ARCS: Auroral Reconstruction CubeSwarm
A 2019 Heliophysics Medium-Class Explorer Phase A Concept Study
Section D: Science

Kristina A Lynch, Dartmouth College
Robert E Erlandson, JHU/APL
Marilia Samara, NASA/GSFC

Brian Anderson, APL
Jacob Bortnik, UCLA
Meghan Burleigh, UMich, now NRL
David Knudsen, Calgary
Kshitija Deshpande, ERAU
Don Hampton, UAF/GI
Lynn Kistler, UNH
Jim LaBelle, Dartmouth
John Lyon, Dartmouth
Elizabeth MacDonald, GSFC
Robert Michell, GSFC
Chris Mouikis, UNH
Steven Myers, SwRI, now FrontGrade Technologies
Rumi Nakamura, IWF
Romina Nikoukar, APL
Werner Magnes, IWF
David Rau, UNH
Griffith Russell, Gryphon Effect
Christine Schulz, SwRI
Roy Torbert, UNH
Jules van Irsel, Dartmouth
Sarah Vines, APL, now SwRI
Matt Zettergren, ERAU
Shasha Zou, UMich

ARCS

Auroral Reconstruction CubeSwarm

2019 Heliophysics Medium-Class Explorer
Phase A Concept Study
07 July 2021

Principal Investigator:
Professor Kristina A. Lynch, Dartmouth College

Authorizing Official:
Jill Mortali, Dir., Office of Sponsored Projects
Dartmouth College

Proposal title page restriction removed for this public document.

AURORAL RECONSTRUCTION CUBESWARM

Connecting the Dots: A distributed high-fidelity map for decoding the auroral ionosphere

The **ARCS** MISSION GOAL: **decode the aurora by exploring the relationship between the visible aurora and distributed currents and flow fields**, to unlock critical physics of the auroral ionosphere at mesoscales.

ARCS addresses Key NASA Goals by exploring auroral processes at mesoscales. These scales have consequences, not only for the ionosphere-thermosphere (IT) system but significantly for the global dynamics of the entire magnetosphere. ARCS directly aligns with NASA Strategic Goals and Objectives and with NASA SMD's strategic objectives to explore processes in the space environment active throughout the solar system and the universe. Specifically, ARCS's focus is to fill key knowledge gaps of "how the IT system responds to, and regulates magnetospheric forcing over... regional and local scales" (AIMI-1).
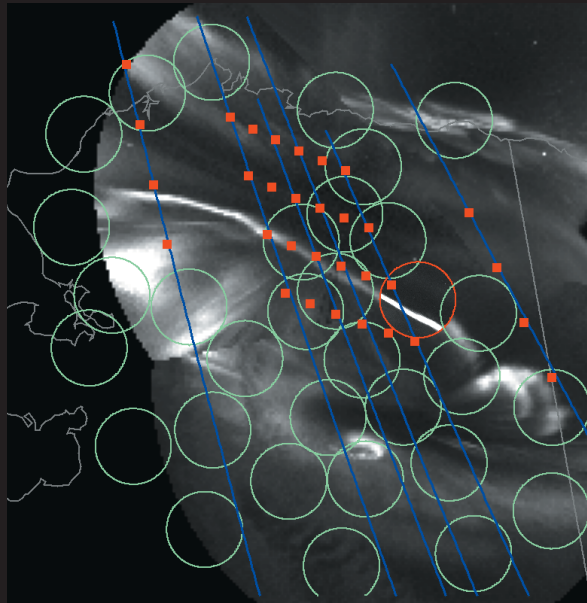
ARCS Science Objectives:

- **SO-1: DISCOVER** Map the 2D mesoscale structure and temporal evolution of plasma flows and currents in the auroral ionosphere.

- **SO-2: LINK** Determine how these 2D maps of plasma flows and currents self-consistently evolve in conjunction with auroral ionospheric density responses

- **SO-3: UNDERSTAND** Determine the roles of the physical mechanisms regulating the relationships between the flows, currents, auroral forms and precipitation in the auroral ionospheric system.

ARCS MISSION OVERVIEW:

- Truly next generation mission using a swarm of 32 cubesats (red dots above) to explore the aurora at mesoscales

- In-situ flows, currents, and 3D electron density measurements over a dedicated array of ground-based auroral imagers (green circles above) & dual frequency transmitters

- Multi-point data reconstructions feed modern 3D physics-based simulations to explore the auroral ionosphere as a system

- Observing System Simulation Experiment (OSSE) with synthetic data generated by GEMINI model shown in reconstruction examples below
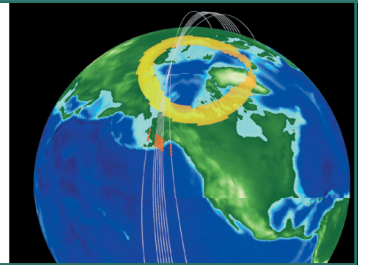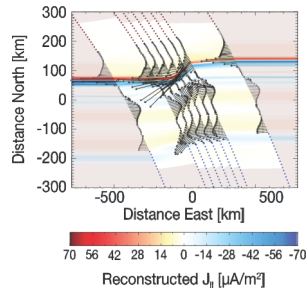
ARCS SYNTHETIC DATA RECONSTRUCTIONS
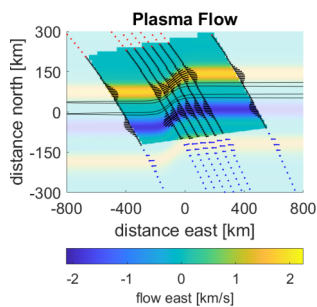
Plasma Flow (STA)
Field Aligned Currents (MAG)
Electron Density (eTOMS)
Precipitation Energy (GBO)
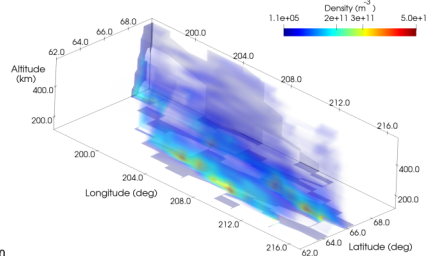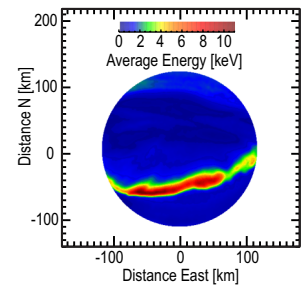
The ARCS swarm produces low-resource observations for system science enabling progress toward the "**Diversified and Distributed Sensor Deployment Strategy**" envisioned in the NAS Decadal Appendix C [NRC, 2013] as a requirement for creating "system-wide understanding" based on data "integrated into distributed yet coordinated approaches that create the best system-wide understanding."

D. Science

Executive summary

The Auroral Reconstruction CubeSwarm (ARCS) MISSION GOAL is to **decode the aurora by exploring the relationship between the visible aurora and distributed currents and flow fields**, to unlock critical physics of the auroral ionosphere at mesoscales. ARCS generates novel, high fidelity, two-dimensional electric and magnetic field maps from an in situ CubeSwarm in concert with dense ionospheric tomography and ground-based multispectral auroral imaging. The final link in the fundamental global magnetic convection cycle is reflected in, and possibly governed by, these fields and associated aurora. Mesoscale flows, currents, and auroral structures represent significant ionospheric energy inputs at auroral latitudes, creating a variety of geophysically important responses and space weather impacts. **These are fundamental processes occurring at magnetized planets and moons with ionospheres.** ARCS is a next-generation mission consisting of the first-ever swarm of NASA scientific satellites packaged in high-heritage CubeSat buses, coupled with a dense grid of custom, ground-based observatories.

ARCS addresses its Science Objectives with a heterogeneous array of observations, illustrated in Figure D-1, with distributed coverage of mesoscale auroral ionospheric systems. ARCS consists of **an array of 32 6U Cube-Sats - a CubeSwarm**. The CubeSwarm has nightly conjunctions with a new, 32 station, dedicated ground-based

observatory system spanning Alaska. **The multipoint in situ and ground-based measurements, together with dense tomography, provide high-fidelity drivers for state-of-the-art physics-based simulations to provide rigorous connections to the underlying physical processes**.

ARCS implements multiple copies of four instruments: STA, MAG, eTOMS, and GBO. Each of the 32 identical Blue Canyon Technologies (BCT) 6U CubeSats carries: (a) two Sweeping Thermal Analyzers (STAs), an electrostatic analyzer to record distribution functions of thermal ionospheric ions and measure the ionospheric flow vector; (b) a fluxgate magnetometer (MAG) on a boom for auroral magnetometry; and (c) an electron density tomography scintillation experiment (eTOMS) at UHF and S-band frequencies, recording phase and amplitude information on beacon signals from the Ground Based Observatory (GBO), our fourth instrument, consisting of 32 stations in Alaska. Each GBO station includes multi-
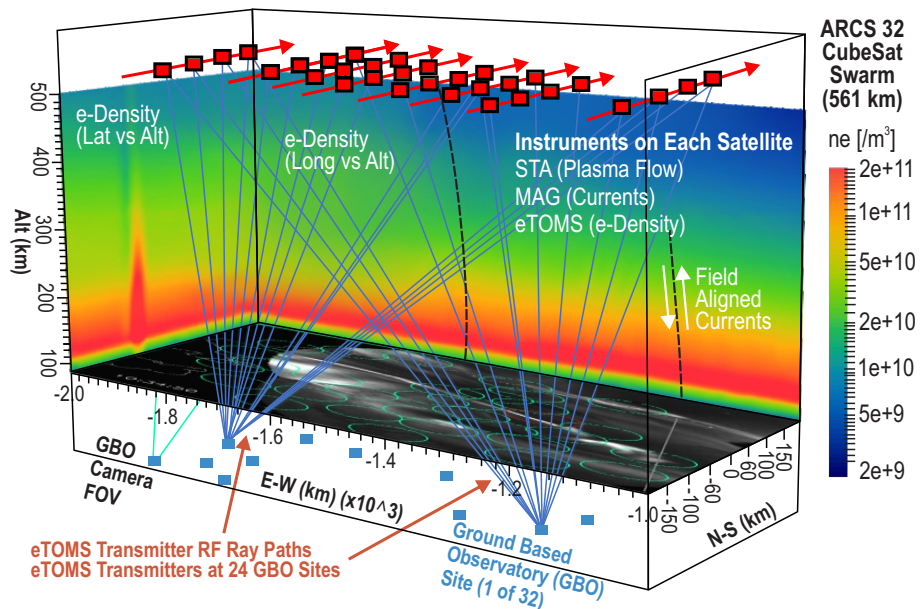

Figure D-1. ARCS heterogeneous arrays in a GEMINI model datacube

spectral auroral imagers to observe the aurora at high resolution and cadence, allowing determination of precipitation total energy flux and average energy. 24 GBO stations also include matching transmitters for the eTOMS receivers, providing a very dense lattice of ray paths for tomography.

The BCT CubeSat bus uses flight-proven power, attitude determination and control, electric propulsion, navigation, and telemetry systems exceeding ARCS requirements. The CubeSwarm deployment, commissioning, orbit and configuration maintenance, and command and telemetry use proven technologies and offer substantial margins.

ARCS uses existing instrumentation in a new, distributed platform, for a transformative system science view.

D.1 Science Background, Goal, and Objectives

D.1.1 Science Goals and Objectives

The ARCS MISSION GOAL is to decode the aurora by exploring the relationship between the visible aurora and distributed currents and flow fields, to unlock critical physics of the auroral ionosphere at mesoscales. These are scales relevant to nightside discrete arcs, defined below. The night-time aurora and its dynamics are tell-tales of the invisible electrodynamics ultimately driven by the transport of magnetic flux from the tail to the inner magnetosphere. This flux transport is the final link in the global magnetic convection cycle [Dungey, 1961] starting with magnetic reconnection at the dayside magnetopause [Burch et al., 2016] and proceeding with convection into the lobes, tail reconnection [Torbert et al., 2018], transport Earthward, and ultimately back to the dayside. This global magnetospheric convection is reflected in the 2D plasma convective flows in the ionosphere.

Dynamics of magnetospheric convection create auroral forms occurring on mesoscales, intermediate between large (>2 hours in local time x 10° in latitude) and small (<50 km in longitude and <0.1° in latitude) sizes; these forms often have sharp boundaries at ~1 km scales. Auroral arcs, auroral streamers, westward traveling surges, and poleward boundary intensifications occur systematically in the nightside auroral zone reflecting fundamental but different

magnetospheric dynamics, and are intimately related to parts of the convection cycle; these visible signatures reflect sudden onsets of flows, currents, and plasma reconfigurations. However, since the electrodynamics are invisible it has not been possible to decode these visible auroral forms and their evolution to determine the corresponding flows and currents and hence understand their contributions to convection and energy dissipation. **A crucial step in understanding how the coupled magnetosphere - ionosphere system controls convection is to observationally constrain, and understand, the flows and currents at the auroral footpoint of the system.** The ARCS mission delivers focussed, closely spaced, distributed, in situ observations of ionospheric flows and magnetic fields, together with advanced multi-spectral distributed auroral imaging and dense local ionospheric tomography using arrays of ground transmitters, to provide the **observational breakthrough** required to finally reveal, by fully constraining the ionospheric end of the coupled system, the actual electrodynamics of each of these auroral forms.

ARCS bypasses standard idealizations of the auroral ionosphere. Prior auroral studies at arc-relevant mesoscales have been constrained by limited observations and are forced to presume variations exist only across magnetic-latitude-aligned structures (1D) and/or use height-integrated ionospheric slabs. Some parameters such as electric potential are indeed strongly mapped along magnetic field lines (2D), and auroral features are often invariant along their length (1D). Nonetheless, parameters defining the auroral ionosphere (currents, flows, and conductivity) vary in three spatial dimensions (3D) and in time (i.e. including inductive effects). The mesoscale forms we want to decode can have (or not have) significant variations along their length, and their behavior can depend closely on the 3D structuring of conductivity, currents, and flows. The current continuity equation (below) quantifying this system depends not only on the parameters themselves, but also on their divergences, gradients, and curls, so the distributed and high-fidelity **maps form the ARCS observational breakthrough** required for progress on quantitative analysis of realistic auroral forms.
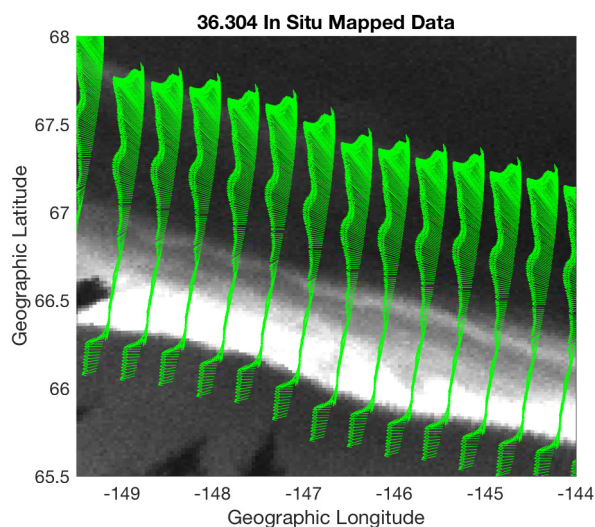
ARCS top-level science objectives are thus:

- **_SO-1:_** Map the 2D mesoscale structure and temporal evolution of plasma flows and currents in the auroral ionosphere;
- **_SO-2:_** Determine how these 2D maps of plasma flows and currents self-consistently evolve in conjunction with auroral ionospheric density responses; and
- **_SO-3:_** Determine the roles of the physical mechanisms regulating the relationships between the flows, currents, auroral forms and precipitation in the auroral ionospheric system.

What are the open puzzles?

SO-1 encapsulates puzzles requiring distributed, high-fidelity in situ observations of auroral drivers. How is the ionospheric electric field distributed, how localized are regions of flow, how are they placed in relation to regions of current, how do regions of current evolve? Figure D-2 shows a flow field replicated from a single sounding rocket crossing, assuming invariance in the arc-tangent direction; ARCS observes directly the 2D field.

SO-2 concerns causal connections between auroral drivers and plasma density responses. When do arc structures reflect ionospheric electric field structures adapting to an imposed current, and when are they current structures adapting to an imposed electric field? How can we recognize which of these two aspects dominate in different situations? What ionospheric density structuring results from current-driven vs voltage-driven sources? How are mesoscale density structures, fields, and currents connected to ionospheric radio scintillation?

SO-3 pulls together the first two objectives and explores puzzles about the relative roles of different physical processes in arc structures. When are Pedersen currents sufficient for current closure and when do Hall currents play a role? Do arcs twist in order to satisfy an increased need for current carriers? Is proper motion related to return current carrier evacuation, and when is this necessary? What details of ionospheric dissipation processes are driven by mesoscale electromagnetic and particle energy inputs? Why do arc structures take on the variety of forms they do, and can we learn to use them as a diagnostic of the M/I state?

Resolving this broad range of open puzzles – including current vs voltage generators for arcs [Newell, 1996; Borovsky, 1998], distributions of electric potential at high latitudes [Lyons, 2016], energy input quantification errors [Huang, 2014; Codrescu et al., 1995, 2000; Deng et al., 2009; Pedatella and Richmond, 2018], locations of strong localized flow shears [Archer et al., 2017, 2019a] -- in the auroral zone depends critically on observing mesoscale features at high fidelity. Progress on understanding requires a new paradigm of measurements.

ARCS addresses, through distributed, high-fidelity in situ measurements and modeling, the hypothesis that mesoscales are important to auroral physics in terms of both self-consistent magnetosphere-ionosphere coupling and the ionospheric dissipation of energy. The integration of the paradigm-shifting class of distributed observations with state-of-the-art physics-based simulations therefore provides a powerful capability to identify key relationships between a wide range of auroral ionospheric scales.

Figure D-2. High fidelity, in situ flow vectors, replicated along the arc, overlay an auroral image (Clayton et al., 2019a) highlighting the clear connection between the arc structure and flow field measurements.

Why haven't we answered these puzzles?

The ARCS science objectives require mapped characterizations of critical system parameters at mesoscale (arc-relevant scales, see below) resolution, in order to get past limiting assumptions about static sheetlike auroral struc-
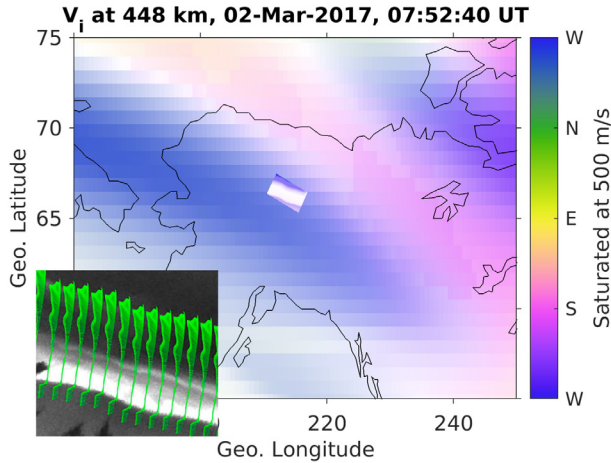
V$_i$ at 448 km, 02-Mar-2017, 07:52:40 UT

Figure D-3. A global GITM run showing iono-spheric flows in the topside F-region driven by the Weimer empirical convection model [Weimer, 1996] (courtesy D. Ozturk, JPL). Color indicates direction of flow, and brightness the flow magnitude. The lower inset repeats Fig D-2; the small rectangle at the center of the GITM run shows this local flow field used as a driver for a local GEMINI run.

tures, and to progress beyond the capabilities of large-scale low-resolution models. Figure D-3 **illustrates the disparity between state-of-the-art global models, and local models capturing arc-scale features**; a major difficulty for progress has been the lack of distributed high-fidelity observations of drivers. This event demonstrates strong, clear, local activities not captured by the high-latitude convection driver used for the global simulation. **A difficulty of addressing our science objectives with existing databases** such as global auroral imager and SuperDARN data is that they only resolve large-scale features [Zou et al., 2009] and are insufficient for revealing mesoscale auroral features. Radar imaging even from local facilities such as PFISR and EISCAT3D provides plasma information averaged over a voxel of dimensions comparable to their resolution, far different from the point-like measurements of an in situ probe; and do not measure electric currents.

What is mesoscale?

The size of **mesoscale nightside auroral structures targeted by ARCS** ranges from ~60 km (e.g., auroral beads) to several hundreds of km (e.g., westward traveling surges) [e.g., Kalmoni et al., 2018; Zou et al., 2010]; to discrete

arcs a few km wide [Knudsen et al., 2001], with gradient scale length boundaries of order of a kilometer [Clayton, 2019a] and longitudinal spans wider than Alaska (1000 km). Recent observations by the ESA Swarm mission [Archer 2017, 2018] show the strong localized flow structures adjacent to nightside arcs, with, as in Clayton et al. [2019a], gradient scale lengths on the order of a km. The mosaic shown in Figure E-23 illustrates the range of structures to be seen over AK at 10UT (2230 MLT). The multicamera image shown on the Fact Sheet illustrates the span of these structures, as well as their finely detailed edges. We wish to capture the arc-relevant features shown, **both** over a regional 2D span encompassing the structures as a whole, **and** with high-resolution pointlike observations with km resolution. In §D.5-7 and §E.3 we show methods for reconstructing in situ vector fields from multipoint in situ data, using information about directions of maximum and minimum variance to help connect the dots across the field.

A strongly coupled 3D system:

The interaction of auroral currents and particles with the terrestrial atmosphere and ionosphere is a **fundamentally three-dimensional process** not captured with sheet-like idealizations, or with existing global models, or with observations containing inherent space-time ambiguities. It is not possible to fully populate this system down to arc-relevant gradient scale lengths with a complete set of measurement points; however, strong constraints on the system electrodynamics make this unnecessary. The height-integrated ionospheric current continuity equation (electrostatic limit) reads [Brekke, 1989; Kelley, 1989]:

$$J_{\parallel}(x,y) = \Sigma_P \left(\nabla \cdot \mathbf{E}_{\perp} \right) + \nabla \Sigma_P \cdot \mathbf{E} - \nabla \Sigma_H \cdot \left(\mathbf{E} \times \hat{\mathbf{b}} \right)$$

where $J_{\parallel}(x,y)$ is field-aligned current as a function of position in the perpendicular-to-**B** plane, and Σ_P and Σ_H refer to Pedersen and Hall height-integrated conductance. The divergence of the ionospheric electric field, and the gradients of conductivities, are sources and sinks of field-aligned currents. Ionospheric conductivities are extremely and rapidly sensitive to variations and structures in electron precipitation, and are further affected by transport processes accompanying visible auroras [e.g. Doe et al, 1995]. The height-integrated equation shown above is
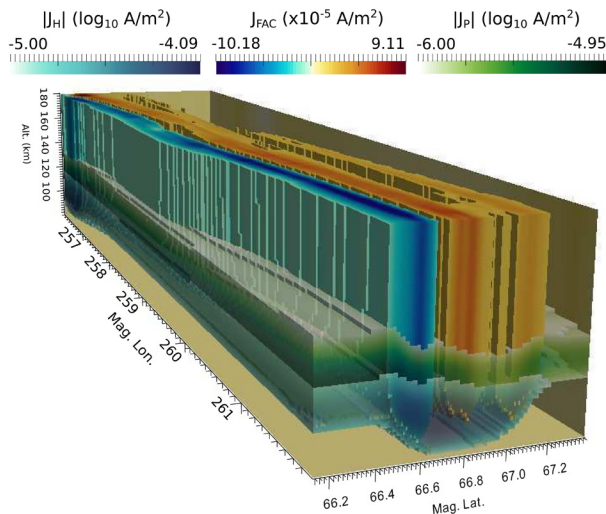
Figure D-4. Three-dimensional view of auroral currents from a data-driven GEMINI simulation run. This 3D volume is the local model run for the insets in Figure D-3.

shorthand for a three-dimensional, time dependent (inductive) system, **yet current continuity is a statement of fact applicable at each point in space**. Maxwell's equations, and associated conservation laws like current continuity, tie together these different system parameters, and their divergences, gradients, and curls. Although discussed here in the electrostatic approximation, analogous fundamental relations (continuity, generalized Ohm's law, Faraday's law) also apply when wave dynamics are relevant [cf. Lotko, 2004].

A physics-based, 3D, time-dependent model encoding these rules, with data drivers of appropriate fidelity and span, can visualize and lead to understanding of this system, just as the simplified, idealized height-integrated equation above has guided many previous auroral studies [Marghitu, 2013]. An illustrative example of such a data-driven model reconstruction is shown in Figure D-4, which plots the Pedersen, Hall, and field-aligned currents of an auroral arc with substantial structure in both latitude and longitude.

Simulated ionospheric processes such as shown in Figures D-2 and D-4 (modeled via the GEMINI ionospheric model), include production of Field Aligned Currents (FAC), small-scale fluid turbulence, density structures, and dynamics of return current regions. Our proposed exploration of auroral ionosphere mesoscales is a **system science** study; successful

implementation and a path to closure require the synthesis of our heterogeneous datasets through physics-based models. This methodology is **directly in line with the Heliophysics Decadal Survey** DRIVE recommendations: "... system science requires new types of configurations of observations..." used in "computational models that extract essential physics from measurements made across multiple observing platforms" [NRC, 2013].

D.1.2 Why ARCS Now?

New observations are needed to - and now can - advance knowledge of the auroral system, and its role in the larger magnetosphere. We can now approach mesoscale resolutions because distributed observations -- low-resource Cube-Sats and modern camera technology -- are now possible, thus allowing a larger field-of-view than is achievable from any single ground-based station or single spacecraft. **ARCS enables discovery-mode auroral science, probing the nature of electric and magnetic fields at unprecedented resolution and dimensionality**.

The morphology of aurora, as an integrated component of the convection cycle, can be used to probe not only the Earth's magnetosphere, but even a distant planet, if we know how to interpret what we see [Delamere, 2015; Grodent 2014; Jia et al., 2012; Sarkango et al., 2019]. Understanding the mesoscale ionospheric physics of the Earth's auroral zone has implications for understanding what we see when we view the aurora -- often the first thing we know about planetary magnetospheres.

D.1.3 Value to NASA Science

ARCS is a heliophysics mission addressing goals related to NASA strategic plan [2018] objective 1.1 to "Understand the Sun, Earth, Solar System, and Universe." ARCS explores physical processes governing auroral ionospheric flows and currents in the space environment close to Earth, linking the ionosphere to the magnetosphere through the central "traffic-circle" of the auroral zone. These processes are fundamental, occurring at magnetized planets and moons with ionospheres, thus leveraging our understanding of the Earth to that of other planetary space environments.

The Heliophysics Decadal Survey identifies two Key Science Goals (KSGs) addressed by

ARCS. "**KSG2**. Determine the dynamics and coupling of Earth's magnetosphere, ionosphere …requiring research approaches that treat it as a coupled system." [NRC, 2013]. ARCS provides exactly the type of resolved, systemic measurements needed as drivers for data-driven simulations necessary to deeply explore the physics of this coupled system, providing a critical contribution to KSG2.

ARCS addresses the fundamental role of the aurora itself, relevant to: "**KSG4**. Discover and characterize fundamental processes that occur both within the heliosphere…. Advances…require the capability to characterize fundamental physical processes that govern how energy and matter are transported. … to improve the capability to predict space weather." [NRC, 2013] ARCS addresses specific questions about the physical mechanisms regulating the relationships between the flows, currents, and precipitation of the auroral ionospheric system. It contributes specifically to KSG4 including advancing predictive descriptions of the auroral ionosphere for space weather purposes.

The ARCS swarm produces low-resource observations for system science enabling progress toward the "**Diversified and Distributed Sensor Deployment Strategy**" envisioned in the NAS Decadal Appendix C [NRC, 2013]. ARCS is the epitome of a "heterogeneous facility", as encouraged by the "Platforms" discussions [(Appendix C, p. 350), NRC, 2013].

D.1.4 Relation to NASA past/present/future missions

NASA missions Polar and IMAGE had global scale imaging to address the larger scales of the auroral ionosphere. Polar determined the energy input from the magnetosphere to the ionosphere [Wygant, 2000; Torr, 1995; Brittnacher, 1997; Germany, 1997]. IMAGE determined the global response of the magnetosphere to variations in the solar wind [Burch, 2000, Frey et al., 2001, Mende et al., 2001]. The high altitude global approach of IMAGE and Polar advanced the study of large-scale geomagnetic disturbances in a manner not limited by local time and latitude.

The FAST mission was focused at very fine spatial and temporal scales [Carlson, 2001], enabling the quantification of the microphysics of upward and downward current regions and associated parallel potential drops [Carlson 1998a, b], occasionally in the context of ground-based imagery [Stenbaek-Nielsen, 1998; Peticolas, 2001]. Recently, the three ESA-Swarm satellites have enabled unprecedented accuracy in determining FAC signatures and their variability in situ: overlap of the Swarm spacecraft with the THEMIS GBO [Mende et al., 2009] has brought to light the extremely localized strong flows near discrete arcs [Archer, 2017, 2019a], and exploited numerous conjunctions with camera arrays [Archer et al., 2015, 2017, Gillies et al., 2015], but also revealed the limitations of having only 2 or 3 platforms, such as the need for sheet-like and time-stationary assumptions in data interpretation.

Polar and IMAGE revolutionized our understanding of the global aurora, but with limited resolution. FAST and Swarm clarified many plasma physical processes, but their studies lacked auroral system context. The ARCS mission targets the creation of the first 2D maps of mesoscale current and flow structures, in ground-based and tomographic context, in order to address the fundamental gaps in our understanding of the physics of auroral processes, by combining high resolution observations with detailed distributed contextual information for a deep system-level study.

The upcoming Geospace Dynamics Constellation (GDC) mission focuses on the global scales of ionosphere/thermosphere dynamics, while ARCS resolves the electrodynamics of mesoscales in the nightside auroral ionosphere. The understanding gained from ARCS therefore complements GDC's focus on the thermospheric response on larger scales.

D.2 Science Requirements

Array and instrument requirements are detailed in the Science Traceability Matrix (STM), Table D-1.

D.2.1 Investigation: measurements, requirements, and projected performance

CubeSwarm and Ground Based Array:

The design of the ARCS CubeSwarm and groundbased array (Fig. D-1) are driven by the in situ **E** and **B** measurements at F-region altitudes and by the features of the aurora in the pre-midnight sector. Figure D-5 shows the magnetic east-west alignment of typical nightside auroral arcs and the scale of auroral structuring (Fig. E-23). The latitudinal width of the

Table D-1: Science Traceability Matrix

Mission Goal: Decode the aurora by exploring the relationship between the visible aurora and distributed currents and flow fields, to unlock critical physics of the auroral ionospheric system

SO-1: Map the 2D mesoscale structure and temporal evolution of plasma flows and currents in the auroral ionosphere

Physical Parameters	Observables	Instrument	Required Performance	Projected Performance
MO-1: Time dependent plasma flow velocity maps across a 2D region associated with mesoscale structures in the premidnight sector high-latitude ionosphere	Thermal ion distribution function to derive plasma flow vector velocity at instrument frame energies from 1-20 eV and at a rate of up to 30/s in two velocity-space planes as a function of time and at multiple locations across the ARCS CubeSwarm	STA (Instrument)	Two dimensional ion distribution function in two planes, offset by 90 deg to cover (a) along-track and across-track flows (plane approximately perp-**B**), and (b) along-track and vertical (approximately field-aligned) flows. Plasma Flow Range: +-2000 m/s with resolution of 300 m/s, 3-components. Sample Rate: 3-30 Hz (Each Plane)	Two dimensional ion distribution function in two planes, offset by 90 deg to cover (a) along-track and across-track flows (plane approximately perp-**B**), and (b) along-track and vertical (approximately field-aligned) flows. Plasma Flow Range: +-3000 m/s with resolution of 100-300 m/s, 3-components. Sample Rate: 3-30 Hz (Each Plane)
		STA (Swarm)	Coverage of 900 km in MLT at 50 km spacing in inner zone and 300 km spacing in MLT to the east and west of the inner zone (8 orbital planes of satellites); 300 km span in magnetic latitude. Three satellites per orbital plane to resolve space and time	Coverage of 900 km in MLT at 50 km spacing in inner zone and 300 km spacing in MLT to the east and west of the inner zone (8 orbital planes of satellites); 300 km span in magnetic latitude. Four satellites per orbital plane to resolve space and time
MO-2: Time dependent field aligned current maps across a 2D area associated with mesoscale structures in the pre-midnight sector high-latitude ionosphere, and mean electrojet intensity and centroid latitude	Vector magnetic field measurements at a rate of >20/s, accuracy of <20 nT, and resolution <2 nT as a function of time and at multiple points across the ARCS CubeSwarm	MAG (Instrument)	Range: +/- 50000 nT; Resolution: 2 nT; Noise < 0.1 nT/sqrt(Hz) @ 1 Hz; Sample Rate = 20/s (Each component); Field-aligned current intensity resolution < 1 uA/m2; Inter-spacecraft Accuracy = 20 nT	Range: +/- 65000 nT; Resolution: 0.5 nT; Noise < 0.03 nT/sqrt(Hz) @ 1 Hz; Sample Rate = 128/s (Each component); Field-aligned current intensity resolution < 0.2 uA/m2; Inter-spacecraft Accuracy = 10 nT
		MAG (Swarm)	Coverage of 900 km in MLT at 50 km spacing in inner zone and 300 km spacing in MLT to the east and west of the inner zone (8 orbital planes of satellites); 300 km span in magnetic latitude. Three satellites per orbital plane to resolve space and time	Coverage of 900 km in MLT at 50 km spacing in inner zone and 300 km spacing in MLT to the east and west of the inner zone (8 orbital planes of satellites); 300 km span in magnetic latitude. Four satellites per orbital plane to resolve space and time

SO-2: Determine how these 2D maps of plasma flows and currents self-consistently evolve in conjunction with auroral ionospheric density responses

Physical Parameters	Observables	Instrument	Required Performance	Projected Performance
MO-1 (Same as Above)	Same as Above	STA	Same as Above	Same as Above
MO-2 (Same as Above)	Same as Above	MAG	Same as Above	Same as Above
MO-3: Electron density as a function of latitude, longitude and altitude with mesoscale resolution to be used to determine the ionospheric conductivity in the nightside auroral region	Electron density determined by dense tomographic reconstruction, using UHF and S-Band signals between transmitters located at ARCS GBO sites and the ARCS CubeSwarm to produce electron densities in a 3D volume from 90 to 540 km altitude	eTOMS (Instrument)	Frequencies: UHF (400-450MHz) and S-Band (2025-2120 MHz); Channels: 12 per satellite (6 simultaneous stations at 2 frequencies per station); Sample Rate of Amplitude and Phase: 50 Hz; Sensitivity: <=0.02 TECU (Relative TEC); Antenna field of view with link margin > 6dB: 50° from nadir	Frequencies: UHF (400-450MHz) and S-Band (2025-2120 MHz); Channels: 18 per satellite (9 simultaneous stations at 2 frequencies per station); Sample Rate of Amplitude and Phase: 50 Hz; Sensitivity: <=0.02 TECU (Relative TEC); Antenna field of view with link margin > 6dB: 50° from nadir
		eTOMS (Swarm)	>24 eTOMS beacon receivers over ground transmitters. Tomographic Inversion Coverage and Spatial Resolution: Altitude = 90 - 561km (10-40km resolution); Latitude = 61 to 72°N (1°); Longitude = 140° to 166°W (2°)	32 eTOMS beacon receivers over ground transmitters. Tomographic Inversion Coverage and Spatial Resolution: Altitude = 90 - 561km (10-40km resolution); Latitude = 61 to 72°N (0.2°); Longitude = 140° to 166°W (1.5°)
MO-4: Scintillation maps as function of time in the nightside auroral zone	Scintillations of ARCS dual band transmitter signals along the line of sight between the ARCS GBO transmitters at 9 different locations at a given time, and the ARCS CubeSwarm	eTOMS (Transmitter)	Frequencies: UHF (400-450MHz) and S-Band (2025-2120 MHz). Ground Sites: 18 Dual Frequency Transmitters	Frequencies: UHF (400-450MHz) and S-Band (2025-2120 MHz). Ground Sites: 18 Dual Frequency Transmitters

SO-3: Determine the roles of the physical mechanisms regulating the relationships between the flows, currents, precipitation and auroral forms in the auroral ionospheric system

Physical Parameters	Observables	Instrument	Required Performance	Projected Performance
MO-1 (Same as Above)	Same as Above	STA	Same as Above	Same as Above
MO-2 (Same as Above)	Same as Above	MAG	Same as Above	Same as Above
MO-3, 4 (Same as Above)	Same as Above	eTOMS	Same as Above	Same as Above
MO-5: Time dependent auroral imagery as a function of time over a 2D region of the nightside auroral region	Auroral luminosity at four wavelengths (557.7, 427.8, 844.6 and 630.0 nm) covering a 2D region of the nightside auroral ionosphere	GBO (Instrument)	Wavelengths: 557.7, 427.8 and 844.6 nm (for <E> above 1 keV); 557.7 and 630.0 nm (for <E> below 1 keV); 557.7, 427.8, and 844.6 nm Sensitivity = 250 Rayleigh; 630.0 nm Sensitivity = 50 Rayleigh; Spatial Resolution (427.8, 557.7 and 844.6 nm) at 110 km: 0.5 x 0.5 km; Spatial Resolution (630 nm) at 110 km: 2 x 2 km; Frame Rate (427.8, 557.7 and 844.6 nm): 8 Hz during overpass; 0.2 Hz before/after; Frame Rate (630 nm): 0.5 Hz during overpass; 0.2 Hz before/after	Wavelengths: 427.8, 557.7 844.6 and 630.0 nm; 557.7, 427.8, and 844.6 nm Sensitivity = 100 Rayleigh; 630.0 nm Sensitivity = 20 Rayleigh; Spatial Resolution (427.8, 557.7 and 844.6 nm) at 110 km: 0.46 x 0.46 km (80° FOV); Spatial Resolution (630 nm) at 110 km: 2 x 2 km; Frame Rate (427.8, 557.7 and 844.6 nm): 15 Hz during overpass; 0.2 Hz before/after; Frame Rate (630 nm): 0.5 Hz during overpass; 0.2 Hz before/after
MO-6: Time dependent electron average energy and energy deposition across a 2D area in the nightside auroral region	Auroral luminosity at four wavelengths (427.8, 557.7, 844.6 and 630.0 nm), using specific ratios to derive maps of the average energy, from 0.1 to 20 keV, and total energy flux, from 5 to 500 mW/m2, of auroral electrons producing the auroral display	GBO (GBO Array)	Provide 75% coverage from 62° to 72° magnetic latitude across Alaskan longitudes. Complete coverage not possible due to remote locations. Number of GBO Stations to Cover Area of Interest: 24	GBO provides >75% coverage from 62° to 72° magnetic latitude across Alaskan longitudes with 32 sites. Complete coverage not possible due to remote locations. Number of GBO Stations to Cover Area of Interest: 32

Mission Requirements

M1 Orbital Configuration
M1-1: Configure a CubeSwarm of in situ platforms in LEO spanning at least 900 km in longitude with an dense inner grid with longitude spacings of ~50 km and outer grid with longitude spacings of ~300 km sampling the same latitudes not less than three times per orbit. (Driven by all Science Objectives)
M1-2: Configure the CubeSwarm such that the four satellites in each orbital plane have spacings of >1.1° and <1.2° Mean Anomaly (MA) separation; and such that each row of 8 spacecraft is aligned to a common magnetic latitude. (Driven by all Science Objectives)

M2 Ground Track
Maneuver the CubeSwarm to achieve repeated ground tracks with CubeSwarm satellite position (SP) 14 over the GBO Bettles station +/-1° in the pre-magnetic midnight sector once per day: polar & sun-synchronous (Driven by Science Objectives 2 and 3).

M3 Spacecraft Accomodation
Accommodate the science intruments (STA, MAG, and eTOMS) and ensure <20 arc second attitude knowledge and <1 degree pointing control. (Driven by all Science Objectives)

M4 Ground Infrastructure Observations
M4-1: Provide multi-station GBO with 75% coverage from 62° to 72° magnetic latitude across Alaskan longitudes for high rate multi-spectral auroral imaging. (Driven by Science Objectives)
M4-2: Host eTOMS dual frequency transmitters in 24 GBO stations. (Driven by Science Objectives 2 and 3)

M5 Science Data Acquisition Plan
M5-1: Acquire 3 daily science crossings (in situ alone) of the nightside pre-magnetic midnight auroral region (Driven by all Science Objectives)
M5-2: Acquire daily science crossings (in situ & tomography) of the nightside pre-magnetic midnight auroral region over the Alaskan GBO (Driven by Science Objectives 2 and 3)

M6 Science Data Volume
Capability to return >9.6 GB of science data per day from the 32-CubeSat CubeSwarm (3 science crossings per day) (Driven by all Science Objectives)

M7 Spacecraft Orientation
Orient the STA in the Ram direction and the eTOMS patch receiving antenna pointed nadir during the science crossings (Driven by all Science Objectives)

M8 Timing
GPS timetagging of data streams to better than 1ms (Driven by all Science Objectives)

M9 Launch Readiness
Be ready for launch no later than October 2026 and collect science data for ≥ 24 months.
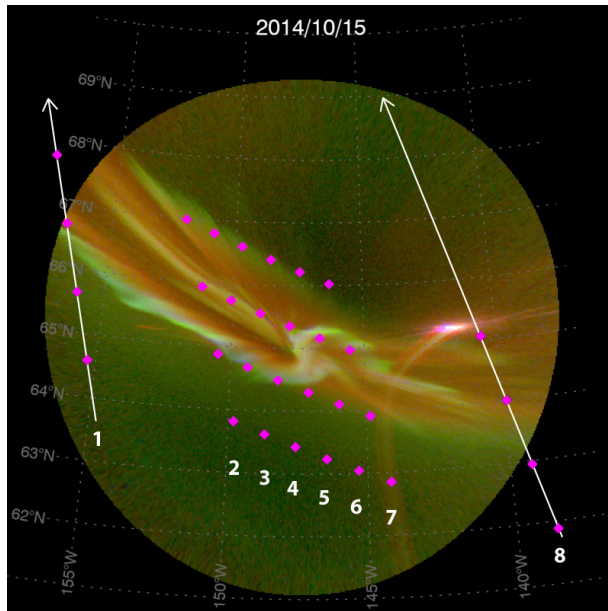
Figure D-5. Auroral image acquired using a single all-sky imager showing an example auroral structure at 10UT over Alaska, covering 6° in latitude and 15° in longitude; the pink dots represent the CubeSwarm moving north, in 8 tracks of 4 spacecraft, through the field of view.

nightside auroral arcs is typically on the order of ~10km [Knudsen et al., 2001] with gradient scale lengths at the edges of 1 km or smaller [Lynch et al., 2017, Clayton et al., 2019a, b]. **The along-track extent of the CubeSwarm** is governed by the need to separate space and time, and the along-track cadence of the in situ data is set to explore the gradient scale lengths across arcs. (See the field reconstruction data products in Fig. D-6). Multiple satellites are required aligned in the along-track direction; the investigation becomes more robust as satellites in a given plane are increased to 3 or 4 per plane. The **cross-track extent and spacing of the CubeSwarm** satisfies two requirements. First, CubeSats spanning 15° in magnetic longitude (900 km at auroral latitudes) provide significant coverage of the basic form and structure of the auroral system in the premidnight sector; the choice of 10UT in Alaska (~2230MLT) provides both a good sampling of diverse premidnight auroral forms and provides the longest span of days per year with dark skies for camera operation. Second, the spatial separation between adjacent CubeSat planes must both cover the 900 km longitudinal extent, and

provide sampling of the aurora along the arc length, allowing measurements of both simple east-west arcs and more complicated auroral forms.

We have chosen a **swarm design to consist of 8 planes of CubeSats** with a nested grid of cross-track spacing, as illustrated in Figure D-5. The local time coverage is obtained by four trajectory planes separated by 5° of longitude (about 300 km at auroral latitudes); tracks 1, 2, 7, and 8 in Figure D-5. An additional set of four trajectory planes separated by 1° of longitude (roughly 60 km at auroral latitudes) is placed at the center of the larger grid (tracks 3, 4, 5, and 6.) Finally, the neighboring CubeSat positions are phased to be aligned along lines of constant magnetic latitude in the northern nightside auroral zone. The baseline mission requires four CubeSats in each plane, with subsequent CubeSat passages of the same point spaced by 18 sec (137 km); thus the array is 410 km wide in latitude and takes 54 sec to pass over a given location.

The electron density tomography lattice extends between transmitters at the GBO sites (**not** GPS signals!), and receivers on the ARCS CubeSats (Fig. D-1). Tomographic reconstruction from this **dense lattice of ray paths** produces unprecedented high-resolution, wide-span volumetric electron densities (§D.5 and §E.3). This measurement provides a distributed, yet mesoscale, view of plasma density throughout the volume; it does not place additional constraints on the definition of the CubeSwarm array.

The dedicated ARCS **GBO** provides continuous spatial and temporal context, providing detailed, invertible, mapped information about auroral precipitating particles' energies and energy fluxes. Ground-based imaging can be limited by cloud cover and daylight (§E.3). For ARCS, this limitation is overridden by the benefits of high-resolution ground-based sensors: significant temporal and spatial context before, during, and after each spacecraft crossing; enormous data bandwidth; no jitter or smear from a moving platform; and avoiding the high cost of space qualified sensors. The ARCS GBO uses sets of four filtered imagers located at 32 sites across Alaska (Fact Sheet, and §E.3), providing auroral imaging with a spatial resolution of 1 km or better over a longitudinal extent cover-

ing the 900 km width of the CubeSwarm, and spanning auroral latitudes from 62° to 72° magnetic latitude for a variety of activity (Kp 1 to Kp 9). To match the 1 km spatial resolution to the rate at which each CubeSat transits an arc (~ 7.6 km/s) the cameras operate at 8 Hz or greater during overpasses; to obtain temporal context, the cameras obtain low-cadence data throughout the night.

The GBO design balances reduction of the off-zenith angle for reconstruction, with the paucity of ground sites with adequate infrastructure in rural northern Alaska. An important result of Grubbs et al. [2018a, 2018b] was to show good reconstructions of the in situ electron precipitation at angles as high as 25° off-zenith. This allows each GBO to provide 2D maps of the electron precipitation parameters with moderate FOVs; multiple sites enable the coordinated regional coverage.

A significant and deciding advantage of ground-based imagery for auroral studies is temporal context. The reconstruction of auroral input from the GBO provides the time history of the intensity and depth of auroral ionization, enabling the modeling of density and composition changes. GBO data are collected at low cadence throughout the night, and at high cadence for 15 minutes (long compared to typical ionospheric recombination times [Gledhill, 1986]) prior to, and at least 5 minutes after, an ARCS crossing.

The **heterogeneous multipoint platform defined by the CubeSwarm and the ground array** thus consists of 32 6U CubeSats arrayed in a nested grid configuration designed to measure multi-scale auroral structures, with a matching-sized GBO array. The aggregation of the multipoint data, in situ, tomographic, and ground-based, into different combinations of data maps -- data **reconstructions**, our new data product -- is described in §D.5-7 and §E.3; examples are shown in Figures D-6 and D-7.

A note about choices: It is important to discuss the parameters we are **not** measuring, and address why we have focused on a **large** number of **limited** in situ measurements. We are not measuring in situ electron precipitation directly; we are not explicitly distinguishing mass species; we are not making dedicated measurements of the neutral thermosphere!

One might well ask, why not have 3 or 4, more fully-instrumented payloads, and move them around to explore different scale sizes over the course of the mission? This would also illuminate auroral science questions. But the objectives we have chosen here for new study focus on the auroral ionosphere as a system, and explore the **2D structure of fields as distributed coherent objects**; ARCS is a **swarm**, as opposed to a cluster (as in the MMS mission) or a constellation (as in the AMPERE experiment [Anderson et al., 2014]). In our closure discussions below we show how we plan to interpret the 2D fields of in situ data; in our justification discussions above, we have shown why information about these distributed, yet mesoscale, field structures is a critical science advancement.

Having a **truly multipoint** (4x8, not 1x3 or 2x2!) array of in situ measurements is a **transformational platform**, giving a new view, not previously available, of the ionospheric physics related to detailed auroral imagery. We build on the laws of electricity and magnetism to stitch together our targeted, multipoint observations, instead of having a few fully-instrumented single points, in order to explore the auroral ionosphere in a new dimension. **Every multipoint mission ever designed starts with large numbers of spacecraft and gets whittled down to only a few. We are pushing back on this argument, and exploring a new regime**.

Individual Instruments: We need to measure localized F-region plasma **flow structures** both along and across **B**. As shown in the continuity equation above, we need to know both the flows, and their spatial variations: divergences of **E** and shears in flow, requiring a distributed field of observations. Thermal ion drift velocity vectors (and thus - **v x B** electric field in the ionospheric F-region) are measured (§E.3) in two planes: near-perpendicular to **B**, in the along and across track direction, as well as in the along-track and vertical/parallel to **B** plane, by the two **STA** instruments on each CubeSat, as with the ESA-Swarm TII sensors [Lomidze et al., 2019; Knudsen, 2017]. We need a variety of resolutions for different interpretations, and the driving requirement for the instrument is the sampling cadence of 3-30 Hz allowing us to reach km spatial scale resolutions in spatial interpretations. The higher cadence, in higher flux

regions, allows us to reach up to 15 Hz Alfvén wave signatures in temporal interpretations, also of great interest here; while observations in this Alfvénic range are an assemblage of single-spacecraft observations, the array of 32 points allows exploration of the spatial coherency of Alvenic signatures at spacecraft separation resolutions. It is important to note the modest flow error requirements; errors of up to several 100 m/s are acceptable, as they allow us to explore localized shear structure as seen by, for instance, Archer et al. [2017], and Clayton et al. [2019a]. The STA data provide two 2D velocity space slices of the distribution; non-Maxwellian signatures [St-Maurice and Schunk, 1979] when they appear, will be evident. Maxwellian parameter matching optimization (§E.3) also provides an estimate of S/C potential, which can serve as an excellent thermal electron temperature proxy [Siddiqui, 2011].

We need to measure **vector magnetic signatures** of field aligned current structures, as a basic core observational input for the auroral electromagnetic fields. The **MAG**, a three axis fluxgate magnetometer, measures (§E.3) the space and time evolution of the field aligned current distributions [e.g. Anderson et al., 2014]. Field reconstruction can be done at various levels of resolution, as discussed in §E.3, trading between time resolution and spatial resolution and taking advantage of geometry signatures in the field to connect the multipoint measurements as illustrated in Figure D-6. Single spacecraft measurements (128 vectors/s, at 32 separate places) can diagnose signatures of Alfvénic structures up to 64 Hz. Our basic sensitivity requirement of 1 $\mu A/m^2$ is well below the context of typical 10 $\mu A/m^2$ currents in the active aurora of interest. Additionally, the ARCS altitude, 561 km, is low enough for high quality magnetic field measurements (10 nT uncertainty with 0.5 nT resolution) to remotely **detect the electrojet (Hall) current** of the auroral arc system [Zanetti et al., 1983; Aakjaer et al., 2016]. A moderate electrojet with ground signature of 300 nT yields a signal of ~75 nT at ARCS altitude, providing a valuable validation metric for model closure, as described below.

We need to measure the 3D **volumetric plasma density** and its structuring between the CubeSwarm and the GBO. The drivers for our physics-based models (described below) require both altitude and horizontal structuring density information; even 50% error bars on the density are useful locally specified inputs as long as the spatial resolution distinguishes the E from the F region in altitude, and has roughly 1° horizontal resolution. Tomographic reconstructions are obtained from Total Electron Content (TEC) measurements (§E.3.3) along the ray paths of the **eTOMS** lattice (Fig. D-1), **about 15,000 lines of sight** between the moving swarm and up to 9 ground stations every 30 to 60 s. Electron density is reconstructed over a 5° latitude and 10° longitude span with roughly 1° or better horizontal resolution. The vertical reconstruction grid has 10-20 km vertical resolution in the E-region up to 200 km and 40 km above. An additional benefit from the eTOMS instrument is the ability to **monitor scintillations**. The eTOMS data can map out scintillation events at ionospheric pierce points along the ray path lattice as in Datta-Barua et al. [2015] and Mrak et al. [2017]. We use scintillation observations as a diagnostic for auroral activity [Smith et al., 2008], and for monitoring ionospheric irregularities of Fresnel scales and above [Briggs et al., 1975], especially during intense ionospheric fluctuations or during a loss of lock on one of the two signals.

We need to measure **mesoscale precipitation signatures**, down to 1 km resolution, within the CubeSwarm in situ observations. These signatures define the conductivity variations needed for current continuity equation studies. The ARCS **GBO** (§E.3.4) provides 2D maps of estimates of the auroral average energy, ⟨E⟩, and total energy flux, Q. Signatures of auroral precipitation as low as 1mW/m² for Q, over a range of 0.1to 20 keV for ⟨E⟩, are required to provide high-fidelity model drivers. Instrument requirements are detailed in the STM (Table D-1). Our inversion methods (§E.3) require three auroral emissions: the 557.7 nm and 844.6 nm of atomic O, and the 427.8 nm of N2+. Q is determined by the intensity of the 427.8 nm emission, which, for 1 mW/m², requires 250 R sensitivity. For ⟨E⟩ above 1 keV all other intensities are expected to be well above 250 R even at 1 mW/m (below our minimum requirement). For cases of ⟨E⟩ < 1 keV and low flux (few mW/m²), both the 427.8 nm and 844.6 intensities drop below 250 R. These events are typically diffuse and static structures and can be determined by the

addition of a low-cadence, low-resolution measurement of the atomic O 630.0 nm emission. The 630.0 nm is poorly suited for determining higher values of ‹E› and Q (§E.3), thus requiring the dual inversion methods and the fourth camera to span all of the ARCS cases.

Mapped ‹E›and Q at 1 km resolution require 0.5 km camera pixel scale to maintain Nyquist sampling. An 80° FOV spans the typical span between rural Alaskan towns (250 km at 110 km altitude), and defines the FOV for 0.5 km pixel scale. Given some regions with a complete lack of established towns, the 80° FOV leaves large gaps, and the full FOV requirement of 120° is set to cover > 90% of the ARCS CubeSwarm in situ sampling region. These requirements define the need for 32 GBO sites, each containing 3 cameras, with a subset containing 630.0 nm cameras and eTOMS transmitters.

D.2.2 Data: quality, quantity, relation between data products and objectives, expected results

Observational scenarios: ARCS observations **map** --- that is, produce reconstructions giving 2D, time-dependent measurements of, --- F-region flows, magnetic field perturbations from which 2-D maps of radial current and mean electrojet properties are derived, and auroral precipitation effects; they also yield volumetric (3D) plasma density measurements, all at 1-100 km scales over a wide swath crossing Alaska with sub-minute time resolution between

successive CubeSat passes of a fixed point. Example reconstruction maps are illustrated in Figure D-6, and example precipitation effect maps in Figure D-7.

Orbital dynamics, telemetry budgets, and cloud cover combine to define **three different observational scenarios** of data collection, as detailed in §E.

Scenario 1) in situ CubeSwarm data: two nighttime auroral zone passes (over any location) per day in addition to the pass over the dedicated GBO. Each Scenario 1 (Scen1) data set consists of mapped magnetic perturbations and F-region flows measured at 32 separate
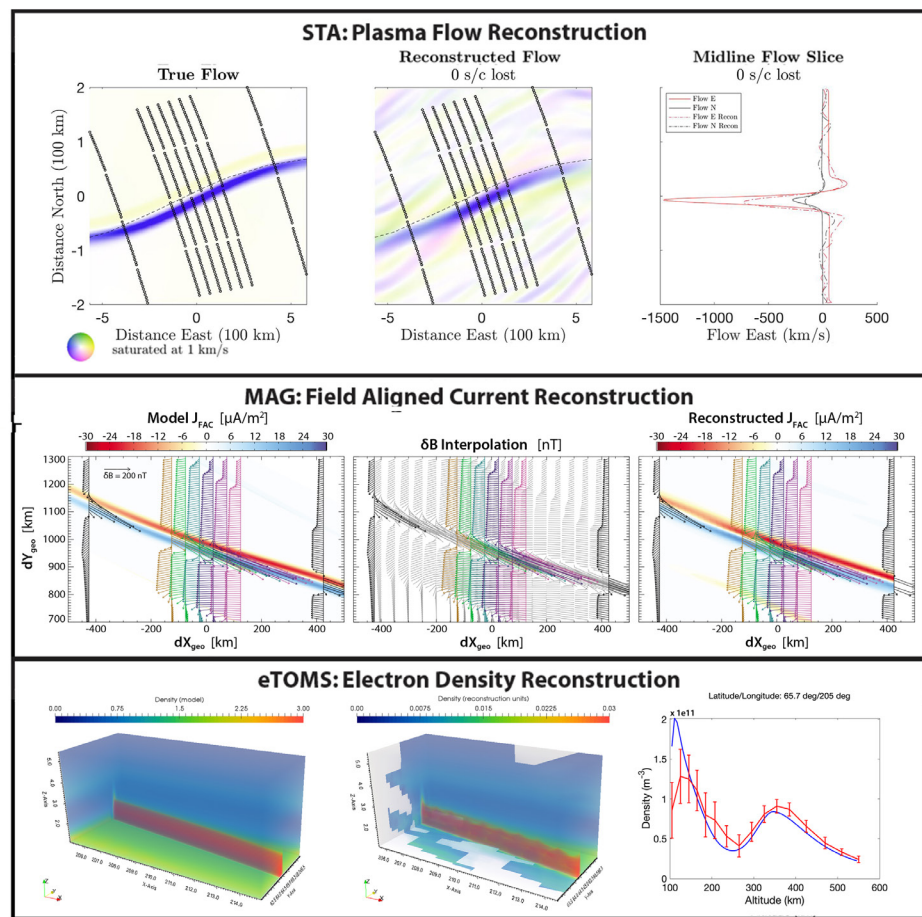

Figure D-6. Example data maps generated from an Observing System Simulation Experiment (OSSE). Virtual data along the CubeSwarm trajectories are extracted from a datacube generated by the GEMINI model, and the reconstruction techniques described in §D.5-7 and §E.3 are used to aggregate the multipoint data into reconstructions of (top) plasma flow [Evans, 2019], (middle) FAC, and (bottom) electron density. In the lower right, the blue curve represents the model density and the red, the reconstruction; the eTOMS reconstruction study input uses both GEMINI and the International Reference Ionosphere (IRI, 2021).
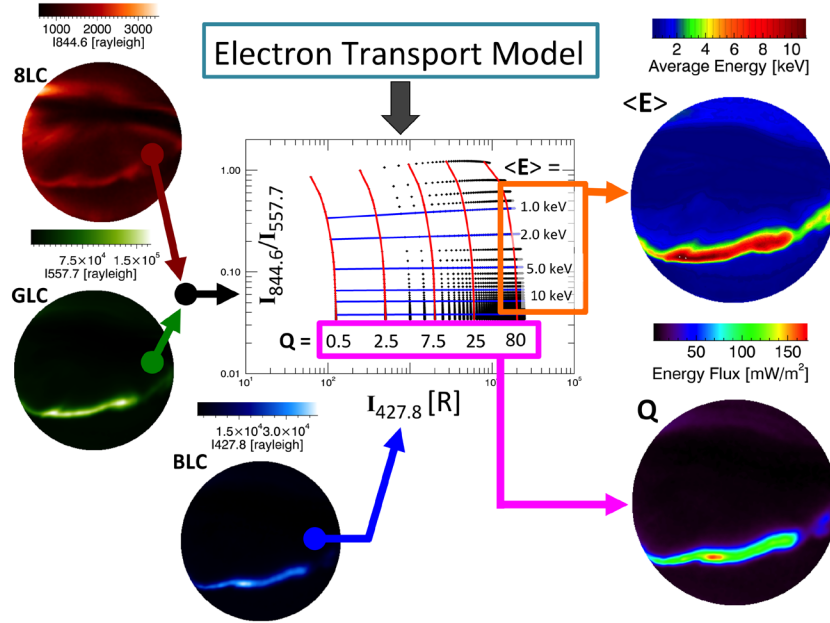
Figure D-7. Example maps of average precipitation energy and flux derived from a single GBO site.

points at high cadence during passage through the nightside auroral zone (45 to 90° latitude.)

Scenario 2) in situ plus tomography data: the auroral zone pass each night over the dedicated Alaskan GBO at 10UT, lacking good imagery. Each Scenario 2 (Scen2) data set consists of tomography and scintillation location maps *in addition to* the magnetic perturbation and flow maps.

Scenario 3) in situ plus tomography plus good optical data: the subset of the Scen2 passes with scientifically significant auroral imagery. Each Scenario 3 (Scen3) data set consists of optical data (yielding maps of average energy and energy flux of auroral precipitation) *in addition to* tomography and scintillation location maps and the FAC and flow maps.

As detailed in §E, the two year science mission phase includes 2,190 in situ passes (Scen1, 2, and 3); 730 of these auroral zone passes include tomography (Scen2 and 3); a (conservatively) estimated 50-100 of these passes also include significant auroral imagery (Scen3). **Each pass includes full cadence data from 32 individual satellites for 12 minutes (1/8 orbit).** Tomography data are available during the overpass of the GBO roughly 5 min per pass. Imagery comes from 32 dedicated sites, collected at high rates for 15 minutes before, and 5 min after, each pass, and at low cadence throughout the

night. The mosaic in Figure E-23 illustrates the range of activity the ARCS mission can explore.

There are a variety of complementary data sources to leverage whenever possible. These include the Poker Flat ISR (PFISR) [Semeter et al., 2009] in central Alaska (i.e., for validation of eTOMS) as well as ionosondes in a variety of locations; the Scanning Doppler Imaging (SDI) [Conde et al., 2018] for background neutral wind information; EISCAT and EISCAT3D [EISCAT3D, 2019]; radars for validation observations in Scandinavian Scen1 crossings; and the THEMIS GBO [Mende et al., 2009; Donovan et al., 2006] and TREx [TREx, 2019]; Canadian imagery facility both for Canadian Scen1 crossings, and for general context in our Scen2/3 crossings.

Modelling framework: Merging of the heterogeneous datasets from ARCS requires sophisticated modeling and machine learning capabilities, driven by the products of data fitting (§E.3) and map reconstruction (§D.5-7 and §E.3) shown in Figures D-6 and D-7. The proposed modeling framework provides a holistic view of the ionospheric volume sampled by ARCS, relating all of the measurements through a physics-based model, and allowing causal relations between parameters to be **quantitatively** explored.

Models used for ARCS analysis comprise recently developed data-driven modeling capabilities built on the global ionosphere-thermosphere model GITM (driven by AMIE) [Ridley et al., 2006; Zhu et al., 2016; Richmond and Kamide, 1988; Richmond, 1992] and local-scale ionospheric model GEMINI [Zettergren and Semeter, 2012, Zettergren and Snively 2015, Zettergren et al., 2015b, Zettergren and Snively, 2019], along with global MHD capabilities from the LFM model [Lyon et al., 2004]. These models are introduced in §E and described in App. L.14; collectively their use in interpreting the ARCS mission data is referred to using
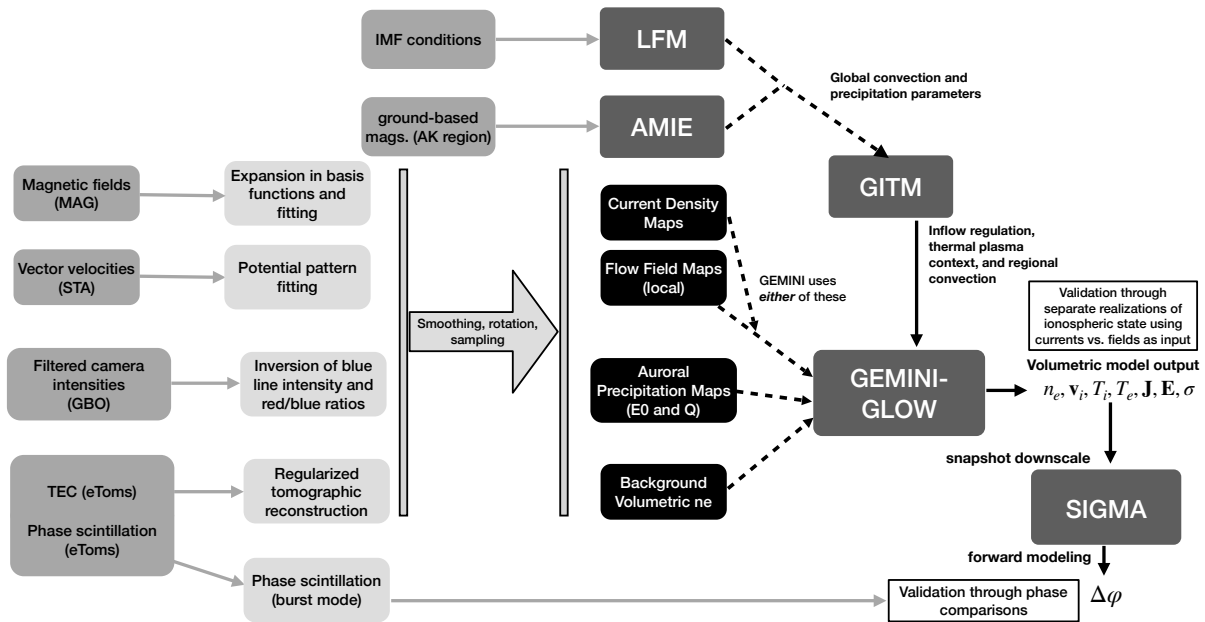
Figure D-8. FrAMBOISE: ARCs modeling framework for synthesizing data from the satellite swarm and GBO. The depiction shown here is applicable to data collected according to Scen3. For Scen2 precipitation information is derived from in situ data (currents, fields, and Poynting flux) instead of from optical data. Scen1 data lack eTOMS beacon data, so background electron density is derived from AMIE/LFM-GITM in these cases.

the acronym **FrAMBOISE - the Framework for ARCS Modeling Based on Observations of Ionospheric mesoScale Electrodynamics** (Fig D-8). FrAMBOISE components have already been developed, and necessary refinements are planned during phases A-D of ARCS, e.g. development of software interfaces (GITM-GEMINI) and addition of induction and generalized Ohm's law, with a separate code branch for shorter time span Alfvénic studies [e.g. Sydorenko and Rankin, 2013; Streltsov and Lotko, 2008] into GEMINI.

FrAMBOISE is driven by level 3 data products (§E.1 and illustrated in Figs. D-6 and 7.) Observing Scen1-3 contribute different sets of **inputs** to FrAMBOISE. The **output** of FrAMBOISE for all Scenarios is a self-consistently transported and evolved volume of local-scale ionospheric state parameters: plasma density, temperature, flow, currents, and conductivities consistent with the available data inputs - **these outputs define level 3.5 data products for ARCS.**

Scen3 data form the most comprehensive set of inputs for GEMINI. The auroral precipitation average energy and total energy flux maps (inverted from GBO data) serve as kinetic energy inputs at the top boundaries of the model. Flow fields and/or currents (via maps from the STA and/or MAG) are used to construct boundary conditions for the electrodynamics of GEMINI, and the tomographic electron density (reconstructions from eTOMS) are used to set the local initial conditions within the model volume. GITM, driven with AMIE or LFM convection and precipitating energy flux, provides global ionospheric state and defines local boundary flows for GEMINI.

For Scen2, information about the auroral precipitation is instead provided by the volumetric electron density reconstructions from eTOMS. The resolution of the tomographic reconstruction is larger scale than the GBO reconstructions in terms of helping to constrain conductivities but is valuable for both validation and for statistics.

For Scen1 we have a large suite of in situ measurements, providing both current (from magnetic field) and electric field, and thus Poynting flux maps. This allows us to estimate conductivity via the current continuity equation and to utilize the Poynting theorem to provide a specification of average energy and total energy flux [Robinson, 1985; Richmond, 2010]. This type

of scheme (referred to as "in situ" conductance determination) is certainly not as accurate as having optical data but unlocks the largest number of datasets for study with FrAMBOISE.

In situations from any scenarios where scintillation has been observed, density structures from GEMINI are used as input to SIGMA to model scintillation from these structures. This allows the study of cascade and irregularity generation, together with the connection to the mesoscale energy inputs coming from the magnetosphere, including dependence on geomagnetic activity.

Multiple points of *validation* are purposefully included in FrAMBOISE to allow for *robust error assessment* of the level 3.5 data products - the model output. Points of consistency and error analysis include: (1) critical comparisons of modeled GEMINI-GLOW optical emissions vs. GBO data, (2) simulated scintillation which are comparable with eTOMS phase/amplitude time series, (3) local ground level magnetic perturbations over Alaska - which can be compared against magnetometer chain measurements, (4) mean electrojet polarity and intensity comparison with MAG observations, (5) comparisons of conductivity reconstructions with and without optical data, (6) tuning of tomographic reconstruction using optical reconstructions of conductance, and (7) consistency of thermal electron temperature with estimates of S/C potential derived from STA data analysis (§E.3.1) [Siddiqui et al., 2011]. Without these it would not be possible to assign confidence to level 3.5 data products.

The number of expected Scen3 datacubes is (conservatively) estimated at 50-100, and statistical rigor must be achieved through the much larger number (2000+) of in situ auroral crossings. Hence, all scenarios are critical to the proposed work - the ground-based imagery represents virtually the only efficient way for us to interpret precipitation events over a large region with temporal context and with resolution high enough to address our science objectives, while the space-based data provide a statistical backbone to complement case studies.

D.2.3 Closure: demonstrate how data products fulfill science requirements, and quantify

Minute to sub-minute time resolution for the highest-spatial-resolution maps, from 18 sec to 60 sec, is sufficient for the discussions below; the faster of these time resolutions allows a greater range of auroral forms to be quantified.

Closure for SO-1: To map, characterize, and classify mesoscale electromagnetic structures, we look for a diversity of activity levels, substorm phases, and auroral morphologies within premidnight behaviour. Each of the expected 2000 in situ crossings produces a temporally evolving, in situ "movie" of electric and magnetic fields as the swarm moves across its 12-minute pass. This allows us to identify commonalities in physical parameters and processes present via machine learning (ML) techniques and modeling with FrAMBOISE.

ARCS Scen1 maps of electric field, field-aligned current, and Poynting flux are used to study spatial and temporal correlations between these parameters in the premidnight auroral zone. Closure for SO-1 is defined as a quantification of the gradient scale lengths, structure sizes, correlation lengths, and temporal coherences of electric and magnetic phenomena for a diversity of auroral forms and geomagnetic activity levels. Scen1 statistics will also be used to catalog occurrence of Alfvén waves in relation to current structures.

Relationships between the various mesoscale structures can be explored with ML techniques. The estimated 2000+ ARCS passes provide a rich data set of flow vectors, since each pass event is sampled by 32 spatially-distributed spacecraft at a high temporal (and hence spatial) resolution. We can train (e.g., Bortnik et al., 2016, 2018) the observed flow velocity fields against maps of in situ magnetic perturbations, to learn observed relationships.

Closure for SO-2: Scen2 data allow detailed studies of sources of mesoscale ionospheric density structure coincident with auroras; providing new insights into the role of auroral currents and flows in affecting ionization enhancements, convection of plasma density structures, cross-field transport of ions in the E-region, formation of density cavities adjacent to arcs, redistribution of plasma through upflows, and connections of observed mesoscale density structures, fields, and currents with scintillation-producing density structures at smaller scales. Closure for SO-2 is defined as characterization of density structures (both E- and F-region) in the vicinity of auroras in terms of the occurrence rates for

various features, relative locations with respect to the currents, evolution of these features, and connection to energy inputs.

Closure for SO-3: SO-3 relies on FrAMBOISE reconstructions of volumetric (3D) ionospheric state and dynamics given flow and precipitation inputs. FrAMBOISE also provides the crucial ability to do term-by-term analysis of conservation of mass, momentum and energy in the ionosphere, leading to clear inferences connecting ARCs-measured maps (energy inputs) and ionospheric behavior (which we define as closure for SO-3), particularly density structures at medium scales, Joule/particle heating effects, polarization effects, transport and chemistry/ionization, irregularities, auroral proper motion, and connection of Alfvénic structures to visible aurora. Case in point: answer the longstanding question of why there are more discrete arcs in nightside ionospheres [Newell, 1996; Borovsky, 1998]. Detailed Scen3 datacubes generate case studies with a high level of physical detail, which are used for error assessment for the less detailed datacubes. ML techniques are to be used to investigate connection of flow and field-aligned current patterns to visible auroral images with a focus on providing physical constraints to models and allows, potentially, for a prediction of flow features associated with various auroral forms. The primary algorithm for this ML spatio-temporal reconstruction is the Artificial Neural Network [Bortnik et al., 2016; 2018; Chu et al., 2017a; 2017b; Camporeale et al., 2019].

The mission as defined here in §D.2 is the **ARCS baseline mission**.

D.3 Threshold Science Mission

The ARCS threshold mission design couples descope (planned build of fewer spacecraft), and reliability (estimated operational reliability of the observation points.) Our baseline mission consists of 32 CubeSats; our threshold mission reduces this number to 24 by optimizing a tradeoff between descope and reliability. It is important to note: the goal of ARCS would be severely compromised if the number of in situ observation points drops below 16. If the longitudinal index of the array lattice is reduced, either significant local-time-span coverage or significant cross-track resolution are lost. If the latitudinal index of the array lattice is below 2,

the space-time disambiguation is not realized. Thus, we are proposing to **build a 32-spacecraft baseline mission**, holding 8 as a potential descope for a **threshold mission which would fly 24,** resilient to anomalies in order to maintain at least two observation points per track in every plane. If both the descope and the resiliency factor come into play, our threshold mission retains its scientific value. §D.4-7 and §E.3 describe an OSSE (Observing System Simulation Experiments) calculation exploring the degradation of the reconstructed flow fields as a function of loss of spacecraft; similar quantifications can be done for the other data products. Similarly, we are proposing to build a 32-station GBO network. However, in the case of GBO our baseline and threshold mission designs are the same.

The ARCS threshold mission includes all baseline science objectives with a moderate reduction of time resolution for STA and MAG mapped data products, and a larger uncertainty for eTOMS data products (§D.5.2). It exercises a descope option reducing the number of satellites per orbital plane from 4 to 3. ARCS has satellites in eight orbital planes so this descope represents a decrease in on-orbit satellites from 32 to 24. The descope does not include removal of instruments, given the low number of different instruments and the importance of having each satellite identical to one another for cost saving purposes.

The ARCS unprecedented local CubeSwarm density is made possible by choosing a high-heritage economically produced spacecraft bus suited to our mission region and duration, where we achieve required mission reliability through redundancy, together with pre-launch integration and test to deliver robust satellites for launch. Our flexible mission design criteria and science requirements are resilient, as described in §D.4-7. The **24 satellite threshold mission** allows ARCS to meet all of its science objectives with some loss of time resolution, and increased eTOMS uncertainty. Sufficient fuel margin is available to adjust the orbital planes of the CubeSats should outages occur preferentially in a single orbital plane (§F.2, Table F-5). Finally, reliability analysis is planned in Phase B in order to provide the technical basis for the number of CubeSats to be descoped versus the number used for on-orbit redundancy.

The ARCS **threshold mission of 24 satellites** is the first ever closely spaced swarm of satellites. The CubeSwarm and associated GBO are ideal to make crucial measurements at auroral mesoscales; it is made possible by recent and significant technology advances in small satellites, ion propulsion, advanced manufacturing, and camera technology.

§D.4 THRU §D.7 BELOW IS NEW MATERIAL SINCE STEP 1 PROPOSAL, AND IS DESIGNATED WITH MARGIN-COLUMN BARS.

D.4 Science section additional descriptions for resolution, sufficiency, and closure

Sections §D.1 through §D.3 above remain unchanged from the original Step1 proposal (other than minor corrections and amendments called out and tracked as required for the CSR). In these added sections below, we address aspects of the Science mission that benefit from fuller explanations, centering on more precise descriptions of ARCS science closure. Closure requirements for the **discovery** aspects of Science Objective 1 "SO1: what are the maps", and the **linkage** aspects of "SO2: how do they evolve together", define the resolutions and observational span that are required. Closure on the **understanding** aspects of "SO3: auroral system science questions", places requirements on both resolution, and on data sufficiency.

In §D.5 we show examples of how ARCS closes on its science objectives, both in its baseline and its threshold variants. In §D.6 we address the data sufficiency requirements defining how ARCS data are generalizable enough for closure. In §D.7 we address resolution requirements, and then close by returning to how we justify our definition of the measurement array, both S/C and GBO. These various pieces tell the story of closure, for instance, of SO1, i.e., "what are the gradients, and, what are they the gradients of?" We need to make clear, for instance, why we do not prefer 4 sequential single S/C crossings one minute apart: this choice does not allow a "snapshot" of the 2D structure of the arc. ARCS must measure both the width and motion of current sheets and flow structures, not merely the time dependence of an assumed spatial structuring. The array choice definitions, then, are a consequence of closure requirements, and are resilient to possible degradations of resolu-

tion and to threshold choices.

Consider what is meant by resolution in a multipoint heterogeneous mission. We need to detail both uncertainty on the measured quantities (flow vector error, deltaB error, density error, image inversion data product error), as well as spatial and temporal resolution of the distributed data products -- the maps -- generated by a CubeSwarms's-worth of these measured quantities. How the data are combined and used involves tradeoffs between temporal and spatial resolution, and availability of different scenarios of data products. We introduce the idea of a 2-level map of resolution in Figure D-9, having truly multipoint spatial resolution (S/C to S/C at a given instant) together with, at each observation point, fine-scale single-S/C along-track resolution (over an 18 sec interval as one S/C moves to the position of the next). Combining the data sets for different spans of data collection cadences allows localized-single-point resolution for gradients embedded in truly multipoint spatial map resolution. The roughly 150 km S/C-to-S/C resolution for the 2d multi-S/C map of observations, with 0.5 km single-S/C resolution at each S/C for spatial gradients, allows us to construct a "map of gradients" exploring the edges of disturbances in the context of the auroral system. Throughout §D.4-7, we develop the arguments for our choices of array spacing and span, as summarized in Table D-3 at the end of §D. With these resolution definitions in place we can clarify what is meant by "moderate reductions in time resolution" as various aspects of the heterogeneous array are degraded from baseline to threshold levels.

Our OSSE, built on the physics-based GEMINI numerical model, generalizes and expands on the standard OSSE setup to move beyond simple quantification of expected measurement error, generating dozens of 300 s duration varied synthetic datasets using GEMINI. These were driven with inputs consistent with what we know about auroral forms from the literature and sampled through STK-generated orbits as idealized sources of synthetic data in 3 ways (Fig. D-10). We demonstrate an end-to-end representation for closure:

1. Resolution: In standard OSSE format, we use virtual observations to quantify expected derived-quantity resolutions in different situations:

- A **scraper tool** is used to extract virtual observations from input-generator driven **GEMINI-created** synthetic datacubes, given the STK representations of the S/C trajectories through the ionosphere and over the GBO.
- **Reconstructor tools**, for flow vectors, magnetometry, tomography, and simulated auroral emissions, are used to create uniformly gridded maps from the scraped virtual data, incorporating different levels of measurement noise and S/C health.
- **GEMINI runs** are then in turn driven by these variously-degraded reconstructions, with noisy observations, missing observations, or increasingly non-ideal arc structures. These GEMINI runs are then quantified against the original synthetic-data GEMINI datacubes; the **metrics** for these comparisons are a science study in and of themselves.

2. Sufficiency: Synthetic data from GEMINI are used to quantify families of auroral arc studies by creating hypothesized arc structures to quantify testable hypotheses. Here we quantify

Figure D-10. OSSE and synthetic data flow plan, three ways.

how many observations of different types of events at different levels of observational quality (Scen1, 2, and/or 3) are needed for generalization. That is, we explore the number of observations needed to move beyond case-study observations, toward generalizable statistics and pattern recognition.

3. Closure: Finally, we exploit ensemble, assimilation, and aggregation tools, including machine learning (ML) studies, to illustrate bringing our studies to closure. In our closure examples in §D.5, we use GEMINI to create hypothetical data fields illustrating examples of exciting science results, here labeled as 'top' results for each of our Science Objectives. In our sufficiency examples in §D.6 we illustrate generalizing from Scen1 (in situ only) out to Scen 2 or Scen3 (in situ with GBO and/or eTOMS) using an ML algorithm developed with GEMINI runs that can be validated with Scen3 data; this inversion problem extracts the conductivity throughout the model volume from the F-region flow (i.e., electric field) and field-aligned cur-
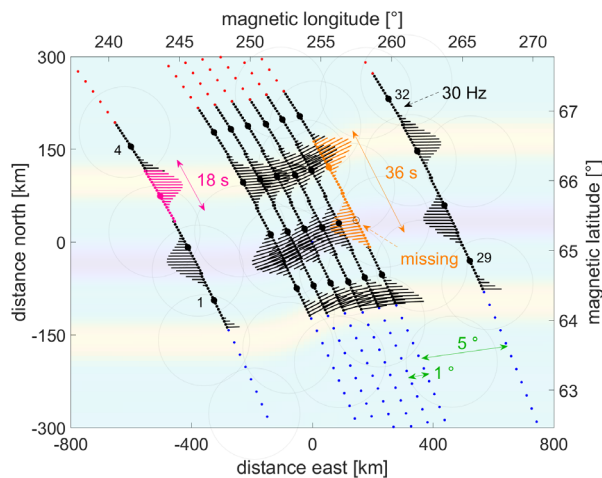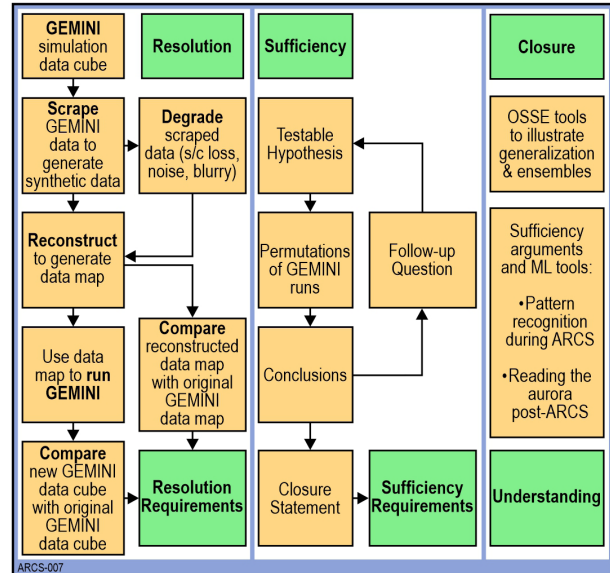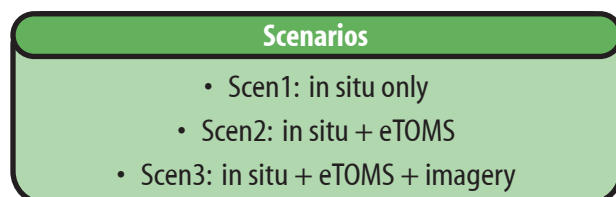

Figure D-9. CubeSwarm array resolution definitions. The aspect resolution of this and OSSE figures is chosen to highlight cross-arc gradients. An 18 s data capture of flow vectors is illustrated for the array; pink vectors show the capture from one spacecraft (decimated for visualization; the full 18 s capture includes 540 vectors per s/c); orange vectors show a 36 s capture by a spacecraft near a missing spacecraft. The underlying color map illustrates a reconstructed scalar field of the eastward component of the flow vectors in the region. See Figure D-20 *for a sequential example.*

Scenarios

- Scen1: in situ only
- Scen2: in situ + eTOMS
- Scen3: in situ + eTOMS + imagery

rent maps. Overall for the ARCS mission, we aim to codify our closure by reconstructing in situ signatures from ground-based imagery, through training an ML algorithm using the full ARCS database; this is what we mean by "reading the aurora".

D.5 Closure
D.5.1 Baseline mission closure

SO1, our **Discovery** objective, is "**Map** the 2D mesoscale structure and temporal evolution of plasma flows and currents in the auroral ionosphere." The maps produced by ARCS, at the spatial resolution, cadence, and quality defined in §D.7, with sufficient number and diversity defined in §D.6, address this objective. The diverse (viz. spanning a wide range of pre-midnight auroral phenomena) and numerous Scen1 and Scen2 events, validated by the detailed case studies of Scen3, over the defined parameter space of premidnight auroral structures, characterize what these flows and currents look like and how they evolve and move for different driving. Figure D-11 illustrates an example 'top' result for SO1: a map of flow and current structures around a westward traveling surge (WTS) -- encoded in our models as an arc with a westward propagating (at 1 km/s) fold structure.

Exploration of the simulated density volume finds a density disturbance in the wake of the bend, which results in the generation of severely non-sheetlike currents even though the imposed precipitation current is sheetlike. In this simulation GEMINI is showing parallel currents that correspond to gradients in conductivity as well as to an enforced flow and precipitation pattern. This example shows that even relatively smooth system inputs (precipitation and flow) can result in sub-

stantial deviations from ideal current structure. This ionospheric-conductivity driven structuring is then a possible basic element of a surge head illustrating the potential role of the ionosphere in determining the evolution of WTS behavior - something to be explored with ARCS. The lower panels of Figure D-11 illustrate how the ARCS in situ observational span and resolution enable closure by capturing the details of this mesoscale event. With ARCS observations, we can directly measure, for the first time, the co-existing flow and current fields around such structures; understanding the ionospheric role in controlling WTS behavior is an open question in ionospheric system science to which ARCS provides closure.

SO2, our **Linkage** objective, is "**Determine** how these 2D maps of plasma flows and currents self-consistently evolve in conjunction with auroral ionospheric density responses." ARCS's evolving maps of flows and currents, coincident with ionospheric density volumes, with suffi-
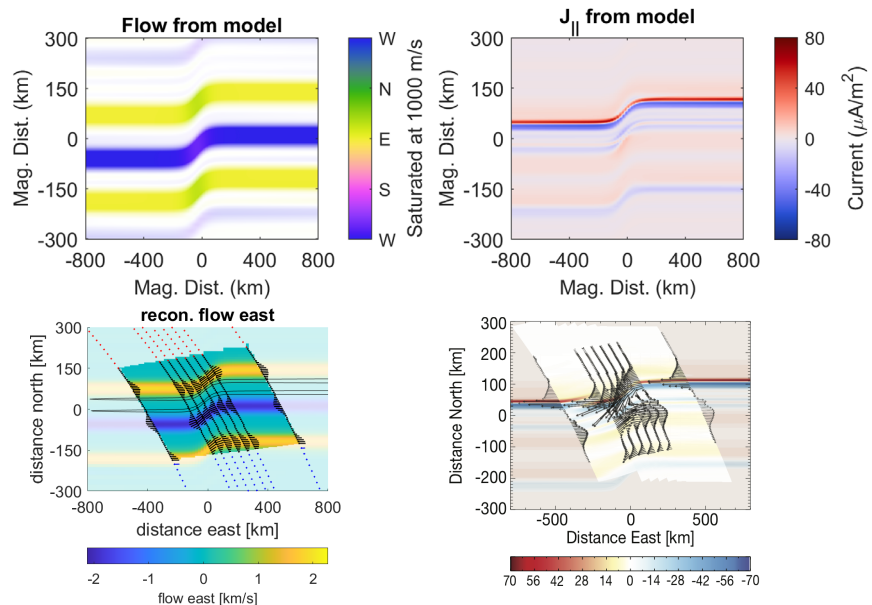

Figure D-11. Example 'top' result for SO1: a map of flow and current structures around a westward travelling surge (to the extent this can be presently modelled with a GEMINI OSSE). Top panels: GEMINI data slices of flow (left) and current (right). The model flow field is represented in HSV format, with color indicating direction. Lower panels: OSSE reconstructions of scraped 32-point observations. Horizontal black-line contours on the flow field reconstruction indicate the location of two narrow precipitation arcs in the GEMINI model input. Black vectors, lower left: measured flow vectors; lower right: measured dB vectors.

cient resolution, diversity, and quantity, together with GEMINI, stitch together auroral conductivity volumes permitting new insights into the behavior of the premidnight auroral lower ionosphere. Figure D-12 illustrates a second 'top' result for SO2: dark winter vs sunlit summer pre-magnetic-midnight density volumes and their related flow-current maps, inferred from a 3-d volumetric evolving density cube, for non-idealized, non-sheetlike discrete arc structures.

The FAC modeled by GEMINI for the narrow precipitation structure response is quite similar in both cases as the return current is predominantly sourced by gradients of the precipitation-induced E-region conductance gradients (clear in the central panel density profiles). However, the flow shears near the arcs are able to source much larger currents in the sunlit summer ionosphere than in the winter one (left panels), changing the broader context in which the aurora interacts with background convection. The sunlit F-region densities (center and right panels) allow current closure of up to 5-10 uA/m^2 over broad regions without the formation of potential drops and narrow precipitation regions. This was supposed by Newell [1996] in the paper "Suppression of discrete aurorae by sunlight." The ARCS span and resolution of F-region measurements, together with tomographic and/or inverted imagery information about density volumes, al-

low determination of the role of the ionospheric density in determining the relationship between F-region flow and current structures - an open question for decades for which ARCS provides closure [Borovsky, 1998].

SO3, our **Understanding** objective, is "**Determine** the roles of the physical mechanisms regulating the relationships between the flows, currents, precipitation and auroral forms in the nightside auroral ionospheric system." The full ARCS data set, including both the numerous Scen1 and Scen2 cases and information rich Scen3 cases, drive a large and diverse set of data-driven GEMINI runs sufficient to generalize behaviour over a variety of circumstances, as listed in Table D-2. Figure D-13 illustrates a third 'top' result for SO3: isolating various terms of the continuity equation which source field-aligned currents in different situations. This result exemplifies how addressing SO1 and SO2 cascades into addressing SO3: **maps** of flows and currents, together with the **evolving ionospheric density datacube**, allow rigorous examination of the **system science** of specific auroral morphologies.

Figure D-13 reveals, through a GEMINI model run of a WTS event with a 3 km/s westward velocity, the underlying physics of the type of current structuring described in Figure D-11. The density cut shows the plume in the wake of
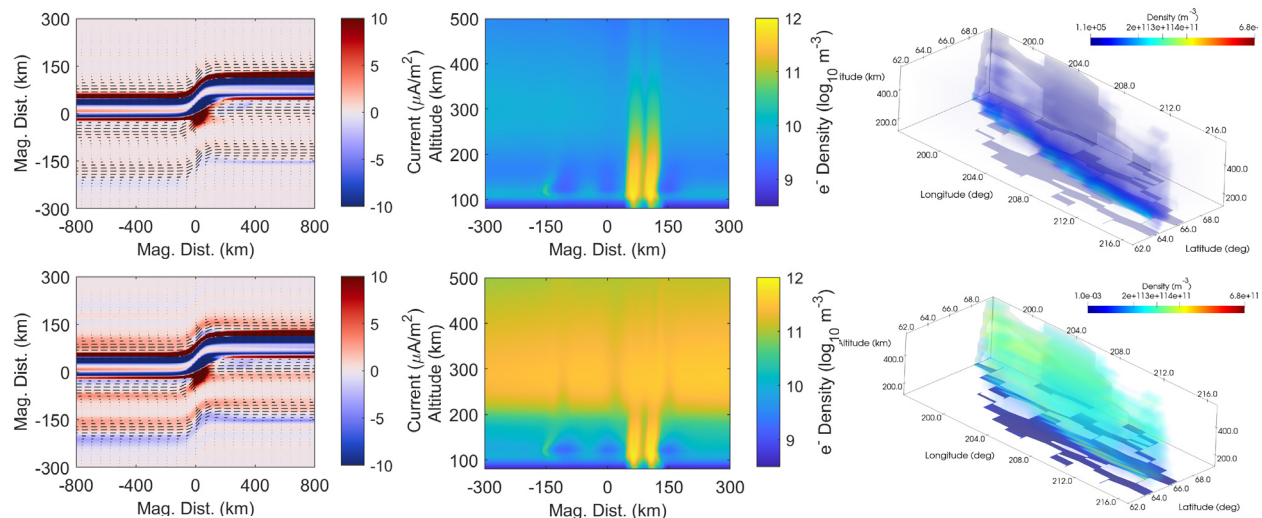
Figure D-12. Example 'top' result for SO2: Dark (February, top) vs sunlit (June, bottom) flow/current linkage inferred from a 3-d volumetric density cube. (left and center) GEMINI data slices of parallel current (color map) and plasma flow (black arrow overlay) in the horizontal plane at F-region altitudes, and of plasma density in a (north, altitude) central cut of the model space. (right) eTOMS OSSE reconstructions of the February and June ionospheric volumes.

the moving arc structure, ostensibly leading to the development of non-sheetlike FAC sourced by the gradient of the Hall conductance in the current continuity equation. ARCS measurements, with non-ideal flow fields constrained by high fidelity imagery, and pairing observational and calculated FAC fields, allow understanding and closure of how the conductivity distribution affects the development of the surge head non-sheetlike FAC.

These examples of generalizable results illustrate how ARCS answers auroral system studies questions. Post-mission, in aggregate, ARCS provides training data sets for ML tools, trained on the disparate observations that the mission collects over its lifetime. This ML model implicitly incorporates all the physical interrelationships in the system, which then are extractable by a number of standard interrogation or interpretability techniques: thus by ARCS, we learn to read the aurora, assisting in closure of SO3.

Finally we provide two examples of significant science questions that incorporate all three science objectives. First, to what extent is the quasistatic current continuity equation (§D.1.1) an accurate description of ionospheric behaviour? Sounding rocket case studies [Zettergen, 2014; Lynch, 2015; Clayton, 2017 and 2021] illustrate the surprisingly broad scope of usefulness of the quasistatic approximations. In what regimes does this break down? Furthermore, when are the height-integrated representations appropriate, and are any key physics missing, for example the effect of imperfect parallel mapping of electric fields at small spatial scales and fast time scales [Forget et al., 1991; Knudsen et al. 1992]? These questions can be addressed with

ARCS because the three key electrodynamics parameters - electric fields, currents, and conductivities - can be estimated independently. **E** and **J**$_\parallel$ are measured in situ, and can be used to estimate conductivities, which in turn can be validated using eTOMS and GBO optics. Discrepancies will be quantified as a function of auroral type, and then used to search for and isolate missing physical effects.

Second, what role does the ionosphere play in regulating magnetospheric drivers of auroral phenomena? ARCS will sample the "load" portion of the auroral circuit, which also includes a magnetospheric generator and M-I coupling medium, both of which are outside the region of ARCS measurements. However, their properties have observable consequences in the ionosphere (Fig. D-14). The Newell [1996] paper ends with the sentence: "Indeed, out of 22 mechanisms proposed for creating discrete aurorae, only the ionospheric conductivity feedback mechanism explains our result that discrete aurorae are suppressed under sunlit conditions [Newell, 1996]." For example, an ideal current generator in the magnetosphere may impose a relatively unstructured FAC pattern which, coupled with structured conductivities, will lead to a structured flow pattern. In the opposite limit, a mesoscale magnetospheric potential field coupled with structured ionospheric conductivities, will lead to a structured current pattern. Comparable amounts of structuring would indicate more evenly-matched ionospheric and generator impedances. There are few self-consistent models of the auroral generator [Borovsky et al., 2020], and the ARCS observational constraints will serve as a valuable tool for achieving a workable generator model.

D.5.2 Threshold mission time resolution

The ARCS threshold mission is defined by the simple reduction of the baseline S/C array, decreasing from the nominal four magnetic-latitude-aligned lines of eight S/C (flying 32 for a resilient base-
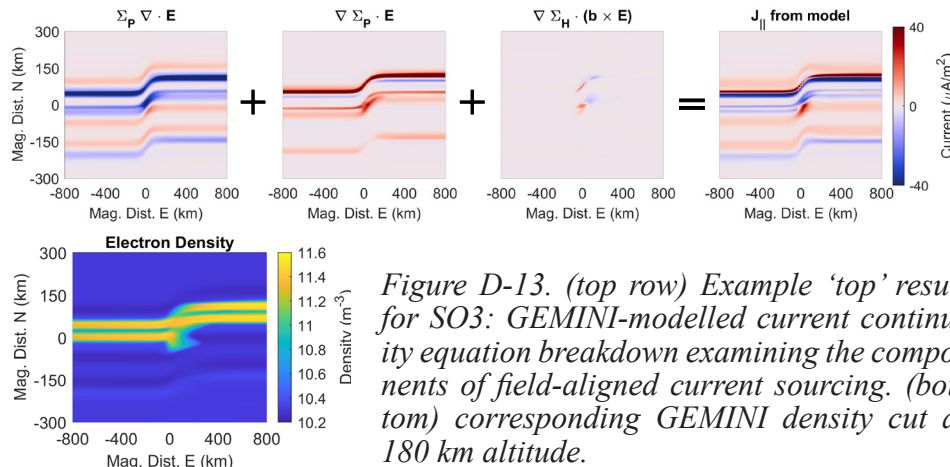

Figure D-13. (top row) Example 'top' result for SO3: GEMINI-modelled current continuity equation breakdown examining the components of field-aligned current sourcing. (bottom) corresponding GEMINI density cut at 180 km altitude.
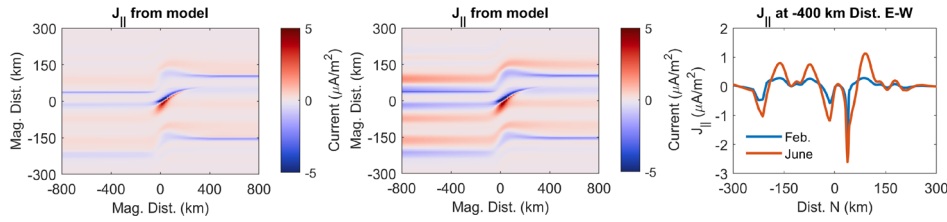
Figure D-14. Demonstration of sunlit ionosphere (center) sourcing FAC from flow shears only, vs dark ionosphere (left) not doing so. These GEMINI runs are driven by the flow patterns, and ionospheres (Fig. D-12) but without imposed arc precipitation. The sunlit ionosphere can source broad regions of several uA/m^2 FAC without localized precipitation regions.

line array of 24 S/C across this lattice); down to three such lines (flying 24 for a resilient threshold array of 16 S/C). Figure D-15 illustrates that the net effect of this reduction is a reduction of our nominal time resolution, turning 18-second frames of data collection, into 36-second frames. (For eTOMS, the effect is an increase in uncertainty; for GBO, there is no change for the threshold mission.) All other aspects of resolution and sufficiency as defined for the baseline mission are unaffected by this change.

Figure D-15 shows that for the threshold mission in its minimal state, with its minimum requirement of 16 in situ measurement points, twice the S/C travel time is needed to span an auroral structure with full along-track data. The images show an overlay of a discrete auroral arc as observed by the KIAN imager of the THEMIS-GBO [Mende, 2009], by the flow vectors of a scrape of a GEMINI run by either 24 (left) or 16 (right) S/C, for either 18 sec (left) or 36 seconds (right). (The image, and the GEMINI run, are not coupled in this figure, other than both being of a discrete auroral arc.) During the timespan of the collection, the arc moves and evolves. In the example baseline observation shown, a random choice of 8 S/C are missing; in the example threshold mission shown, the array is presumed to be reordered to maintain at least 2 S/C per track. The highlighted pink vectors in each case illustrate the swath of flow data collected by S/C position 3 (left), or 2 (right) over the course of the frame. The net cost of the reduction to the threshold mission is a limiting of the scope of auroral motions and structures that can be space-time disambiguated: arcs moving or evolving rapidly on 30-second timescales will be more blurred, and only 2 rather than 4 fully-independent frames of a structure on the

scale of the array span can be captured during a crossing. More examples of this framing are shown in §D.7. The in situ field illustrated by Figure D-15 (right) remains a distinct leap from present single- or few-S/C views of auroral structures, and would be worthwhile albeit limited from the preferred rich baseline mission.

This reduction to the threshold mission definition preserves the resolution (other than the factor of 2 in net in situ frame time resolution) and sufficiency for ARCS. Further reductions in the designed S/C number would prevent any significant space-time disambiguation, and would not allow the mission to be worthwhile. As we illustrate below, occasional holes in the defined S/C array can be corrected for with the reconstructions, such that the baseline 32-array is resilient down to 24 operational S/C at a given time. Similarly here in the threshold mission, some points of the 24-S/C array could become non-operational without crippling the reconstructions. However, reductions below 16 mea-
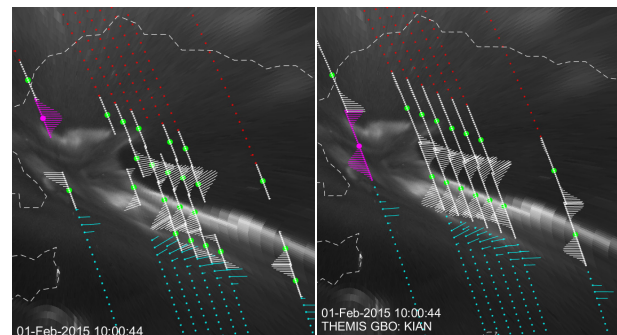
Figure D-15. Reduction of time resolution caused by dropping from the baseline to the threshold spacecraft array design. The white feathers illustrate a scrape of a GEMINI model flow field, overlaid on a THEMIS-GBO from from KIAN (Mende, 2009). Data must be collected for 36 seconds to fill the threshold span (right, threshold) rather than 18 sec (left, baseline). Vectors from a single spacecraft are highlighted in pink. Vectors from times previous to the shown array footprint are in blue.

surement points, such as to a single line, or to sets of 3-4 S/C, would be too like existing missions such as ESA-Swarm to be worth the effort expended. The defined threshold mission maintains the essential elements of the ARCS multipoint study at the cost of a limited reduction in time resolution.

D.6 Sufficiency

Generalizing observational results for science closure requires a **sufficiency** of data. In this section we detail data sufficiency requirements for diversity and number, and the ARCS mission capability of meeting them in a resilient fashion. There are three data collection scenarios: Scen1, in situ only; Scen2, in situ crossing of the GBO array with TEC but no imagery; Scen3, in situ crossing of the GBO array with valid imagery. There are 24 contiguous months of science data collection. In the summer months (§E), auroral imagery is not available in the Northern Hemisphere, but in situ and tomography data remain scientifically valid and valued.

The essential requirement for sufficiency is that we move beyond individual-auroral-crossing case studies into generalizable observations. Scen3 observations form the most complete crossings; interpretations of these crossings are used to validate the much more numerous Scen2 and Scen1 observations. These more numerous observations provide the statistical heft for generalization of the deep Scen3 observations.

D.6.1 Scen1: in situ data sufficiency

Diversity and number of map examples expected: In situ data maps of flow fields and current structures are collected for three Northern Hemisphere nightside auroral zone crossings every day for the two-year science phase, providing a database of two thousand such crossings. Two-thirds of these are designated Scen1 in that they are not over the Alaska GBO. One-third are part of either Scen2 or Scen3. Overall there are 2000 in situ crossings. Data are collected year-round, covering seasonal dependences of premidnight aurora over a two-year cycle. We expect to be in the declining phase of the solar cycle, and can expect a substorm cycle rate of 5.5 substorms per day, based on the number of substorms observed during a similar phase of solar cycle 24 [Newell and Gjerloev, 2011]. As typical substorm life cycle durations are about two hours, this means

that at any given time, there is a 45% chance of being "in" a substorm. Multiplying our 18 min/day (taking the central 6 minutes of each of the three 12 minute science passes) of pre-magnetic-midnight central-auroral-zone data collection cross section with this 45% density of expected substorm activity allows us to predict an intersection with 18*720*0.45 = 5800 minutes of 32-point in situ recorded substorm activity.

The 2014 ground-based imagery mosaic shown in §E illustrates the diversity of auroral activity that was recorded in central Alaska over the course of a winter season in solar cycle 24. Much of the premidnight auroral zone diversity can be organized around the substorm sequence. We can collect hundreds of examples covering the different phases of substorm sequence, as well as hundreds of examples of quiet arcs. This large number allows generalization of the ionospheric science implications we extract from each event.

Ability to interpret without context of GBO: In order to make use of this large number of in situ crossings, we need to be able to "connect-the-dots" between the multipoint S/C observations in a coherent manner. The reconstructions generally assume knowledge of the line of the "arc boundary", that is, the coherent boundary of a longitudinally extended auroral structure, along which the activity is assumed to have minimal variance. This allows us to combine the fine-scale structure of the along-track observations, with the across-track spacing, in an informed manner. For events with no ground-based imagery, we are able to reproduce this constraint in several ways. The simplest is knowledge that most auroral arcs are aligned to a line of constant MLAT [Gillies et al., 2014]; indeed this is why our array is aligned to magnetic latitude. This however is overly idealized and we want to allow for non-aligned structures. As long as the structure has a coherent sheetlike envelope, even if the sheet is distorted, maximum-variance analysis of the in situ magnetometry [Sonnerup and Scheible, 1998] allows us to extract from the in situ magnetometry data a proxy for the inferred arc boundary. Figure D-16 illustrates such a reconstruction of a flow field using only the arc boundary inferred from the in situ magnetometry. For simple arc structures (left panel), the two boundaries are quite similar; for faster-moving structures (right panel) the two defini-

tions of the boundary can vary but the resulting reconstruction remains viable (Table E-5).

Ability to invert with GEMINI and Poynting's Theorem constraint: Measurements being made for ARCS Scen1 crossings will result in the production of reconstructed data maps (2D fields) of parallel current density and electric field (flow field). These measurements may be directly used to also produce derived data maps of Poynting flux. In the case of Scen1 data, key unknown physical parameters are ionospheric Pedersen and Hall conductances - without these one does not have a full picture of electrodynamics and energy flow in the auroral system and cannot unlock the scientific potential of the large amount of Scen1 data collected by ARCS.

Scen1 current density, flow field, and Poynting flux data maps can be related to each other through electromagnetic conservation laws: current continuity and the Poynting theorem. Under assumptions of steady state conditions and equipotential field lines (appropriate at scales relevant to our science questions), these can be reduced to expressions relating current density (the current continuity equation, in §D.1.1) and Poynting flux (for the case of sheetlike arcs [Richmond, 2010]) to the conductances. For sheetlike arc structures, [Richmond, 2010)] shows the Poynting flux can be represented as:

$$S_\parallel = -\sum_P E^2$$

Removing sheetlike assumptions can be dealt with via further analysis shown Richmond et al (2010), which would lead to a more sophisticated estimation method. These conductances may, in principle, be solved by simply inverting this system of equations. However, the component of the Hall conductance gradient along the electric field direction is explicitly not part of this system. Thus in addition to conservation laws additional prior information is needed. For ARCS data processing we have several approaches to adding prior information: (1) regularization that places constraints on solution norm or smoothness (i.e., Tikhonov regularization), and/or (2) inclusion of model information that further correlates Pedersen conductance (which is well-constrained by laws above) to Hall conductance (which requires further constraints). As a final note, the conservation laws used above are subject to assumptions of steady-state, so care will need to be taken to apply them only to DC components of the measurements.

Figure D-17 shows an example that directly computes Pedersen conductance from the Poynting theorem and then combines this information with a linear regularized solution to the current continuity equation to estimate the Pedersen to Hall conductance ratio. Here a regularization based on smoothness and deviation from a fixed Pedersen-to-Hall ratio illustrates that even a relatively simple linear algorithm is able to reconstruct useful information about the conductances from ARCS's 2D maps of current density and of energy flow.

There are other means of achieving conductance estimates. For example constraints could be derived from model-based inversions or simple parameterizations based, e.g., on the Robinson formulas [e.g. Liemohn, 2020; Robinson et al, 1987] or updated versions of these formulas. These approaches would yield nonlinear estimation techniques that directly derive electron precipitation total energy flux and characteristic energy needed to construct GEMINI simulations for these passes. The same precipitation parameters could alternatively be estimated from the Pedersen and Hall conductance output by our example linear estimator using any model of conductance produced by energetic precipitation.

Information content of in situ data alone: Another way of revealing and exploiting connections of flow and current is by training a neural net with combinations of in situ information and conjugate auroral imagery. Figure D-18 illustrates one example of such a process, using the more limited data available from ESA-Swarm
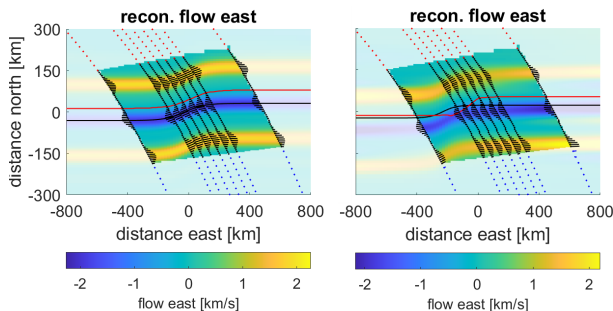

Figure D-16. Reconstructions using magnetometry-based arc boundaries. Red line: boundary from imagery. Black line: boundary from magnetometry. (left) Reconstruction of Figure E-11 *event. (right) of* Figure D-23 *event.*
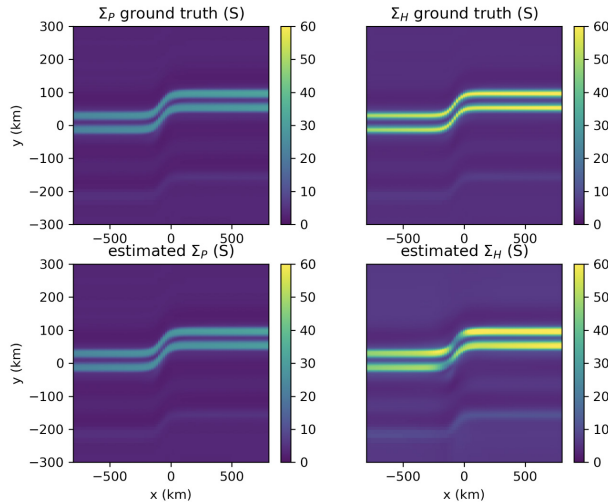
Figure D-17. Example of use of electromagnetic conservation law-based inversion (top left) model Pedersen conductance, (top right) model Hall conductance, (bottom left) Pedersen conductance computed from Poynting theorem, (bottom right) Hall conductance computed using regularized inversion of current continuity equation (with specified Pedersen conductance).

and THEMIS-GBO. Using several hundred crossings of the ESA-Swarm S/C [Knudsen, 2017; ESA, 2021] over various THEMIS-GBO imagers [Mende, 2009], a neural net algorithm was trained to relate features of field aligned current signatures and cross-track flow signatures, to matching features of white-light brightness traces along the trajectory footpoint. In the example shown, the resulting ML algorithm took as input the featurized in situ crossing current and flow information, and predicted the location and magnitude of the matching discrete arc, shown here as a sheetlike swath aligned to a line of constant MLAT. With ARCS, the in situ data are distributed in 2D, rather than limited along a single trajectory, allowing the exploration of non-sheetlike structures even in the absence of associated imagery.

We can use ML tools to infer expected auroral brightness signatures from in situ distributed maps of F-region current and flow, in the absence of imagery. This learning algorithm can be jump-started with existing THEMIS-GBO and ESA-Swarm databases (albeit limited by the small number of S/C and the broadband unfiltered imagery), as shown just above, and expanded and improved using distributed ARCS

data as it becomes available.

Additionally, ML tools can provide an alternate means of inversion of the ionospheric conductivities from in situ maps of flow and current. An Artificial Neural Network (ANN) is trained on a large number of GEMINI model runs (i.e., synthetic data) where maps of accompanying precipitation average energy <E> and energy flux Q from the simulation volume are given, and maps of field-aligned currents and potentials are specified at the upper altitude boundary of the simulation, providing a low-cost emulator of the full physics-based model. When ARCS produces 2D observational maps of the FACs and potentials, the ANN model will be used to estimate the most likely distribution of <E> and Q consistent with the observations. Then GEMINI, constrained by the in situ maps and the predicted precipitation, can be used to calculate the conductivity volume.

While it is difficult to demonstrate ahead of time the efficacy of these ML tools for the ARCS data, we can illustrate the use case above on paired time-series maps of GEMINI-synthetic-data flow, current, and precipitation. We have many already in hand, for all the existing OSSEs and all their timesteps. Figure D-19 shows

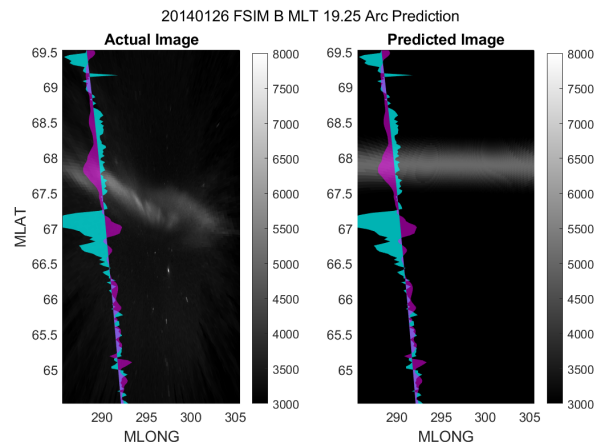*Figure D-18. Example ML neural net prediction of discrete arc based on ESA-Swarm flow (blue) and FAC (purple) signatures over a THEMIS-GBO (Fort Simpson) imager (Mende, 2009). Left image: observed. Right image: predicted arc structure assuming MLAT-alignment. (cite M Kawamura, Dartmouth). With ARCS, the assumption of MLAT-alignment can be relaxed, and featurization can be done using 2D array of in situ data.*

an example of such a prediction using the available database of OSSE GEMINI runs, for the restricted case of paired discrete arcs.

The Scen1 database has exceptional depth and dimensionality; it will produce two-dimensional time-dependent maps of flows and currents for a diverse multitude of Northern hemisphere premidnight auroral zone crossings.

D.6.2 Scen2: in situ plus tomography sufficiency

The nightly Scen2 crossings provide tomographic density reconstructions that are diverse, interesting, and interpretable without imagery context. eTOMS provides necessary validation for GEMINI calculations of density volumes. As with Scen1, Scen2 data also lack optical measurements and direct specifications of precipitation therefrom; yet these precipitation specifications are required inputs for FrAMBOISE. Scen1 inversion can make use of energy and charge conservation laws to compute the precipitation characteristics; for Scen2 we have the additional tomographic reconstruction for plasma density (viz. full 3D volumes of density estimates). There are several established approaches for inverting density profiles to derive auroral precipitation [Semeter and Kamalabadi, 2005 and references therein] parameters. The essence of these techniques is that the height of the ionization layer effectively determines the energy of the precipitating particles while the amount of ionization determines the total energy flux. These algorithms can be leveraged to determine maps of characteristic energy and total energy flux at the native resolution of the tomographic reconstruction of density (within limits of tomography inversion resolution).

An additional consideration that can improve the quality of Q and <E> maps for Scen2 is that the density inversion algorithms can be combined with conservation equations and parallel current
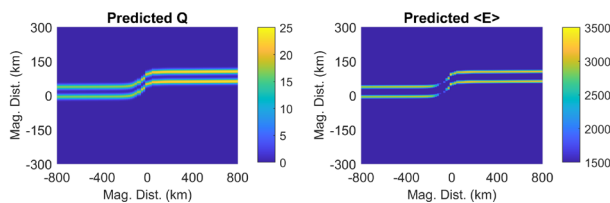

Figure D-19. *Example ML predictions of precipitation maps from flow and current maps, using an algorithm trained on many similar GEMINI runs. RMSE is 3% for both.*

density and Poynting flux measurements. The result will be a larger and more computationally expensive (but not prohibitive) approach that derives a higher fidelity precipitation estimate given constraints from all Scen2. Finally, we also note that eTOMS Scen2 data will provide specifically the F-region plasma density needed for initial conditions in the models. Also of note is that the eTOMS data are available through the summer sunlit-ionosphere months when the imagery is offline.

D.6.3 Scen3: in situ plus tomography plus imagery sufficiency

Sufficiency arguments for Scen1 and Scen2 data are that those data can be interpreted without imagery. Sufficiency arguments for Scen3 data are concerned with showing that there are enough examples for generalization and for validation. The GBO array is resilient to operational and weather outages, as detailed in §E. The statistics of true Scen3 events include the **depth** of their datacubes; these event studies are deep/high-dimensional enough for generalization to the larger-numbers of Scen1 and Scen2 data use.

The 2014/2015 "mosaic" of auroral events shown in §E contains 48 of 100 clear-sky auroral images from 1000UTC in that solar-cycle equivalent year. An examination of these events finds, over a total of 273 days that season, 37 quiet arc events, and 81 substorms, which included 30 storm-time substorms. So the probability of clear sky and auroral events is (37+81)/273 = 0.43, which is remarkably consistent with the statistics mentioned earlier based on the Super-MAG substorm list.

D.6.4 Modelling sufficiency

A standard GEMINI datacube contains the density, 3D bulk velocity, and temperature for six ion species ($O+$, $NO+$, N_2+, O_2+, $N+$, and $H+$), and electrons. The potential, conductivities, and currents are also included. The richness of this datacube provides constraining information for understanding the local ionosphere.

All of the ARCS data can be ingested by GEMINI and used as data drivers (App. L.14.2.4) for simulation runs, using the Scen1 inversions described in §D.6.1, validated by Scen2 and Scen3 observations as well as physics-based synthetic datacubes (3D volumes of ionospheric plasma parameters) created within GEMINI. The ARCS

data are sufficiently diverse to be generalizable into a range of modeling case studies. Finally, it is noted that substantial resources are allocated so that GEMINI can be extended with an inductive component so that we can use it to study Alfvenic auroral fluctuations observed by ARCS.

D.6.5 Machine learning sufficiency

Machine Learning (ML) tools will be used in multiple ways, such as in a Scen1 inversion tool as described above. Separately, ML provides a tool to stitch together all the data collected from all the ARCS crossings under a variety of conditions, at the conclusion of the mission. This includes data from all S/C passes, for all events, with the aim of reconstructing a complete auroral ionospheric state given ground-based information (imagery). ARCS GBO data, together with activity indices, combined with ARCS in situ data, train the ANN model for post-ARCS use. The resulting model will recreate, given ground-based input data, what the ARCS in situ CubeSwarm would have observed over its target region of Alaska given those specific driving conditions, for events after the conclusion of the mission, trained on the disparate observations that the mission collects over its lifetime. This model would thus implicitly incorporate all the physical interrelationships in the system which could be extracted by a number of standard interrogation or "interpretability" techniques. [e.g., Marsland, 2015, p.88; Raissi et al., 2017; Zhu et al., 2017]. These ML use-cases are feasible and will be conclusive.

D.6.6 Summary of sufficiency issues

We close this section on sufficiency by returning to the middle panel of Figure D-10, creating example statements such as "this question requires N ScenarioX crossings for generalization." We can use the framework of FrAMBOISE synthetic datacubes to explore and quantify testable hypotheses. Table D-2 provides an illustrative, though not exhaustive, listing of this class of questions. Table D-2 lists specific science investigations/hypotheses that ARCS data will be used to address alongside the estimated amount of data needed to make substantial progress on each, a citation describing the phenomena of interest in detail, and the top-level, upstream objective to which each investigation

component contributes. These investigations are also categorized according to which scientific objective (SO) they *most* contribute to.

Based on Poker Flat all-sky camera observations from 8/2014-4/2015, during the ARCS mission we expect of order 70 quiet arc and 160 substorm cloud-free events under Scen3. These events will allow us to train and validate the interpretation of Scen2 (seven times more numerous) and Scen1 (twenty times more numerous) observations, to increase statistics. In Table D-2 we estimate the number of different types of events, in the different Scenarios, that would be necessary for generalization. Remember that each arc-crossing event is a 32-S/C 20-100 second datacube, including tomography for Scen2 and imagery for Scen3.

ARCS science objectives are centered around developing a fundamental understanding of plasma flows, currents, and conductances for a wide range of auroral conditions. Indeed new types of auroras are still being discovered today and we struggle to explain how they occur (e.g. ionospheric signatures such as STEVE, eraser aurora, etc.). Parameters measured by the ARCS mission will help define the state of the ionospheric electrical system in auroras and will be used to advance a wide range of topics in auroral physics. These are organized into the general hierarchy of (SO1 -- Discovery) mapping of forcing (flows, currents), (SO2 -- Linkages) sensing or estimating ionospheric plasma responses (e.g. plasma density, current closure, and conductance), and (SO3 -- Understanding) exploring physical connections between electrodynamics of auroras and suprathermal electron precipitation - though many investigations are related to more than one objective as noted. All of these are to be done, for the first time, in a spatially and temporally resolved sense needed to improve our understanding of auroras.

D.7 Resolutions

For the ARCS array, there is not a single answer to the question "what is the resolution of the observations", as this is a multi-dimensional array allowing a variety of optimal uses of the heterogeneous data sources. The framework for interpreting these resolution tradeoffs is through the OSSE. In §E we address both (a) measurement uncertainty and (b) map error for each measurement provider. Here we address (§D.7.1

Table D-2: Data sufficiency for specific scientific investigations (Fig. D-10)		
SO	Investigation/Hypothesis	(Scen:# Needed)
S01	How do mesoscale flow and current structures correlate with large-scale FACs and convection? (e.g. Coxon et al, 2018) (optional use of AMPERE, SMILE UV, and SuperDARN)	Sc1:50
S01	(a) What are flow and current conditions accompanying STEVE/SAID, both with and without the "picket fence"? (b) How do extreme STEVE/SAID flows work to modulate ionospheric conductivity and self-consistent MI coupling? (also SO2) (e.g. MacDonald et al, 2018; Archer et al, 2019) (optional use of ground-based optics/TEC from subauroral regions)	Sc1:100
S01	How do spatial and temporal mesoscales in auroral flows vary as a function of morphology (diffuse, discrete growth, onset, breakup, recovery/pulsating, beads)?	Sc1:200; Sc3:10
S02	How are current closure specifically and MI coupling generally affected by (a) arc proper motion, (b) arc spatial configurations, and (c) precipitation energy flux and spatial distribution? (e.g. Haerendel et al, 1993)	(a) Sc1:100 and Sc3:10 (b) Sc3:12 (c) (Sc2+Sc3):50
S02	What contribution(s) do auroral beads make to overall system level substorm dynamics, e.g. are the bead-associated FACs closed locally? What is the relative balance of FAC sources (electric field structure vs. conductance structure) in beads (also SO3)? (e.g. Nishimura et al, 2016)	Sc3:10; Sc1+2:50
S02	How are variations in FAC related to variations in conductivity, and what implications does this have for self modification (e.g. pinching) of current structures (also SO3)? (e.g. Kan and Akasofu, 1979)	Sc1:100; (Sc2+Sc3):12
S03	To what degree are different types of auroral forms voltage vs. current-driven? Are there well-defined electrical morphologies recognizable from patterns in the imagery? How do daylit auroras differ (e.g. Borovsky, 1998)?	Sc1:100; Sc2,3:10
S03	(a) How do westward travelling surge ionospheric electrodynamics (fully resolved in lat/lon) and responses depend on drivers? (b) What role do streamers play in magnetosphere-ionosphere coupling (Amm et al. 1999; 2011) and ionospheric modulation of substorms? (also SO1+2) (e.g. Marklund et al, 1998; McPherron et al, 2020)	Sc2,3:12; Sc1:100
S03	To what degree are different auroral morphologies associated with Alfvenic features (e.g. PBIs and rays) driven by dynamic (viz. inductive) vs. static electromagnetic features? What role do conductivity gradients and broadband precipitation play in these events? (e.g. Kieling et al, 2020)	Sc1:100; Sc2:20
S03	What effects do auroral flow and current have on the distribution and energetics of the ionospheric plasma vis-a-vis density enhancements, cavities, and regions of frictional heating? (e.g. Zettergren et al, 2012; Zou et al, 2013)	Sc2:25; Sc3:10
Secondary	Topside evolution of equatorial spreadF with ARCS array with Jicamarca conjunctions. (e.g. Burke et al, 2003)	Sc1:6
Secondary	Plasma flow structures in the polar cap, coordination with Resolute Bay Incoherent Scatter Radar/CHAIN. (e.g. Lamarche et al, 2020)	Sc1:100 events
Secondary	Neutral wind coupling to auroral arc systems: dynamo and plasma density effects (e.g. Anderson et al, 2011); Collaboration with ground-based imaging FPIs	
Secondary	How do auroral activations (precipitation and motion) relate to magnetotail current sheet dynamics? E.g. the motion of westward traveling surge v.s. the expansion of plasma sheet flow region (Angelopoulos et al., 2008); Auroral streamer v.s. magnetospheric fast flows flows (Sergeev et al., 2000) and associated field aligned current (Nakamura et al., 2001); Collaboration with magnetically conjugate magnetospheric spacecraft.	

and §D.7.2) the implications of this map error for use of these maps in driving FrAMBOISE, and then finish with a revisit of the justifications for the definition of the ARCS observational platform arrays.

D.7.1 Interpretation of Model Output: effects of input data map quality

§D.2.1, the STM, and Figure D-5 define the parameters of our planned CubeSwarm array. We can now re-examine that definition in light of the resolution descriptions above. Table D-3 lists the array parameter definition in relation to the defined resolutions. The latitudinal span of the array is designed to include the typical spans of WTS structures of ~3-4 degrees in magnetic latitude [Zou et al., 2010]. The 4 along-track rows separated by 18 s of along-track S/C motion mean that in a typical crossing, 3-4 fully independent 2-d in situ snapshots of the full

flow and current structure can be obtained. The GBO span and cadencing allows maps of auroral precipitation estimates at 1 km resolution at 8 Hz, during the swarm overpass, covering the cloud-free portions of a 10^6 km^2 region. For this nominal interpretation, the connection between loss of S/C and time resolution is defined: if a S/C is missing from the array, its data need to be replaced by those of its along-track neighbors 18 sec prior or after, resulting in a blurring of time-dependent structures at that place in the array. Similarly, if a GBO station is offline, its field of view must be covered by other imager stations at oblique angles.

The longitudinal spacing of the array is determined by spanning significant lengths of discrete arc structures with sufficient resolution to examine deviations from sheet-like current sheets and flow structures. As detailed in §D.2.1, it allows study of mesoscale (10's-100's km) beads in

auroral structures and auroral systems such as westward traveling surges and substorm onsets [Forsyth et al., 2020]. The WTS structures are often seen in radars and imagery to move with proper motions and westward velocities around 2 km/s [Craven et al., 1989]. Thus the 3-4 independent snapshots (or a sliding window of time across an arc crossing span) allow study of the evolution of these structures with minimal blurring, particularly if proper motion is accounted for during the 18s data collection span. The upper panels of Figure D-20 illustrate a sequence of such reconstructions of a westward-moving flow field structure. The four frames shown capture the evolving westward surge of the OSSE event. The ARCS array is designed to span and resolve structures at these scales, with edge-gradient resolutions matching the km-scale observed edges for such events, together with the span and time resolution to observe the meso-scale structure of the event as a whole.

Taking the errors detailed in §E for both measurement error, and data map error, as given, we next consider how these mapped-data-product resolutions, either through measurement error or through map error, affect interpretations of the ionospheric state through GEMINI calculations. We compare simulation results for GEMINI runs driven by idealized hypothetical drivers, to runs driven by deliberately degraded drivers. These degradations include adding noise to the measurements, and/or removing S/C or GBO sites from the databases used to create the maps. We can also explore the effects of noise removal and/or smoothing of data that is often part of preparing real data for use as a model driver (often a result of moving from one lattice (such as the measurement points) to another (such as the model space). This exercise defines the worst case scenario that still allows scientific conclusions to be drawn.

We can quantify the degradation of the reconstructed flow field map as a function of the loss of (multiple) S/C. Figure D-21 explores this by reconstructing these fields, for a given hypothetical arc structure, using fewer and fewer S/C. Certainly for idealized sheetlike auroral arcs, a very few S/C can capture the essential elements.
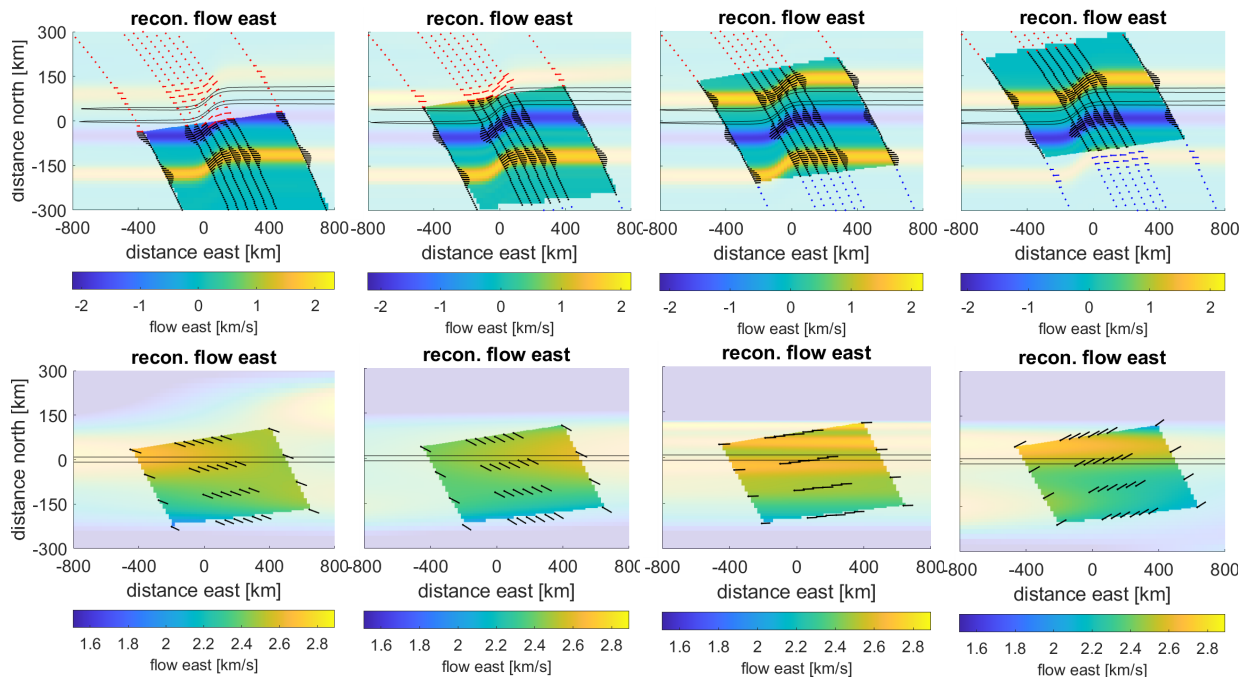

Figure D-20. Two extremes of resolution definitions: (top) Sequential moving-mosaic-tile flow-field reconstructions of a moving discrete structure. (120 m/s southward, 3 km/s westward). Four independent 18-second collections are reconstructed. (bottom) Sequential timesteps of a temporally-focussed reconstruction of a pulsating aurora region. Four separate independent 1-second data collections are reconstructed, ignoring future and past flow vectors.
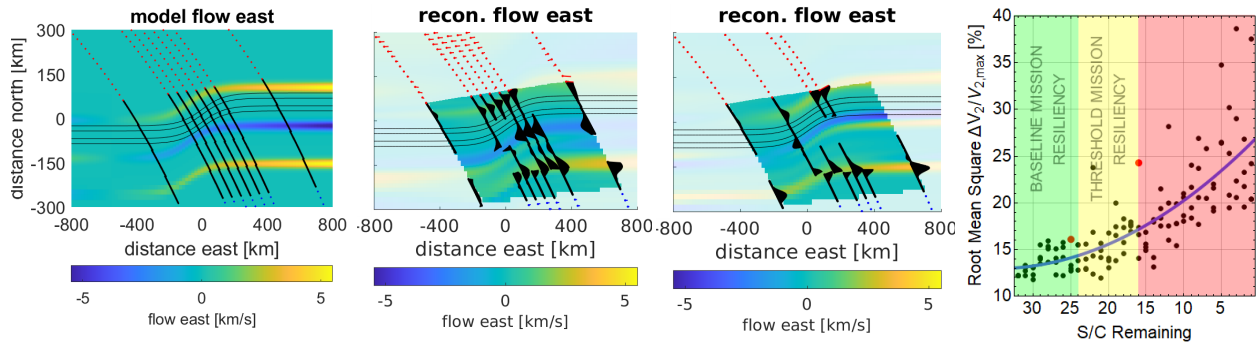
Figure D-21. Flow field reconstructions with 24 spacecraft and with 16 spacecraft; (far left) -- original flow field. (right) -- Scatterplot of metric degradation within the trapezoidal array region, as a function of number of spacecraft used for reconstruction. Green: baseline; Yellow: threshold.

However, for ARCS we wish to be able to quantify flows and currents around non-ideal arcs, so the example structure here includes along-arc spatial variation, temporal variations, and proper motion. The scatter plot of Figure D-21 shows the increasing error in the data map metrics as S/C are removed.

Finally in the last step of the OSSE, shown in Figure D-22, we compare the field-aligned current calculations of GEMINI for (a) the originating hypothetical datacube, (b) a GEMINI run driven by a flow-field reconstruction built from all 32 S/C of that datacube, and (c) a GEMINI run driven by a 24-S/C flow-field reconstruction. The basic GEMINI-resulting current structure is well reproduced in both the reconstruction with no S/C loss and the reconstruction with eight S/C lost. Comparing the field-aligned currents at 500 km, across the whole simulation domain, from these reconstruction simulations, to the original GEMINI datacube slice of FAC, generates a RMSE for (b) of 13.8% and for (c) of 7.7%. It is important to recognize that Figures D-21 and D-22 are meant to be illustrative, not comprehensive. There are many many ways that combinations of differently structured and complicated events will cross with differently arranged observational situations: either from losses of S/C, or from offsets between the location of a particular event, and the placement of the ARCS array.

(Note, for instance, that in the example shown, the 24-S/C reconstruction drives GEMINI better than the 32-S/C one does; consistent with the scatter in Figure D-21 (right), a different realization can "capture" a structure in slightly better or worse ways.) However, for this example, we illustrate a quantification of the degradation of metrics of data map quality, and the degradation of the resulting GEMINI calculation.

Another example calculation involves deliberately degrading the <E> and Q mapped data drivers from precipitation information from the imagery (Fig. D-23). The left panel illustrates the view (obliquity) angle from the nearest GBO station to any pixel in the model space. In this example, the effect of the region without imagers is clear, along with the errors caused in the mapping of the precipitation patterns (here represented as order of magnitude estimates of errors on <E> and Q from obliquity; see §E.3.4.6), which, when uncorrected, result in gaps in the calculated FAC structure.

Modelling Summary: These examples of modelling output datacube resolutions for choices of different situations, using the RMSE metric on
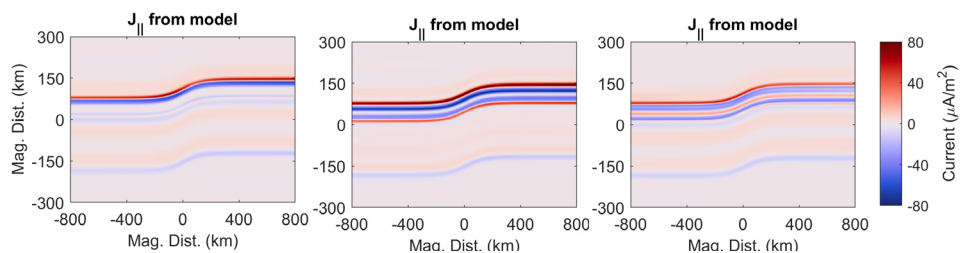

Figure D-22. GEMINI-calculated FAC maps for model runs driven by (a) hypothetical flow map inputs; (b) 32- and (c) 24-spacecraft reconstructed flow fields. RMSE for (b) is 13.8% and for (c) is 7.7%.
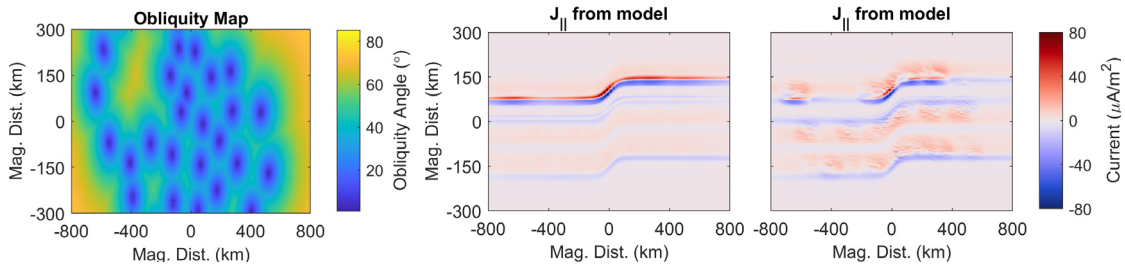
Figure D-23. Driving GEMINI with degraded particle precipitation inputs. Error on <E> and Q is applied either as (center) a cosine function of the obliquity angle for each pixel (at 110km), or (right) a combination of expected imagery noise at a full 8Hz frame rate (co-adding of imagery frames will reduce gaussian noise on the input drivers), together with the obliquity angle effect. RMSE for (center) is 8.2% and for (right) 11.0%.

calculated FAC described above, illustrate that GEMINI interpretations of even uncorrected degraded ARCS data will provide breakthrough science closure.

D.7.2 Summary of resolution and array definition

We close by revisiting the initial observational array definitions of §D.2 and Figure D-5. The CubeSwarm is designed to focus on mesoscale pre-magnetic-midnight auroral arc structures. The focus of ARCS is on evolving discrete arc structures, and it is a clarifying counterpoint to consider an event with substantial temporal structure, as shown in the lower panels of Figure D-20. In the lower panels, illustrating an idealized pulsating auroral region, the flow field has only large-scale spatial variation, but an overall 0.3 Hz temporal variation. To make best use of the ARCS CubeSwarm for such an event, one would instead take sub-second or faster data collection frames, and allow large (S/C to S/C in two dimensions) spatial interpolation. While this is not our focus, it illustrates the flexibility of the ARCS data collection scheme, and the high dimensionality of what is meant by "what is ARCS's resolution".

For our ARCS mission, in §D.4 through §D.6, we have described the scales and diversity of structures we aim to examine in order to close our science objectives. Table D-3 lists a summary chart relating the observational platform parameters (in time, space, and measurement) that are required for science closure, to the array definition justification.

Table D-3: Observational Baseline Array Definition Justification		
Array Parameter	**Requirement**	**Justification**
Latitudinal Span	400 km cross-arc width	covers substantial fraction of typical arc structures, Fig. D-11, Fig. D-5
Along-track space/ time disambiguation	at least 3 points along-track	18-sec cadence, sub km cross-arc resolution, Fig. D-23 top
Longitudinal Span	900 km including 300 km spacing of outer planes	based on the need to observe context of WTS and streamer-like structures in the along-arc direction, Fig D-11, Fig. D-5
Along-track resolution	30 Hz sample rate for flows and mag	needed to resolve gradient scale lengths at edges of arcs, Fig. D-13
Across-track resolution	50 km inner orbit plane spacing	based on the need to resolve WTS and bead-like structures in the along-arc direction, Fig. D-11, Fig. D-5
Rapid time variation	30 Hz sample rate for flows and mag; high frame rate in GBO	Sub-second cadence, inter-spacecraft spatial resolution, Fig. D-20 bottom
Temporal context	Imagery before and after Scen3 crossings	Collect imagery over 10s of min time evolution of discrete arc structures of crossing, up to 10s of minutes
3d ionospheric volume	Volumetric electron density validation over in situ observation region	Density reconstructions Fig. D-12

L.27.1 Referenced Standards

ANSI/AIAA S-120A-2015(2019), Mass Properties Control for Space Systems. https://www.aiaa.org/docs/default-source/uploadedfiles/publications/standards/s-120a-sec-public-review-and-co-ballot-draft.pdf?sfvrsn=ac4256aa_0

ANSI/EIA-649, National Consensus Standard for CM, March 2015. https://www.dsp.dla.mil/Portals/26/Documents/Publications/Journal/150301-DSPJ-02.pdf

CANISTERIZED SATELLITE DISPENSER (CSD) DATA SHEET. Planetary Systems Corp. (2017, August 4). http://www.planetarysystemscorp.com/web/wp-content/uploads/2017/10/2002337E-CSD-Data-Sheet.pdf.

EEE-INST-002 (2003), https://nepp.nasa.gov/docuploads/FFB52B88-36AE-4378-A05B-2C084B5EE2CC/EEE-INST-002_add1.pdf

EHPD-RQMT-0001, Explorers & Heliophysics Projects Division (EHPD) Mission Assurance Requirements (MAR) Mission Risk Class - NPR7120.5 Class C, 2017. https://explorers.larc.nasa.gov/2019APSMEX/MO/pdf_files/EHPD-RQMT-0001-091416Released-1.pdf

FAR 19.7, The Small Business Subcontracting Program, March 10, 2021. https://www.acquisition.gov/far/subpart-19.7.

FAR 52.219-9, Small Business Subcontracting Plan, June 2020. https://www.acquisition.gov/far/52.219-9.

FIPS 140-2, Security Requirements for Crytographic Modules, May 25, 2001. https://csrc.nist.gov/publications/detail/fips/140/2/final.

GSFC-STD-7000A, General Environmental Verification Standards for GSFC Flight Programs and Projects, (2013). https://standards.nasa.gov/standard/gsfc/gsfc-std-7000

IPC standards for class-3/A printed wiring board assemblies. https://www.ipc.org/ipc-standards

International Reference Ionosphere (2021), http://irimodel.org/.

International Telecommunication Union, Recommendation ITU-R P.531-11 (2012) Ionospheric propagation data and prediction methods required for the design of satellite services and systems

IRI, (2021) https://ccmc.gsfc.nasa.gov/modelweb/ionos/iri.html, accessed May, 2021.

Mil-STD-461. http://everyspec.com/MIL-STD/MIL-STD-0300-0499/MIL-STD-461_8678/

NASA CARA (2020), "Best Practices", https://nodis3.gsfc.nasa.gov/OCE_docs/OCE_50.pdf; page 15. accessed 2021.

NASA EEE-INST-002, (April 2008). https://nepp.nasa.gov/index.cfm/12821.

NASA Strategic Plan 2018. (2018, February 12). https://www.nasa.gov/sites/default/files/atoms/files/nasa_2018_strategic_plan.pdf.

NASA. (2018) Science Mission Directorate Policy Citizen Science SMD Policy Document SPD-33 Recommended by SMD Science Management Council Approved by SMD Associate Administrator Responsible SMD Official: Direction, Science Engagement and Partnerships[Online]. Available at: https://science.nasa.gov/citizenscientists

NASA-STD-1006 Space Systems Protection, October 29, 2019. https://standards.nasa.gov/standard/nasa/nasa-std-1006-wchange-1.

NASA-STD-6016 Technical Standards System (May 14, 2020). https://standards.nasa.gov/stan-

dard/nasa/nasa-std-6016.

NASA-STD-8719.24 Technical Standards System (August 26, 2011). https://standards.nasa.gov/standard/nasa/nasa-std-871924

NASA 8739 Workmanship Standards. https://nepp.nasa.gov/index.cfm/5511

NASA. (2016, June 30). GSFC-STD-1000. Rules for the Design, Development, Verification, and Operation of Flight Systems. https://standards.nasa.gov/standard/gsfc/gsfc-std-1000.

NID 1058.127, NASA Enterprise Protection Program, May 7, 2020. https://nodis3.gsfc.nasa.gov/OPD_docs/NID_1058_127.pdf

NPD 8700.1E, NASA Policy for Safety and Mission Success, (December6, 2013). https://nodis3.gsfc.nasa.gov/displayDir.cfm?Internal_ID=N_PD_8700_001E_&page_name=main

NPR 1058.1 section 2.3, Officials-in-Charge of Headquarters Offices, Mission Directorate Associate Administrators, Center Directors, Program Directors, Program Managers, and Project Managers, June 14, 2019.

NPR 2810.1, Security of Information Technology, (May 19, 2011). https://nodis3.gsfc.nasa.gov/displayDir.cfm?Internal_ID=N_PR_2810_001A_&page_name=main

NPR 7120.5, NASA Space Flight Program and Project Management Requirements, (August 14, 2012). https://nodis3.gsfc.nasa.gov/displayDir.cfm?t=NPR&c=7120&s=5E

NPR 7123.1C, NASA Systems Engineering Processes and Requirements, (February, 14, 2020). https://nodis3.gsfc.nasa.gov/displayDir.cfm?t=NPR&c=7123&s=1B

NPR 7150.2C, NASA Software Engineering Requirements, (2019). https://nodis3.gsfc.nasa.gov/displayDir.cfm?t=NPR&c=7150&s=2B

NPR 8705.4, Risk Classfication for NASA Payloads, (June 14, 2004). https://nodis3.gsfc.nasa.gov/displayDir.cfm?Internal_ID=N_PR_8705_004A_&page_name=main

NPR 8705.5A, Technical Probabilistic Risk Assessment (PRA) Procedures for Safety and Mission Success for NASA Programs and Projects, (June 7, 2010). Technical Probabilistic Risk Assessment (PRA) Procedures for Safety and Mission Success for NASA Programs and Projects

NPR 8715.7, Payload Safety Program, (April 27, 2020). https://nodis3.gsfc.nasa.gov/displayDir.cfm?Internal_ID=N_PR_8715_007B_&page_name=main

NRC, (2013), National Research Council (2013), Solar and Space Physics: A Science for a Technological Society. Washington, DC: The National Academies Press. https://doi.org/10.17226/13060.

Science Mission Directorate Policy Citizen Science SMD Policy Document SPD-33 Recommended by SMD Science Management Council Approved by SMD Associate Administrator Responsible SMD Official: Director, Science Engagement and Partnerships. (2018). Retrieved from https://science.nasa.gov/citizenscientists

L.27.2 Documents and Papers

Aakjær, C.D., Olsen, N. and Finlay, C.C., 2016. Determining polar ionospheric electrojet currents from Swarm satellite constellation magnetic data. Earth, Planets and Space, 68(1), p.140. doi: 10.1186/s40623-016-0509-y.

AIM-1, in National Research Council (2013), Solar and Space Physics: A Science for a Technological Society. Washington, DC: The National Academies Press. https://doi.org/10.17226/13060.

Alken, P., Thébault, E., Beggan, C.D. et al. International Geomagnetic Reference Field: the thirteenth generation. Earth Planets Space 73, 49 (2021). https://doi.org/10.1186/s40623-020-

01288-x

Amm, O., 2001. The elementary current method for calculating ionospheric current systems from multisatellite and ground magnetometer data. Journal of Geophysical Research: Space Physics, 106(A11), pp.24843-24855. doi: 10.1029/2001JA900021.

Amm, O., et al., Ann. Geophys., 29, 701–716, 2011.

Amm, O., Pajunpää, A., and Brandström, U., 1999, Spatial distribution of conductances and currents associated with a north-south auroral form during a multiple-substorm period, Ann. Geophys., 17, 1385–1396, https://doi.org/10.1007/s00585-999-1385-6.

Anderson, B. J., R. Angappan, A. Barik, S. K. Vines, S. Stanley, P. N. Bernasconi, H. Korth, and R. J. Barnes (2020), Satellite Constellation Data for Study of Earth's Magnetic Field, in press, Geochemistry, Geophysics, Geosystems (G3), 8 June 2021.

Anderson, B.J., Acuña, M.H., Lohr, D.A., Scheifele, J., Raval, A., Korth, H. and Slavin, J.A., 2007. The Magnetometer instrument on MESSENGER. In The MESSENGER mission to Mercury (pp. 417-450). Springer, New York, NY. doi: 10.1007/978-0-387-77214-1_12.

Anderson, B.J., Gary, J.B., Potemra, T.A., Frahm, R.A., Sharber, J.R. and Winningham, J.D., 1998. UARS observations of Birkeland currents and Joule heating rates for the November 4, 1993, storm. Journal of Geophysical Research: Space Physics, 103(A11), pp.26323-26335. doi: 10.1029/98JA01236.

Anderson, B.J., Korth, H., Waters, C.L., Green, D.L., Merkin, V.G., Barnes, R.J. and Dyrud, L.P., 2014. Development of large-scale Birkeland currents determined from the Active Magnetosphere and Planetary Electrodynamics Response Experiment. Geophysical Research Letters, 41(9), pp.3017-3025. doi: 10.1002/2014GL059941.

Anderson, B.J., Potemra, T.A., Bythrow, P.F., Zanetti, L.J., Holland, D.B. and Winningham, J.D., 1993. Auroral currents during the magnetic storm of November 8 and 9, 1991: Observations from the Upper Atmosphere Research Satellite particle environment monitor. Geophysical research letters, 20(12), pp.1327-1330. doi: 10.1029/93GL01106.

Anderson, B.J., Takahashi, K. and Toth, B.A., 2000. Sensing global Birkeland currents with Iridium® engineering magnetometer data. Geophysical Research Letters, 27(24), pp.4045-4048. doi: 10.1029/2000GL000094.

Anderson, B.J., Zanetti, L.J., Lohr, D.H., Hayes, J.R., Acuña, M.H., Russell, C.T. and Mulligan, T., 2001. In-flight calibration of the NEAR magnetometer. IEEE transactions on geoscience and remote sensing, 39(5), pp.907-917. doi: 10.1109/36.921408.

Anderson, C., Davies, T., Conde, M., Dyson, P., & Kosch, M. J. (2011). Spatial sampling of the thermospheric vertical wind field at auroral latitudes. Journal of Geophysical Research: Space Physics, 116(A6).

Angelopoulos et al., 2008, First Results from the THEMIS Mission, Space Sci Rev, 141: 453–476 DOI 10.1007/s11214-008-9378-4

Archer, W. E., Knudsen, D. J., Burchill, J. K., Jackel, B., Donovan, E., Connors, M., and Juusola, L., 2017. Birkeland current boundary flows, J. Geophys. Res. Space Physics, 122, 4617– 4627, doi:10.1002/2016JA023789.

Archer, W. E., Knudsen, D. J., Burchill, J. K., Patrick, M. R. and St.-Maurice, J. P. 2015. Anisotropic core ion temperatures associated with strong zonal flows and upflows. Geophys. Res. Lett., 42: 981– 986. doi: 10.1002/2014GL062695.

Archer, W., D.J. Knudsen, 2018. Distinguishing subauroral ion drifts from Birkeland current boundary flows: SAID vs BCBF. Journal of Geophysical Research: Space Physics 123. doi: 10.1002/2017JA024577.

Archer, W.E., Gallardo-Lacourt, B., Perry, G., St.-Maurice, J.P., Buchert, S.C. and Donovan, E., 2019. Steve: The Optical Signature of Intense Subauroral Ion Drifts. Geophysical Research Letters. doi: 10.1029/2019GL082687.

Auroral Imaging Group, University of Calgary., (2019) swarm-aurora.com[Online]. Available at: https://swarm-aurora.com.

Austen, J.R., Franke, S.J. and Liu, C.H., 1988. Ionospheric imaging using computerized tomography. Radio Science, 23(3), pp.299-307. doi: 10.1029/RS023i003p00299.

Averkin, S. N. and N. A.Gatsonis, A parallel electrostatic Particle-in-Cell method on unstructured tetrahedral grids for large-scale bounded collisionless plasma simulations, Journal of Computational Physics, Volume 363, 15 June 2018, Pages 178-199, https://doi.org/10.1016/j.jcp.2018.02.011

Baker, D.N., Riesberg, L., Pankratz, C.K., Panneton, R.S., Giles, B.L., Wilder, F.D. and Ergun, R.E., 2016. Magnetospheric multiscale instrument suite operations and data system. Space Science Reviews, 199(1-4), pp.545-575. doi: 10.1007/s11214-014-0128-5.

Basu, S. K.M. Groves, Su. Basu, P.J. Sultan, Specification and forecasting of scintillations in communication/navigation links: current status and future plans, Journal of Atmospheric and Solar-Terrestrial Physics, Volume 64, Issue 16, 2002, Pages 1745-1754, ISSN 1364-6826,https://doi.org/10.1016/S1364-6826(02)00124-4.

Basu, S., MacKenzie, E., and Basu, S. (1988), Ionospheric constraints on VHF/UHF communications links during solar maximum and minimum periods, Radio Sci., 23(3), 363– 378, doi:10.1029/RS023i003p00363.

Bekkeng, T.A., Helgeby, E.S., Pedersen, A., Trondsen, E., Lindem, T. and Moen, J.I., 2019. Multi-needle Langmuir probe system for electron density measurements and active spacecraft potential control on cubesats. IEEE Transactions on Aerospace and Electronic Systems. doi: 10.1109/TAES.2019.2900132.

Bernhardt, P.A. and Siefring, C.L., 2006. New satellite-based systems for ionospheric tomography and scintillation region imaging. Radio science, 41(5). doi: 10.1029/2005RS003360.

Bernhardt, P.A. and Siefring, C.L., 2010. Low-latitude ionospheric scintillations and total electron content obtained with the CITRIS instrument on STPSat1 using radio transmissions from DORIS ground beacons. Advances in Space Research, 45(12), pp.1535-1540. doi: 10.1016/j.asr.2009.12.001.

Bernhardt, P.A., McCoy, R.P., Dymond, K.F., Picone, J.M., Meier, R.R., Kamalabadi, F., Cotton, D.M., Charkrabarti, S., Cook, T.A., Vickers, J.S. and Stephan, A.W., 1998. Two-dimensional mapping of the plasma density in the upper atmosphere with computerized ionospheric tomography (CIT). Physics of Plasmas, 5(5), pp.2010-2021. doi: 10.1063/1.872872.

Bernhardt, P.A., Selcher, C.A., Basu, S., Bust, G. and Reising, S.C., 2000. Atmospheric studies with the Tri-Band Beacon instrument on the COSMIC constellation. TERRESTRIAL ATMOSPHERIC AND OCEANIC SCIENCES, 11(1), pp.291-312.

Bernhardt, P.A., Siefring, C.L., Galysh, I.J. and Koch, D.E., 2008. The Scintillation and Tomography Receiver in Space (CITRIS) Instrument for Ionospheric Research. NAVAL RESEARCH LAB WASHINGTON DC PLASMA PHYSICS DIV.

Bernhardt, P.A., Siefring, C.L., Galysh, I.J., Rodilosso, T.F., Koch, D.E., MacDonald, T.L., Wilkens, M.R. and Landis, G.P., 2006. Ionospheric applications of the scintillation and tomography receiver in space (CITRIS) mission when used with the DORIS radio beacon network. Journal of Geodesy, 80(8-11), pp.473-485. doi: 10.1007/s00190-006-0064-6.

Bland, E. C., Heino, E., Kosch, M. J., and Partamies, N.: SuperDARN Radar-Derived HF Radio Attenuation During the September 2017 Solar Proton Events, Space Weather, 16, 1455–1469,

https://doi.org/10.1029/2018SW001916, 2018.

Blewitt, G., 1990. An automatic editing algorithm for GPS data. Geophysical research letters, 17(3), pp.199-202. doi: 10.1029/GL017i003p00199.

Board, S.S. and National Research Council, 2013. Solar and space physics: A science for a technological society. National Academies Press. doi: 10.17226/13060.

Borovsky, J.E., 1998. Aurorae: Still in the dark. Nature, 393(6683), p.312. doi: 10.1038/30616.

Borovsky, J.E., Birn, J., Echim, M.M., Fujita, S., Lysak, R.L., Knudsen, D.J., Marghitu, O., Otto, A., Watanabe, T.H. and Tanaka, T., 2020. Quiescent discrete auroral arcs: A review of magnetospheric generator mechanisms. Space Science Reviews, 216(1), pp.1-39.

Bortnik, J., W. Li, R. M. Thorne, and V. Angelopoulos (2016), A unified approach to inner magnetospheric state prediction, J. Geophys. Res. Space Phys., 120, doi: 10.1002/2015JA021733.

Bortnik, J., X. Chu, Q. Ma, W. Li, X. Zhang, R. M. Thorne, V. Angelopoulos, R. E. Denton, C. A. Kletzing, G. B. Hospodarsky, H. E. Spence, G. D. Reeves, S. G. Kanekal, and D. N. Baker (2018), Artificial Neural Networks for Determining Magnetospheric Conditions, in Machine Learning Techniques for Space Weather, Elsevier Inc., doi: 10.1016/B978-0-12-811788-0.00011-1.

Brambles, O.J., Lotko, W., Zhang, B., Wiltberger, M., Lyon, J. and Strangeway, R.J., 2011. Magnetosphere sawtooth oscillations induced by ionospheric outflow. Science, 332(6034), pp.1183-1186. doi: 10.1126/science.1202869.

Brekke, A., Hall, C. and Hansen, T.L., 1989, June. Auroral ionospheric conductances during disturbed conditions. In Annales Geophysicae (Vol. 7, pp. 269-280).

Briggs, B.H., 1975. Ionospheric irregularities and radio scintillations. Contemporary Physics, 16(5), pp.469-488. doi: 10.1080/00107517508210825.

Brittnacher, M., Spann, J., Parks, G. and Germany, G., 1997. Auroral observations by the polar ultraviolet imager (UVI). Advances in Space Research, 20(4-5), pp.1037-1042. doi: 10.1016/S0273-1177(97)00558-9.

Bunch, N.L., J. LaBelle, A.T. Weatherwax, J.M. Hughes, Auroral Medium Frequency Burst radio emission associated with the March 23, 2007, THEMIS study substorm, J. Geophys. Res., 113, A00C08, doi:10.1029/2008JA013503, 2008.

Burch, J.L., 2000. IMAGE mission overview. In The Image Mission (pp. 1-14). Springer, Dordrecht. doi: 10.1007/978-94-011-4233-5_1.

Burch, J.L., Torbert, R.B., Phan, T.D., Chen, L.J., Moore, T.E., Ergun, R.E., Eastwood, J.P., Gershman, D.J., Cassak, P.A., Argall, M.R. and Wang, S., 2016. Electron-scale measurements of magnetic reconnection in space. Science, 352(6290), p.aaf2939. doi: 10.1126/science.aaf2939.

Burke, W. J., Huang, C. Y., Valladares, C. E., Machuzak, J. S., Gentile, L. C., & Sultan, P. J. (2003). Multipoint observations of equatorial plasma bubbles. Journal of Geophysical Research: Space Physics, 108(A5).

Burnett, A., and J. LaBelle, Estimating polar cap density and medium-frequency burst source heights using 2fce-roar radio emissions, J. Geophys. Res., 125, doi:10.1029/2020JA028166, 2020.

Camporeale, E., X. Chu, O. V. Agapitov, and J. Bortnik (2019), On the generation of probabilistic forecasts from deterministic models, Space Weather, doi: 10.1029/2018SW002026.

Carlson, C.W., Curtis, D.W., Paschmann, G. and Michel, W., 1982. An instrument for rapidly measuring plasma distribution functions with high resolution. Advances in Space Research, 2(7), pp.67-70. doi: 10.1016/0273-1177(82)90151-X.

Carlson, C.W., Pfaff, R.A. and Watzin, J.G., 1998a. The fast auroral snapshot (FAST) mission. Geophysical research letters, 25(12), pp.2013-2016. doi: 10.1029/98GL01592.

Carlson, C.W., McFadden, J.P., Ergun, R.E., Temerin, M., Peria, W., Mozer, F.S., Klumpar, D.M., Shelley, E.G., Peterson, W.K., Moebius, E. and Elphic, R., 1998b. FAST observations in the downward auroral current region: Energetic upgoing electron beams, parallel potential drops, and ion heating. Geophysical Research Letters, 25(12), pp.2017-2020. doi: 10.1029/98GL00851.

Carlson, C.W., McFadden, J.P., Turin, P., Curtis, D.W. and Magoncelli, A., 2001. The electron and ion plasma experiment for FAST. In The FAST Mission (pp. 33-66). Springer, Dordrecht. doi: 10.1007/978-94-010-0332-2_2.

Case, N., MacDonald, E. and Patel, K., 2015a. Aurorasaurus and the St Patrick's Day storm. Astronomy and Geophysics, 56(3), pp.3-13. doi: 10.1093/astrogeo/atv089.

Case, N.A., MacDonald, E.A., Heavner, M., Tapia, A.H. and Lalone, N., 2015b. Mapping auroral activity with Twitter. Geophysical Research Letters, 42(10), pp.3668-3676. doi: 10.1002/2015GL063709.

Case, N.A., Kingman, D. and MacDonald, E.A., 2016a. A real-time hybrid aurora alert system: Combining citizen science reports with an auroral oval model. Earth and Space Science, 3(6), pp.257-265. doi: 10.1002/2016EA000167.

Case, N.A., MacDonald, E.A. and Viereck, R., 2016b. Using citizen science reports to define the equatorial extent of auroral visibility. Space Weather, 14(3), pp.198-209. doi: 10.1002/2015SW001320.

Cavalier, D. and Kennedy, E.B. eds., 2016. The rightful place of science: Citizen science. Consortium for Science, Policy & Outcomes.

Chu, X., et al. (2017a), A neural network model of three-dimensional dynamic electron density in the inner magnetosphere, J. Geophys. Res. Space Physics, 122, 9183–9197, doi: 10.1002/2017JA024464.

Chu, X. N., J. Bortnik, W. Li, Q. Ma, V. Angelopoulos, and R. M. Thorne (2017b), Erosion and refilling of the plasmasphere during a geomagnetic storm modeled by a neural network, Journal of Geophysical Research: Space Physics, Volume 122, issue 7, pp. 7118-7129, doi: 10.1002/2017JA023948.

Clayton, R., Burleigh, M., Lynch, K.A., Zettergren, M., Conde, M., Evans, T., Grubbs, G., Hampton, D.L., Hysell, D., Lessand, M., Michell, R., Reimer, A., Roberts, T.M., Samara, M., Varney, R., 2021. 3D modeling results of the GEMINI models using reconstructed 2D maps of auroral data. In preparation for submission to Journal of Geophysical Research: Space Physics.

Clayton, R., Lynch, K. A., Evans, T., Hampton, D. L., Burleigh, M., Zettergren, M. D.,et al. (2017). ISINGLASS Auroral Sounding Rocket Campaign Data Synthesis: Radar, Imagery, and In Situ Observations. In AGU Fall Meeting Abstracts (Vol. 2017, pp. SM41A-2664).

Clayton, R., Lynch, K., Zettergren, M., Burleigh, M., Conde, M., Grubbs, G., Hampton, D., Hysell, D., Lessard, M., Michell, R. and Reimer, A., 2019. Two-Dimensional Maps of In Situ Ionospheric Plasma Flow Data Near Auroral Arcs Using Auroral Imagery. Journal of Geophysical Research: Space Physics, 124(4), pp.3036-3056. doi: 10.1029/2018JA026440.

Codrescu, M.V., Fuller-Rowell, T.J. and Foster, J.C., 1995. On the importance of E-field variability for Joule heating in the high-latitude thermosphere. Geophysical Research Letters, 22(17), pp.2393-2396. doi: 10.1029/95GL01909.

Codrescu, M.V., Fuller-Rowell, T.J., Foster, J.C., Holt, J.M. and Cariglia, S.J., 2000. Electric field variability associated with the Millstone Hill electric field model. Journal of Geophysical Research: Space Physics, 105(A3), pp.5265-5273. doi: 10.1029/1999JA900463.

Cohen, I.J., Lessard, M.R., Kaeppler, S.R., Bounds, S.R., Kletzing, C.A., Streltsov, A.V., LaBelle, J.W., Dombrowski, M.P., Jones, S.L., Pfaff, R.F. and Rowland, D.E., 2013. Auroral Current and Electrodynamics Structure (ACES) observations of ionospheric feedback in the Alfvén resonator and model responses. Journal of Geophysical Research: Space Physics, 118(6), pp.3288-3296. doi: 10.1002/jgra.50348.

Conde, M.G., Bristow, W.A., Hampton, D.L. and Elliott, J., 2018. Multiinstrument Studies of Thermospheric Weather Above Alaska. Journal of Geophysical Research: Space Physics, 123(11), pp.9836-9861. doi: 10.1029/2018JA025806.

Cooper, C., 2016. Citizen science: How ordinary people are changing the face of discovery. Abrams.

Coster, A.J., Erickson, P. J., Lanzerotti, Lou, eds., Space Weather Effects and Applications, Wiley. (2021). DOI: https://doi.org/10.1002/9781119815570

Coster, Anthea, Skone, Susan, Mitchell, Cathryn, De Franceschi, Giorgiana, Alfonso, Lucilla, Romano, Vincenzo, "Global Studies of GPS Scintillation," Proceedings of the 2005 National Technical Meeting of The Institute of Navigation, San Diego, CA, January 2005, pp. 1130-1139.

Coxon, J. C., Milan, S. E., & Anderson, B. J. (2018). A review of Birkeland current research using AMPERE. Electric currents in geospace and beyond, 257-278.

Craven P. and Wahba G., Smoothing noisy data with spline functions: Estimating the correct degree of smoothing by the method of generalized cross-validation, Numerische Mathematik volume31, pages 377–403 (1978).

Craven, J. D., Frank, L. A., and Akasofu, S.-I. (1989), Propagation of a westward traveling surge and the development of persistent auroral features, J. Geophys. Res., 94(A6), 6961– 6967, doi:10.1029/JA094iA06p06961.

Darkjamn (2021), https://darkjamn.blogspot.com/2015/12/dark-wallpaper-earth.html, accessed May 2021.

Datta-Barua, S., Su, Y., Deshpande, K., Miladinovich, D., Bust, G.S., Hampton, D. and Crowley, G., 2015. First light from a kilometer-baseline Scintillation Auroral GPS Array. Geophysical research letters, 42(10), pp.3639-3646. doi: 10.1002/2015GL063556.

Delamere, P.A., Otto, A., Ma, X., Bagenal, F. and Wilson, R.J., 2015. Magnetic flux circulation in the rotationally driven giant magnetospheres. Journal of Geophysical Research: Space Physics, 120(6), pp.4229-4245. doi: 10.1002/2015JA021036.

Delaney, A.H. and Bresler, Y., 1998. Globally convergent edge-preserving regularized reconstruction: an application to limited-angle tomography. IEEE Transactions on Image Processing, 7(2), pp.204-221. doi: 10.1109/83.660997

Deng, Y., Maute, A., Richmond, A.D. and Roble, R.G., 2009. Impact of electric field variability on Joule heating and thermospheric temperature and density. Geophysical Research Letters, 36(8). doi: 10.1029/2008GL036916.

Deshpande, K.B. and Zettergren, M.D., 2019. Satellite-Beacon Ionospheric-Scintillation Global Model of the Upper Atmosphere (SIGMA) III: Scintillation Simulation Using A Physics-Based Plasma Model. Geophysical Research Letters, 46(9), pp.4564-4572. doi: 10.1029/2019GL082576.

Deshpande, K.B., Bust, G.S., Clauer, C.R., Rino, C.L. and Carrano, C.S., 2014. Satellite-beacon Ionospheric-scintillation Global Model of the upper Atmosphere (SIGMA) I: High-latitude sensitivity study of the model parameters. Journal of Geophysical Research: Space Physics, 119(5), pp.4026-4043. doi: 10.1029/2019GL082576.

Deshpande, K.B., Bust, G.S., Clauer, C.R., Scales, W.A., Frissell, N.A., Ruohoniemi, J.M., Spogli, L., Mitchell, C. and Weatherwax, A.T., 2016. Satellite-beacon Ionospheric-scintillation Global Model of the upper Atmosphere (SIGMA) II: Inverse modeling with high-latitude observations to deduce irregularity physics. Journal of Geophysical Research: Space Physics, 121(9), pp.9188-9203. doi: 10.1002/2016JA022943.

Dettmering, D., Limberger, M. and Schmidt, M., 2014, May. Using DORIS for modeling the Vertical Total Electron Content of the Earth's Ionosphere. In EGU General Assembly Conference Abstracts (Vol. 16). doi: 10.1007/s00190-014-0748-2

Devereux, W.S., Asher, M.S., Heins, R.J., Chacos, A.A., Kusterer, T.L. and Linstrom, L.A., 2003. TIMED GPS navigation system (GNS): design, implementation, and performance assessment. Johns Hopkins APL technical digest, 24(2), p.179.

Documentary: Chasing Steve (2019), Prod. Leah Mallen and J. Fraser, All-In Productions.

Doe, R.A., Mendillo, M., Vickrey, J.F., Zanetti, L.J. and Eastes, R.W., 1993. Observations of nightside auroral cavities. Journal of Geophysical Research: Space Physics, 98(A1), pp.293-310. doi: 10.1029/92JA02004.

Doe, R.A., Vickrey, J.F. and Mendillo, M., 1995. Electrodynamic model for the formation of auroral ionospheric cavities. Journal of Geophysical Research: Space Physics, 100(A6), pp.9683-9696. doi: 10.1029/95JA00001.

Donovan, E., Mende, S., Jackel, B., Frey, H., Syrjäsuo, M., Voronkov, I., Trondsen, T., Peticolas, L., Angelopoulos, V., Harris, S. and Greffen, M., 2006. The THEMIS all-sky imaging array— System design and initial results from the prototype imager. Journal of Atmospheric and Solar-Terrestrial Physics, 68(13), pp.1472-1487. doi: 10.1016/j.jastp.2005.03.027.

Dungey, J.W., 1961. Interplanetary magnetic field and the auroral zones. Physical Review Letters, 6(2), p.47. doi: 10.1103/PhysRevLett.6.47.

ECSA. (2015) Ten principles of citizen science [Online]. Available at: https://ecsa.citizen-science.net/documents.

EISCAT3d, (2019): https://www.eiscat.se/eiscat3d/, accessed 2019.

ESA, 2021, https://earth.esa.int/eogateway/instruments/vfm/description.

Evans, T, 2019. The Reconstruction of Auroral Zone Plasma Flow Fields and Associated Electric Fields Combining Ground-Based Observation and MultiPoint in Situ Measurements, Senior Honors Thesis, Dept of Physics and Astronomy, Dartmouth College.

Fernandes, P.A. and Lynch, K.A., 2016. Electrostatic analyzer measurements of ionospheric thermal ion populations. Journal of Geophysical Research: Space Physics, 121(7), pp.7316-7325. doi: 10.1002/2016JA022582.

Fernandes, P.A., Lynch, K.A., Zettergren, M., Hampton, D.L., Bekkeng, T.A., Cohen, I.J., Conde, M., Fisher, L.E., Horak, P., Lessard, M.R. and Miceli, R.J., 2016. Measuring the seeds of ion outflow: Auroral sounding rocket observations of low-altitude ion heating and circulation. Journal of Geophysical Research: Space Physics, 121(2), pp.1587-1607. doi: 10.1002/2015JA021536.

Finlay, C.C., Maus, S., Beggan, C.D., Bondar, T.N., Chambodut, A., Chernova, T.A., Chulliat, A., Golovkov, V.P., Hamilton, B., Hamoudi, M. and Holme, R., 2010. International geomagnetic reference field: the eleventh generation. Geophysical Journal International, 183(3), pp.1216-1230. doi: 10.1111/j.1365-246X.2010.04804.x.

Fisher, L.E., Lynch, K.A., Fernandes, P.A., Bekkeng, T.A., Moen, J., Zettergren, M., Miceli, R.J., Powell, S., Lessard, M.R. and Horak, P., 2016. Including sheath effects in the interpretation of planar retarding potential analyzer's low-energy ion data. Review of Scientific Instruments, 87(4), p.043504. doi: 10.1063/1.4944416.

Forget, B., J-C. Cerisier, A. Berthelier, and J-J. Berthelier. "Ionospheric closure of small-scale Birkeland currents." Journal of Geophysical Research: Space Physics 96, no. A2 (1991): 1843-1847.

Forsyth, C., Sergeev, V.A., Henderson, M.G. et al. Physical Processes of Meso-Scale, Dynamic Auroral Forms. Space Sci Rev 216, 46 (2020). https://doi.org/10.1007/s11214-020-00665-y

Fraunberger, Lynch, et al, "Auroral Ionospheric Plasma Flow Extraction using Subsonic Retarding Potential Analyzers", Rev Scientific Instr., 2020, DOI: 10.1063/1.5144498.

Fraunberger, M 2019. 'Fitting Auroral Sounding Rocket Data to Optimize Thermal Ion Sensors'. Undergraduate thesis. Dartmouth College, Hanover.

Frederick-Frost, K.M. and Lynch, K.A., 2007. Low energy stable plasma calibration facility. Review of Scientific Instruments, 78(7), p.075113. doi: 10.1063/1.2756996.

Frey, H.U., Mende, S.B., Carlson, C.W., Gérard, J.C., Hubert, B., Spann, J., Gladstone, R. and Immel, T.J., 2001. The electron and proton aurora as seen by IMAGE-FUV and FAST. Geophysical research letters, 28(6), pp.1135-1138. doi: 10.1029/2000GL012352.

Frissell, N.A., Joshua S. Vega, E. Markowitz, A.J. Gerrard, W.D. Engelke, P.J. Erickson, E.S. Miller, R.C. Luetzelschwab, and J. Bortnik, High-Frequency Communications Response to Solar Activity in September 2017 as Observed by Amateur Radio Networks, Space Weather, 10.1029/2018SW002008, 17, 1, (118-132), (2019).

Frissell, N.A., Katz, J.D., Gunning, S.W., Vega, J.S., Gerrard, A.J., Earle, G.D., Moses, M.L., West, M.L., Huba, J.D., Erickson, P.J. and Miller, E.S., 2018. Modeling amateur radio soundings of the ionospheric response to the 2017 Great American Eclipse. Geophysical Research Letters, 45(10), pp.4665-4674. doi: 10.1029/2018GL077324.

Frissell, N.A., Miller, E.S., Kaeppler, S.R., Ceglia, F., Pascoe, D., Sinanis, N., Smith, P., Williams, R. and Shovkoplyas, A., 2014. Ionospheric sounding using real-time amateur radio reporting networks. Space Weather, 12(12), pp.651-656. doi: 10.1002/2014SW001132.

Gallardo-Lacourt, B., Nishimura, Y., Donovan, E., Gillies, D. M., Perry, G. W., Archer, W. E., et al. (2018). A statistical analysis of STEVE. Journal of Geophysical Research: Space Physics, 123,9893– 9905. doi: 10.1029/2018JA025368.

Galvin, A.B., Kistler, L.M., Popecki, M.A., Farrugia, C.J., Simunac, K.D.C., Ellis, L., Möbius, E., Lee, M.A., Boehm, M., Carroll, J. and Crawshaw, A., 2008. The Plasma and Suprathermal Ion Composition (PLASTIC) investigation on the STEREO observatories. In The STEREO Mission (pp. 437-486). Springer, New York, NY. doi: 10.1007/s11214-007-9296-x.

Garbe, G.P., 1990. A study of ion acceleration at rocket altitudes and development and calibration of pitch angle imaging charged particle detectors.

Garner, T.W., Gaussiran, T.L., York, J.A., Munton, D.M., Slack, C.M. and Mahrous, A.M., 2009. Ionospheric tomography network of Egypt: A new receiver network in support of the International Heliophysical Year. Earth, Moon, and Planets, 104(1-4), pp.227-235.

Garrett, H.B., "Spacecraft charging, an update", IEEE Transactions on Plasma Science, DOI:10.1109/27.902229, January 2001.

Gayetsky, L.E. and Lynch, K.A., 2011. Note: Flowing ion population from a resonance cavity source. Review of Scientific Instruments, 82(4), p.046112. Doi: 10.1063/1.3584969.

GCC Team. (2013, April 11). GCC 4.7 Release Series. GCC 4.7 Release Series - GNU Project - Free Software Foundation (FSF). https://gcc.gnu.org/gcc-4.7/. GEMINI, (2021) (https://github.com/gemini3d/), accessed May, 2021.

Germany, G.A., Parks, G.K., Brittnacher, M., Cumnock, J., Lummerzheim, D., Spann, J.F., Chen, L., Richards, P.G. and Rich, F.J., 1997. Remote determination of auroral energy char-

acteristics during substorm activity. Geophysical research letters, 24(8), pp.995-998. doi: 10.1029/97GL00864.

Gillies, D. M., Knudsen, D., Spanswick, E., Donovan, E., Burchill, J., and Patrick, M. , 2015. Swarm observations of field-aligned currents associated with pulsating auroral patches, J. Geophys. Res. Space Physics, 120, 9484–9499, doi: 10.1002/2015JA021416.

Gillies, D.M., Knudsen, D.J., Donovan, E.F., Spanswick, E.L., Hansen, C., Keating, D. and Erion, S., 2014. A survey of quiet auroral arc orientation and the effects of the interplanetary magnetic field. Journal of Geophysical Research: Space Physics, 119(4), pp.2550-2562.

GITM, (2021) GitHub (https://github.com/aaronjridley/GITM), accessed May, 2021.

Gjerloev, J. W., S. Ohtani, T. Iijima, B. Anderson, J. Slavin, and G. Le (2011), Characteristics of the terrestrial field-aligned current system, Ann. Geophys., 29, 1713–1729, doi:10.5194/angeo-29-1713-2011.

Gkioulidou, M., Wang, C.-P., Lyons, L. R., and Wolf, R. A.(2009), Formation of the Harang reversal and its dependence on plasma sheet conditions: Rice convection model simulations, J. Geophys. Res., 114, A07204, doi: 10.1029/2008JA013955.

Gledhill, J.A., 1986. The effective recombination coefficient of electrons in the ionosphere between 50 and 150 km. Radio Science, 21(3), pp.399-408. doi: 10.1029/RS021i003p00399.

Gold, G.H., Van Loan, C.F. (1996) Matrix Computations. Chapter 10.

Gold, R.E., Solomon, S.C., McNutt Jr, R.L., Santo, A.G., Abshire, J.B., Acuña, M.H., Afzal, R.S., Anderson, B.J., Andrews, G.B., Bedini, P.D. and Cain, J., 2001. The MESSENGER mission to Mercury: scientific payload. Planetary and Space Science, 49(14-15), pp.1467-1479.

Grodent, D., 2015. A brief review of ultraviolet auroral emissions on giant planets. Space Science Reviews, 187(1-4), pp.23-50. doi: 10.1007/s11214-014-0052-8.

Grubbs, G., II, R. Michell, M. Samara, D. Hampton, and J.-M. Jahn., 2016. A synthesis of star calibration techniques for ground-based narrowband electron-multiplying charge-coupled device imagers used in Auroral Photometry. J. Geophys.Res. Space Physics, 121, (pp.5991–6002), doi:10.1002/2015JA022186.

Grubbs, G., Michell, R., Samara, M., Hampton, D., Hecht, J., Solomon, S. and Jahn, J.M., 2018a. A comparative study of spectral auroral intensity predictions from multiple electron transport models. Journal of Geophysical Research: Space Physics, 123(1), pp.993-1005. doi: 10.1002/2017JA025026.

Grubbs, G., Michell, R., Samara, M., Hampton, D. and Jahn, J.M., 2018b. Predicting electron population characteristics in 2-D using multispectral ground-based imaging. Geophysical Research Letters, 45(1), pp.15-20. doi: 10.1002/2017GL075873.

Haerendel, G., Buchert, S., La Hoz, C., Raaf, B., & Rieger, E. (1993). On the proper motion of auroral arcs. Journal of Geophysical Research: Space Physics, 98(A4), 6087-6099.

Hansen, A., Blanch, J., Walter, T. and Enge, P., 2000. Ionospheric correlation analysis for WAAS: quiet and stormy. proceedings of ION GPS, Salt Lake City, UT.

Harrington, M, "RENU2 SOUNDING ROCKET ANALYSIS: ION DATABASE CONSTRUCTION", MS Thesis, Dartmouth College, Hanover NH, 2017

Haskins, C.B., Angert, M.P., Sheehi, E.J., Millard, W.P., Adams, N. and Hennawy, J.R., 2016, March. The Frontier software-defined radio for the solar probe plus mission. In 2016 IEEE Aerospace Conference (pp. 1-11). IEEE. doi: 10.1109/AERO.2016.7500770.

Heise, S., Jakowski, N., Wehrenpfennig, A., Reigber, C. and Lühr, H., 2002. Sounding of the topside ionosphere/plasmasphere based on GPS measurements from CHAMP: Initial results. Geophysical Research Letters, 29(14), pp.44-1. doi: 10.1029/2002GL014738.

Hernandez, E., E.A. Bering, A. Pessoa, M. Manriquez, N. Frissell, and J. LaBelle, HamSci Radio Research Using VLF and HF to measure aurora emissions and related phenomena, Abstract SA028-0004, presented at American Geophysical Union Fall Meeting (2020).

Huang, C.Y., Su, Y.J., Sutton, E.K., Weimer, D.R. and Davidson, R.L., 2014. Energy coupling during the August 2011 magnetic storm. Journal of Geophysical Research: Space Physics, 119(2), pp.1219-1232. doi: 10.1002/2013JA019297.

Huang, P. M. et al., "Different approaches to developing Small Satellite Missions," 31st Annual AIAA/USU Conference on Small Satellites, 2017.

Hughes, J., and J. LaBelle, The latitude dependence of auroral roar emissions, J. Geophys. Res., 103, 14910, 1998.

Iijima, T. and Potemra, T.A., 1976. The amplitude distribution of field-aligned currents at northern high latitudes observed by Triad. Journal of Geophysical Research, 81(13), pp.2165-2174. doi: 10.1029/JA081i013p02165.

Jia, X., Hansen, K. C., Gombosi, T. I., Kivelson, M. G., Tóth, G., DeZeeuw, D. L., and Ridley, A. J.(2012), Magnetospheric configuration and dynamics of Saturn's magnetosphere: A global MHD simulation, J. Geophys. Res., 117, A05225, doi:10.1029/2012JA017575.

Kaeppler, S.R., Hampton, D.L., Nicolls, M.J., Strømme, A., Solomon, S.C., Hecht, J.H. and Conde, M.G., 2015. An investigation comparing ground-based techniques that quantify auroral electron flux and conductance. Journal of Geophysical Research: Space Physics, 120(10), pp.9038-9056. doi: 10.1002/2015JA021396.

Kalmoni, N.M.E., Rae, I.J., Watt, C.E.J., Murphy, K.R., Samara, M., Michell, R.G., Grubbs, G. and Forsyth, C., 2018. A diagnosis of the plasma waves responsible for the explosive energy release of substorm onset. Nature communications, 9(1), p.4806. doi: 10.1038/s41467-018-07086-0.

Kamalabadi, F., Karl, W.C., Semeter, J.L., Cotton, D.M., Cook, T.A. and Chakrabarti, S., 1999. A statistical framework for space-based EUV ionospheric tomography. Radio Science, 34(2), pp.437-447. doi: 10.1029/1998RS900026.

Kaminski, A., Buquo, L., Roman, M.C., Beck, B. and Thaller, M., 2016. NASA's Public Participation Universe: Why and How the US Space Agency Is Democratizing Its Approaches to Innovation. In AIAA SPACE 2016 (p. 5466). doi: 10.2514/6.2016-5466.

Kan, J. R., & Akasofu, S. I. (1979). A model of the auroral electric field. Journal of Geophysical Research: Space Physics, 84(A2), 507-512.

Karl, W.C., 2005. Regularization in image restoration and reconstruction. In Handbook of Image and Video Processing(pp. 183-V). Academic Press.

Keiling, A., Wygant, J., Fillingim, M., & Trattner, K. J. (2020). Energetics and Alfvénic coupling of a poleward boundary intensification: A Polar case study. Journal of Geophysical Research: Space Physics, 125(8), e2020JA028041.

Kelley, M., 1989. The Earth's Ionosphere: Plasma Physics and Electrodynamics, Int. Geophys. Ser, 43, pp.437-455.

Kim, H., Lessard, M.R., Jones, S.L., Lynch, K.A., Fernandes, P.A., Aruliah, A.L., Engebretson, M.J., Moen, J.I., Oksavik, K., Yahnin, A.G. and Yeoman, T.K., 2017. Simultaneous observations of traveling convection vortices: Ionosphere-thermosphere coupling. Journal of Geophysical Research: Space Physics, 122(5), pp.4943-4959. doi: 10.1002/2017JA023904.

Kishk, A.A. and Huang, W., 2011. Size-reduction method for dielectric-resonator antennas. IEEE Antennas and Propagation Magazine, 53(2), pp.26-38. doi: 10.1109/MAP.2011.5949322.

Kivelson, M. G. and C.T. Russell, "Introduction to Space Physics", Cambridge University Press,

Knudsen, D. J., Burchill, J. K., Buchert, S. C., Eriksson, A. I., Gill, R., Wahlund, J.-E., Åhlen, L., Smith, M., and Moffat, B., 2017. Thermal ion imagers and Langmuir probes in the Swarm electric field instruments, J. Geophys. Res. Space Physics, 122, 2655– 2673, doi:10.1002/2016JA022571.

Knudsen, D.J., Donovan, E.F., Cogger, L.L., Jackel, B. and Shaw, W.D., 2001. Width and structure of mesoscale optical auroral arcs. Geophysical Research Letters, 28(4), pp.705-708. doi: 10.1029/2000GL011969.

Knudsen, D.J., Kelley, M.C. and Vickrey, J.F., 1992. Alfvén waves in the auroral ionosphere: A numerical model compared with measurements. Journal of Geophysical Research: Space Physics, 97(A1), pp.77-90. doi: 10.1029/91JA02300.

Knudsen, D.J., Kelley, M.C., Earle, G.D., Vickrey, J.F. and Boehm, M., 1990. Distinguishing Alfvén waves from quasi-static field structures associated with the discrete aurora: Sounding rocket and HILAT satellite measurements. Geophysical Research Letters, 17(7), pp.921-924. doi: 10.1029/GL017i007p00921.

Kosar, B.C., MacDonald, E.A., Case, N.A. and Heavner, M., 2018a. Aurorasaurus Database of Real-Time, Crowd-Sourced Aurora Data for Space Weather Research. Earth and Space Science, 5(12), pp.970-980. doi: 10.1029/2018EA000454.

Kosar, B.C., MacDonald, E.A., Case, N.A., Zhang, Y., Mitchell, E.J. and Viereck, R., 2018b. A case study comparing citizen science aurora data with global auroral boundaries derived from satellite imagery and empirical models. Journal of Atmospheric and Solar-Terrestrial Physics, 177, pp.274-282. doi: 10.1016/J.JASTP.2018.05.006.

Kovesi, P., 2015. Good colour maps: How to design them. arXiv preprint arXiv:1509.03700.

Kunitsyn, V.E. and Tereshchenko, E.D., 2003. Ionospheric tomography. Springer Science & Business Media.

Kunitsyn, V.E., Andreeva, E.S., Razinkov, O.G. and Tereshchenko, E.D. (1994), Phase and phase-difference ionospheric radio tomography. Int. J. Imaging Syst. Technol., 5: 128-140.

Kunitsyn, V.E., Andreeva, E.S., Tereshchenko, E.D., Khudukon, B.Z. and Nygren, T., 1994. Investigations of the ionosphere by satellite radiotomography. International Journal of Imaging Systems and Technology, 5(2), pp.112-127. doi: 10.1002/ima.1850050208.

LaBelle, J., An Explanation for the Fine Structure of MF Burst Emissions, Geophys. Res. Lett., 38, L03105, doi:10.1029/2010GL046218, 2011a.

LaBelle, J., Medium Frequency Burst Emissions: A terrestrial analog to Solar Type III bursts?, Planet. Radio Emissions VII, ed. by H.O. Rucker, et al., Austrian Acad. Sci. Press, p. 271--282, 2011b.

LaBelle, J., High-latitude radiowave propagation studies using a meridional chain of receivers, Ann. Geophys., 22, 1705--1718, 2004.

Lamarche, L. J., Varney, R. H., & Siefring, C. L. (2020). Analysis of Plasma Irregularities on a Range of Scintillation-Scales Using the Resolute Bay Incoherent Scatter Radars. Journal of Geophysical Research: Space Physics, 125(3), e2019JA027112.

Lee, J. K., Kamalabadi, F., and Makela, J. J. (2007), Localized three-dimensional ionospheric tomography with GPS ground receiver measurements, Radio Sci., 42, RS4018, doi:10.1029/2006RS003543.

Lee, J. K., Kamalabadi, F., and Makela, J. J. (2008), Three-dimensional tomography of ionospheric variability using a dense GPS receiver array, Radio Sci., 43, RS3001, doi:10.1029/2007RS003716.

Lessard, M, et al., 2019. "Overview of the Rocket Experiment for Neutral Upwelling Sounding Rocket 2 (RENU2), Geophys. Res. Lett., 46, https://doi.org/10.1029/2018GL081885

Liemohn, M. W. (2020). The case for improving the Robinson formulas. Journal of Geophysical Research: Space Physics, 125(10), e2020JA028332

Lohr, D.A., Zanetti, L.J., Anderson, B.J., Potemra, T.A., Hayes, J.R., Gold, R.E., Henshaw, R.M., Mobley, F.F., Holland, D.B., Acuña, M.H. and Scheifele, J.L., 1997. NEAR magnetic field investigation, instrumentation, spacecraft magnetics and data access. In The Near Earth Asteroid Rendezvous Mission (pp. 255-281). Springer, Dordrecht. doi: 10.1007/978-94-011-5200-6_6.

Lomidze, L., Burchill, J.K., Knudsen, D.J., Kouznetsov, A. and Weimer, D.R., 2019. Validity study of the Swarm horizontal cross-track ion drift velocities in the high-latitude ionosphere. Earth and Space Science, 6(3), pp.411-432. doi: 10.1029/2018EA000546.

Lotko, W., 2004. Inductive magnetosphere–ionosphere coupling. Journal of atmospheric and solar-terrestrial physics, 66(15-16), pp.1443-1456.

Loucks, D., Palo, S., Pilinski, M., Crowley, G., Azeem, I., and Hampton, D. (2017), High-latitude GPS phase scintillation from E region electron density gradients during the 20–21 December 2015 geomagnetic storm, J. Geophys. Res. Space Physics, 122, 7473–7490, doi:10.1002/2016JA023839.

Lu, G., Baker, D. N., McPherron, R. L., Farrugia, C. J., Lummerzheim, D., Ruohoniemi, J. M., et al. (1998). Global energy deposition during the January 1997 magnetic cloud event. Journal of Geophysical Research: Space Physics, 103(A6), 11685–11694. https://doi.org/10.1029/98JA00897

Lu, G., Richmond, A. D., Ruohoniemi, J. M., Greenwald, R. A., Hairston, M., Rich, F. J., & Evans, D. S. (2001). An investigation of the influence of data and model inputs on assimilative mapping of ionospheric electrodynamics. Journal of Geophysical Research: Space Physics, 106(A1), 417–433. https://doi.org/10.1029/2000JA000606

Lühr,H., J.Park, J.W.Gjerloev, J. Rauberg, I. Michaelis, J. M. G. Merayo, and P. Brauer (2015), Field-aligned currents' scale analysis performed with the Swarm constellation, Geophys. Res. Lett., 42,1–8, doi:10.1002/2014GL062453.

Lummerzheim, D. and Lilensten, J., 1994, November. Electron transport and energy degradation in the ionosphere: Evaluation of the numerical solution, comparison with laboratory experiments and auroral observations. In Annales Geophysicae (Vol. 12, No. 10, pp. 1039-1051).

Lynch, K.A., Hampton, D.L., Zettergren, M., Bekkeng, T.A., Conde, M., Fernandes, P.A., Horak, P., Lessard, M., Miceli, R., Michell, R. and Moen, J., 2015. MICA sounding rocket observations of conductivity-gradient-generated auroral ionospheric responses: Small-scale structure with large-scale drivers. Journal of Geophysical Research: Space Physics, 120(11), pp.9661-9682. doi: 10.1002/2014JA020860.

Lyon, J.G., Fedder, J.A. and Mobarry, C.M., 2004. The Lyon–Fedder–Mobarry (LFM) global MHD magnetospheric simulation code. Journal of Atmospheric and Solar-Terrestrial Physics, 66(15-16), pp.1333-1350. doi: 10.1016/j.jastp.2004.03.020.

Lyons, L.R., Nishimura, Y. and Zou, Y., 2016. Unsolved problems: Mesoscale polar cap flow channels' structure, propagation, and effects on space weather disturbances. Journal of Geophysical Research: Space Physics, 121(4), pp.3347-3352. doi: 10.1002/2016JA022437.

Lysak, R.L., 1991. Feedback instability of the ionospheric resonant cavity. Journal of Geophysical Research: Space Physics, 96(A2), pp.1553-1568. doi: 10.1029/90JA02154.

MacDonald, E.A., Case, N.A., Clayton, J.H., Hall, M.K., Heavner, M., Lalone, N., Patel, K.G. and Tapia, A., 2015. Aurorasaurus: A citizen science platform for viewing and reporting the aurora. Space Weather, 13(9), pp.548-559. doi: 10.1002/2015SW001214

MacDonald, Elizabeth A. (2018a) STEVE and the Citizen Scientists [Online]. Available at: https://www.americanscientist.org/article/steve-and-the-citizen-scientists. doi: 10.1511/2018.106.5.283.

MacDonald, E.A., Donovan, E., Nishimura, Y., Case, N.A., Gillies, D.M., Gallardo-Lacourt, B., Archer, W.E., Spanswick, E.L., Bourassa, N., Connors, M. and Heavner, M., 2018b. New science in plain sight: Citizen scientists lead to the discovery of optical structure in the upper atmosphere. Science advances, 4(3), p.eaaq0030. doi: 10.1126/sciadv.aaq0030

Magnes, W., Oberst, M., Valavanoglou, A., Hauer, H., Hagen, C., Jernej, I., Neubauer, H., Baumjohann, W., Pierce, D., Means, J. and Falkner, P., 2008. Highly integrated front-end electronics for spaceborne fluxgate sensors. Measurement Science and Technology, 19(11), p.115801. doi: 10.1088/0957-0233/19/11/115801.

Marghitu, O., 2012. Auroral arc electrodynamics: Review and outlook. Auroral Phenomenology and Magnetospheric Processes: Earth And Other Planets, 197, pp.143-158. doi:10.1029/2011GM001189.

Marholm, S., Marchand, R., Darian, D., Miloch, W.J. and Mortensen, M., 2019. Impact of Miniaturized Fixed-Bias Multineedle Langmuir Probes on CubeSats. IEEE Transactions on Plasma Science. doi: 10.1109/TPS.2019.2915810.

Markkanen, M., Lehtinen, M., Nygren, T., Pirttilä, J., Henelius, P., Vilenius, E., Tereshchenko, E.D. and Khudukon, B.Z., 1995. Bayesian approach to satellite radiotomography with applications in the Scandinavian sector. In Annales geophysicae (Vol. 13, No. 12, pp. 1277-1287). Copernicus.

Marklund, G. T., Karlsson, T., Blomberg, L. G., Lindqvist, P. A., Fälthammar, C. G., Johnson, M. L., ... & Zanetti, L. J. (1998). Observations of the electric field fine structure associated with the westward traveling surge and large-scale auroral spirals. Journal of Geophysical Research: Space Physics, 103(A3), 4125-4144.

Marsland, S. (2015), Machine learning: An Algorithmic Perspective, Second Edition, CRC Press, ISBN-13: 978-1-4665-8328-3

MATLAB answers: Reconstructing an image from projection data—MATLAB and Simulink Example [Online]. (2017). Available at: www.mathworks.com/matlabcentral/answers/370726-how-to-control-color-and-brightness-for-a-vector-map.

Maus, S., Manoj, C., Rauberg, J., Michaelis, I. and Lühr, H., 2010. NOAA/NGDC candidate models for the 11th generation International Geomagnetic Reference Field and the concurrent release of the 6th generation Pomme magnetic model. Earth, planets and space, 62(10), p.2. doi: 10.5047/eps.2010.07.006.

McPherron, R. L., El-Alaoui, M., Walker, R. J., Nishimura, Y., & Weygand, J. M. (2020). The relation of N-S auroral streamers to auroral expansion. Journal of Geophysical Research: Space Physics, 125(4), e2019JA027063.

Mende, S.B., Frey, H.U., Lampton, M., Gerard, J.C., Hubert, B., Fuselier, S., Spann, J., Gladstone, R. and Burch, J.L., 2001. Global observations of proton and electron auroras in a substorm. Geophysical research letters, 28(6), pp.1139-1142. doi: 10.1029/2000GL012340.

Mende, S.B., Harris, S.E., Frey, H.U., Angelopoulos, V., Russell, C.T., Donovan, E., Jackel, B., Greffen, M. and Peticolas, L.M., 2009. The THEMIS array of ground-based observatories for the study of auroral substorms. In The THEMIS Mission (pp. 357-387). Springer, New York, NY. doi: 10.1007/978-0-387-89820-9_16.

Merayo, J.M., Brauer, P., Primdahl, F., Petersen, J.R. and Nielsen, O.V., 2000. Scalar calibration of vector magnetometers. Measurement science and technology, 11(2), p.120.

Mercier, F., Cerri, L. and Berthias, J.P., 2010. Jason-2 DORIS phase measurement processing.

Advances in space research, 45(12), pp.1441-1454. doi: 10.1016/j.asr.2009.12.002.

Merkin, V.G. and Lyon, J.G., 2010. Effects of the low-latitude ionospheric boundary condition on the global magnetosphere. Journal of Geophysical Research: Space Physics, 115(A10). doi: 10.1029/2010JA015461.

Merkin, V.G., Anderson, B.J., Lyon, J.G., Korth, H., Wiltberger, M. and Motoba, T., 2013a. Global evolution of Birkeland currents on 10 min timescales: MHD simulations and observations. Journal of Geophysical Research: Space Physics, 118(8), pp.4977-4997. doi: 10.1002/jgra.50466.

Merkin, V.G., Lyon, J.G. and Claudepierre, S.G., 2013b. Kelvin-Helmholtz instability of the magnetospheric boundary in a three-dimensional global MHD simulation during northward IMF conditions. Journal of Geophysical Research: Space Physics, 118(9), pp.5478-5496. doi: 10.1002/jgra.50520.

Mitchell, C.N., Kersley, L., Heaton, J.A.T. and Pryse, S.E., 1997, June. Determination of the vertical electron-density profile in ionospheric tomography: experimental results. In Annales Geophysicae (Vol. 15, No. 6, pp. 747-752). Springer-Verlag. doi: 10.1007/s00585-997-0747-1.

Mittermaier, M. and Roberts, N., 2010. Intercomparison of spatial forecast verification methods: Identifying skillful spatial scales using the fractions skill score. Weather and Forecasting, 25(1), pp.343-354. doi: 10.1175/2009WAF2222260.1.

Moore, T.E., Chandler, M.O., Pollock, C.J., Reasoner, D.L., Arnoldy, R.L., Austin, B., Kintner, P.M. and Bonnell, J., 1996. Plasma heating and flow in an auroral arc. Journal of Geophysical Research: Space Physics, 101(A3), pp.5279-5297. doi: 10.1029/95JA03154.

Morioka, A., Y. Miyoshi, F. Tsuchiya, H. Misawa, K. Yumoto, G.K. Parks, R.R. Anderson, J.D. Menietti, and F. Honary (2009), Vertical evolution of auroral acceleration at substorm onset, {\it Ann. Geophys., 27}, 525–535.

Morioka, A., Y. Miyoshi, F. Tsuchiya, H. Misawa, T. Sakanoi, K. Yumoto, R.R. Anderson, J.D. Menietti, and E.F. Donovan (2007), Dual structure of auroral acceleration regions at substorm onsets as derived from AKR spectra, {\it J. Geophys. Res., 112}, A06245, doi:10.1029/2006JA012186.

Mrak, S., Semeter, J., Hirsch, M., Starr, G., Hampton, D., Varney, R.H., Reimer, A.S., Swoboda, J., Erickson, P.J., Lind, F. and Coster, A.J., 2018. Field-aligned GPS scintillation: Multisensor data fusion. Journal of Geophysical Research: Space Physics, 123(1), pp.974-992. doi: 10.1002/2017JA024557.

Nakamura, R., W. Baumjohann, R. Schoedel, V. A. Sergeev, M. Kubyshkina, M. Brittnacher, T. Mukai, K. Liou, 2001, Earthward flow bursts, auroral streamers and small expansions, J. Geophys. Res., 106, 10791-10802

Newell, P. T., and J. W. Gjerloev (2011), Evaluation of SuperMAG auroral electrojet indices as indicators of substorms and auroral power, J. Geophys. Res., 116, A12211, doi:10.1029/2011JA016779.

Newell, P.T., Meng, C.I. and Lyons, K.M., 1996. Suppression of discrete aurorae by sunlight. Nature, 381(6585), p.766. doi: 10.1038/381766a0.

Nikoukar, R., Kamalabadi, F., Kudeki, E., and Sulzer, M. 2012, On resolution/error trade-offs in incoherent scatter radar measurements, Radio Sci., 47, RS1008, doi:10.1029/2011RS004685.

Nikoukar, R., 2010. Near-optimal inversion of incoherent scatter radar measurements: coding schemes, processing techniques, and experiments (Doctoral dissertation, University of Illinois at Urbana-Champaign).

Nikoukar, R., Bust, G. and Murr, D., 2015. A novel data assimilation technique for the plasmasphere. Journal of Geophysical Research: Space Physics, 120(10), pp.8470-8485. doi: 10.1002/2015JA021455.

Nikoukar, R., Kamalabadi, F., Kudeki, E. and Sulzer, M., 2008. An efficient near-optimal approach to incoherent scatter radar parameter estimation. Radio Science, 43(05), pp.1-15. doi: 10.1029/2007RS003724.

Nishimura, Y., Gallardo-Lacourt, B., Zou, Y., Mishin, E., Knudsen, D.J., Donovan, E.F., Angelopoulos, V. and Raybell, R., 2019. Magnetospheric signatures of STEVE: Implication for the magnetospheric energy source and inter-hemispheric conjugacy. Geophysical Research Letters. doi: 10.1029/2019GL082460.

Nishimura, Y., Yang, J., Pritchett, P. L., Coroniti, F. V., Donovan, E. F., Lyons, L. R., ... & Mende, S. B. (2016). Statistical properties of substorm auroral onset beads/rays. Journal of Geophysical Research: Space Physics, 121(9), 8661-8676.

NOAA-SWPC, Solar Cycle 25 Forecast Update, https://www.swpc.noaa.gov/news/solar-cycle-25-forecast-update, downloaded May 2021

Nygrén, T., Markkanen, M., Lehtinen, M., Tereshchenko, E.D., Khudukon, B.Z., Evstafiev, O.V. and Pollari, P., 1997, February. Comparison of F-region electron density observations by satellite radio tomography and incoherent scatter methods. In Annales Geophysicae (Vol. 14, No. 12, pp. 1422-1428). Springer-Verlag. doi: 10.1007/s00585-996-1422-7.

O'Neill, M.B., Millard, W.P., Bubnash, B.M., Mitch, R.H. and Boye, J.A., 2016. Frontier Radio Lite: A Single-Board Software-Defined Radio for Demanding Small Satellite Missions, AIAA Small Satellite Conference SSC16-VII-2.

Otsuka, Y., Ogawa, T., Saito, A. et al. Earth Planet Sp (2002) 54: 63. https://doi.org/10.1186/BF03352422

Pedatella, N.M., Lu, G. and Richmond, A.D., 2018. Effects of high-latitude forcing uncertainty on the low-latitude and midlatitude ionosphere. Journal of Geophysical Research: Space Physics, 123(1), pp.862-882. doi: 10.1002/2017JA024683.

Peticolas, L.M., Hallinan, T.J., Stenbaek-Nielsen, H.C., Bonnell, J.W. and Carlson, C.W., 2002. A study of black aurora from aircraft-based optical observations and plasma measurements on FAST. Journal of Geophysical Research: Space Physics, 107(A8), pp.SMP-30. doi: 10.1029/2001JA900157.

Petosa, A. and Ittipiboon, A., 2010. Dielectric resonator antennas: A historical review and the current state of the art. IEEE antennas and Propagation Magazine, 52(5), pp.91-116. doi: 10.1109/MAP.2010.5687510.

Potemra, T.A., Zanetti, L.J. and Acuna, M.H., 1985. The AMPTE CCE magnetic field experiment. IEEE transactions on geoscience and remote sensing, (3), pp.246-249. doi: 10.1109/TGRS.1985.289521.

Raissi, Maziar, Paris Perdikaris, and George E. Karniadakis. "Physics-informed neural networks: A deep learning framework for solving forward and inverse problems involving nonlinear partial differential equations." Journal of Computational Physics 378 (2019): 686-707.

Raymund, T.D., Austen, J.R., Franke, S.J., Liu, C.H., Klobuchar, J.A. and Stalker, J., 1990. Application of computerized tomography to the investigation of ionospheric structures. Radio Science, 25(5), pp.771-789. doi: 10.1029/RS025i005p00771.

Rees, M.H. and Luckey, D., 1974. Auroral electron energy derived from ratio of spectroscopic emissions 1. Model computations. Journal of Geophysical Research, 79(34), pp.5181-5186. doi:10.1029/JA079i034p05181.

Rees, M.H. and Roble, R.G., 1986. Excitation of O (1 D) atoms in aurorae and emission of the [OI] 6300-Å line. Canadian journal of physics, 64(12), pp.1608-1613. doi: 10.1139/p86-284.

Reeves S. J. and Z. Zhe (1999), Sequential algorithms for observation selection, IEEE Trans. Sig-

nal Process., vol. 47, no. 1, pp. 123-132.

Richmond, A.D. and Kamide, Y., 1988. Mapping electrodynamic features of the high-latitude ionosphere from localized observations: Technique. Journal of Geophysical Research: Space Physics, 93(A6), pp.5741-5759. doi: 10.1029/JA093iA06p05741.

Richmond, A.D., 1992. Assimilative mapping of ionospheric electrodynamics. Advances in Space Research, 12(6), pp.59-68. doi: 10.1016/0273-1177(92)90040-5.

Richmond, A.D., 2010. On the ionospheric application of Poynting's theorem. Journal of Geophysical Research: Space Physics, 115(A10). doi: 10.1029/2010JA015768.

Richmond, A.D., Lu, G., Emery, B.A. and Knipp, D.J., 1998. The AMIE procedure: Prospects for space weather specification and prediction. Advances in Space Research, 22(1), pp.103-112. doi: 10.1016/S0273-1177(97)01108-3.

Ridley, A.J., Deng, Y. and Toth, G., 2006. The global ionosphere–thermosphere model. Journal of Atmospheric and Solar-Terrestrial Physics, 68(8), pp.839-864. doi: 10.1016/j.jastp.2006.01.008.

Robert, P., Dunlop, M. W., Roux, A., & Chanteur, G. (1998). Accuracy of current density determination. In G. Paschmann & P. W. Daly (Eds.), Analysis methods for multi-spacecraft data, ISSI scientific Reports Series (Vol. 1, pp. 395–418). Bern: Springer.

Roberts, N.M. and Lean, H.W., 2008. Scale-selective verification of rainfall accumulations from high-resolution forecasts of convective events. Monthly Weather Review, 136(1), pp.78-97. doi: 10.1175/2007MWR2123.1.

Roberts, T.M., Lynch, K.A., Clayton, R.E., Weiss, J. and Hampton, D.L., 2017. A small spacecraft for multipoint measurement of ionospheric plasma. Review of Scientific Instruments, 88(7), p.073507. doi: 10.1063/1.4992022.

Robinson, R. M., Vondrak, R. R., and Potemra, T. A. (1985), Auroral zone conductivities within the field-aligned current sheets, J. Geophys. Res., 90(A10), 9688– 9696, doi:10.1029/ JA090iA10p09688.

Robinson, R. M., Vondrak, R. R., Miller, K., Dabbs, T., & Hardy, D. (1987). On calculating ionospheric conductances from the flux and energy of precipitating electrons. Journal of Geophysical Research, 92(A3), 2565– 2569. https://doi.org/10.1029/JA092iA03p02565

Rogers, N.C., E.M. Warrington, and T.B. Jones, Large HF bearing errors for propagation paths tangential to the auroral oval, IEEE Proc. Microw. Antennas Propag., 144(4), 241-249, 1997.

Russell, C. T., B. J. Anderson, W. Baumjohann, K. R. Bromund, D. Dearborn, D. Fischer, G. Le, H. K. Leinweber, D. Leneman, W. Magnes, J. D. Means, M. B. Moldwin, R. Nakamura, D. Pierce, F. Plaschke, K. M. Ro, J. A. Slavin, R. J. Strangeway, R. Torbert, C. Hagen, I. Jernej, A. Valavanoglou, I. Richter (2014), The Magnetospheric Multiscale Magnetometers, Space Sci. Rev., doi:10.1007/s11214-014-0057-3.

Sarkango, Y., Jia, X., & Toth, G.(2019). Global MHD simulations of the response of Jupiter's magnetosphere and ionosphere to changes in the solar wind and IMF. Journal of Geophysical Research: Space Physics, 124, 5317– 5341. https://doi.org/10.1029/2019JA026787

Sarno-Smith, L. K., B. A. Larsen, R. M. Skoug, M. W. Liemohn, A. Breneman, J. R. Wygant, and M. F. Thomsen (2016), Spacecraft surface charging within geosynchronous orbit observed by the Van Allen Probes, Space Weather, 14, 151– 164, doi:10.1002/2015SW001345.

Sarrailh P. et al., "SPIS 5: New Modeling Capabilities and Methods for Scientific Missions," in IEEE Transactions on Plasma Science, vol. 43, no. 9, pp. 2789-2798, Sept. 2015, doi: 10.1109/ TPS.2015.2445384.

Schaubert, D.H., D. M. Pozar and A. Adrian, "Effect of microstrip antenna substrate thickness and permittivity: comparison of theories with experiment," in IEEE Transactions on Antennas and

Propagation, vol. 37, no. 6, pp. 677-682, June 1989, doi: 10.1109/8.29353.

Schunk, R.W. and Sojka, J.J., 1982. Ion temperature variations in the daytime high-latitude F region. Journal of Geophysical Research: Space Physics, 87(A7), pp.5169-5183. doi: 10.1029/ JA087iA07p05169.

Semeter, J., Mrak, S., Hirsch, M., Swoboda, J., Akbari, H., Starr, G.,… Pankratius, V. (2017). GPS signal corruption by the discrete Aurora: Precise measurements from the Mahali experiment. Geophysical Research Letters, 44, 9539– 9546. https://doi.org/10.1002/2017GL073570

Semeter, J., & Kamalabadi, F. (2005). Determination of primary electron spectra from incoherent scatter radar measurements of the auroral E region. Radio Science, 40(2), 1-17.

Semeter, J., Butler, T., Heinselman, C., Nicolls, M., Kelly, J. and Hampton, D., 2009. Volumetric imaging of the auroral ionosphere: Initial results from PFISR. Journal of Atmospheric and Solar-Terrestrial Physics, 71(6-7), pp.738-743. doi: 10.1016/j.jastp.2008.08.014.

Sergeev V, Sauvaud JA, Popescu D, Kovrazhkin R, Liou K, Newell P, Brittnacher M, Parks G, Nakamura R, Mukai T, Reeves G, 2000, Multiple-spacecraft observation of a narrow transient plasma jet in the earth's plasma sheet. Geophys Res Lett 27(6):851–854

Sharif B., and F. Kamalabadi (2008), Optimal Sensor Array Configuration in Remote Image Formation, in IEEE Transactions on Image Processing, vol. 17, no. 2, pp. 155-166, doi: 10.1109/ TIP.2007.914225

Sharif, B., and F. Kamalabadi (2005), Optimal discretization resolution in algebraic image reconstructions, in Bayesian Inference and Maximum Entropy Methods in Science and Engineering, edited by K. H. Knuth, A. E. Abbas, R. D. Morris, and J. P. Castle, Am. Inst. Phys. Conf. Proc., 803, 199–206.

Sharma, A. and R. Stilwell. "A low profile broadband UHF canted turnstile antenna phasing network." 2017 USNC-URSI Radio Science Meeting (Joint with AP-S Symposium) (2017): 117-118.

Shepherd, S.G., J. LaBelle, C.W. Carlson, and G. Rostoker, The latitudinal dynamics of auroral roar emissions, J. Geophys. Res., 104, 17217, 1999.

Shupe, M. D., , S. Y. Matrosov, , and T. Uttal, 2006: Arctic mixed-phase cloud properties derived from surface-based sensors at SHEBA. J. Atmos. Sci., 63, 697–711.

Siddiqui, M.U., Gayetsky, L.E., Mella, M.R., Lynch, K.A. and Lessard, M.R., 2011. A laboratory experiment to examine the effect of auroral beams on spacecraft charging in the ionosphere. Physics of Plasmas, 18(9), p.092905. doi: 10.1063/1.3640512.

Smith, A.M., Mitchell, C.N., Watson, R.J., Meggs, R.W., Kintner, P.M., Kauristie, K. and Honary, F., 2008. GPS scintillation in the high arctic associated with an auroral arc. Space Weather, 6(3). doi: 10.1029/2007SW000349.

Solomon, S.C., 2001. Auroral particle transport using Monte Carlo and hybrid methods. Journal of Geophysical Research: Space Physics, 106(A1), pp.107-116. doi: 10.1029/2000JA002011.

Solomon, S.C., 2017. Global modeling of thermospheric airglow in the far ultraviolet. Journal of Geophysical Research: Space Physics, 122(7), pp.7834-7848. doi: 10.1002/2017JA024314.

Sonnerup, B. U. Ö., & Scheible, M. (1998). Minimum and maximum variance analysis. In G. Paschmann, & P. W. Daly (Eds.), Analysis Methods forMulti-Spacecraft Data (no. SR-001 in ISSI Scientific Reports, chap. 8) (pp. 185–220). Noordwijk, Netherlands: ESA Publ. Div.

Stenbaek-Nielsen, H.C., Hallinan, T.J., Osborne, D.L., Kimball, J., Chaston, C., McFadden, J., Delory, G., Temerin, M. and Carlson, C.W., 1998. Aircraft observations conjugate to FAST: Auroral are thicknesses. Geophysical research letters, 25(12), pp.2073-2076. doi: 10.1029/98GL01058.

St-Maurice, J.P. and Schunk, R.W., 1979. Ion velocity distributions in the high-latitude ionosphere.

Reviews of Geophysics, 17(1), pp.99-134. doi: 10.1029/RG017i001p00099.

Streltsov, A.V. and Lotko, W., 2008. Coupling between density structures, electromagnetic waves and ionospheric feedback in the auroral zone. Journal of Geophysical Research: Space Physics, 113(A5). doi: 10.1029/2007JA012594.

Strickland, D.J., Meier, R.R., Hecht, J.H. and Christensen, A.B., 1989. Deducing composition and incident electron spectra from ground-based auroral optical measurements: Theory and model results. Journal of Geophysical Research: Space Physics, 94(A10), pp.13527-13539. doi:10.1029/JA094iA10p13527.

Sugiura, M., 1984. A fundamental magnetosphere-ionosphere coupling mode involving field-aligned currents as deduced from DE-2 observations. Geophysical research letters, 11(9), pp.877-880. doi: 10.1029/GL011i009p00877.

Sukur, M.I.A., Rahim, M.K.A. and Murad, N.A., 2013, September. Hybrid dielectric resonator with patch antenna at ultra-high frequency band. In 2013 IEEE International Conference on RFID-Technologies and Applications (RFID-TA) (pp. 1-4). IEEE. doi: 10.1109/RFID-TA.2013.6694535.

Sydorenko, D. and Rankin, R., 2013. Simulation of O+ upflows created by electron precipitation and Alfvén waves in the ionosphere. Journal of Geophysical Research: Space Physics, 118(9), pp.5562-5578. doi: 10.1002/jgra.50531.

Tavernier G, Fagard H, Feissel-Vernier M, Lemoine F, Noll C, Ries J, Soudarin L, Willis P (2005) The international DORIS service, Adv Space Res 36(3):333–341

Torbert, R.B., Burch, J.L., Phan, T.D., Hesse, M., Argall, M.R., Shuster, J., Ergun, R.E., Alm, L., Nakamura, R., Genestreti, K.J. and Gershman, D.J., 2018. Electron-scale dynamics of the diffusion region during symmetric magnetic reconnection in space. Science, 362(6421), pp.1391-1395. doi: 10.1126/science.aat2998.

Torbert, R.B., Vaith, H., Granoff, M., Widholm, M., Gaidos, J.A., Briggs, B.H., Dors, I.G., Chutter, M.W., Macri, J., Argall, M. and Bodet, D., 2016. The electron drift instrument for MMS. Space Science Reviews, 199(1-4), pp.283-305. doi: 10.1007/s11214-015-0182-7.

Torr, M.R., Torr, D.G., Zukic, M., Johnson, R.B., Ajello, J., Banks, P., Clark, K., Cole, K., Keffer, C., Parks, G. and Tsurutani, B., 1995. A far ultraviolet imager for the international solar-terrestrial physics mission. Space Science Reviews, 71(1-4), pp.329-383. doi: 10.1007/BF00751335.

TREx, (2019): https://www.ucalgary.ca/aurora/projects/trex, accessed 2019.

Troyer, R. N.,Jaynes, A. N.,Jones, S. L.,Knudsen, D. J., &Trondsen, T. S.(2021).The diffuse auroral eraser.Journal of Geophysical Research: Space Physics,126, e2020JA028805.https://doi.org/10.1029/2020JA028805

University of Calgary. Auroral Imaging Group, Projects [Online]. Available at: https://www.ucalgary.ca/aurora/projects.

University of Calgary. What is TREx? [Online]. Available at: http://aurora.phys.ucalgary.ca/public/trex/TREx_factsheet.png.

Vierinen, J., Norberg, J., Lehtinen, M. S., Amm, O., Roininen, L., Väänänen, A., Erickson, P. J., and McKay-Bukowski, D. (2014), Beacon satellite receiver for ionospheric tomography, Radio Sci., 49, 1141– 1152, doi: 10.1002/2014RS005434.

Vogel, C.R. and Oman, M.E., 1996. Iterative methods for total variation denoising. SIAM Journal on Scientific Computing, 17(1), pp.227-238. doi: 10.1137/0917016.

Vogel, C.R., 2002. Computational methods for inverse problems (Vol. 23). Siam.

Warrington, E.M., N.C. Rogers, and T.B. Jones, Large bearing errors for propagation paths contained within the polar cap, IEEE Proc. Microw.Antennas Propag., 144(4), 241-249, 1997.

Waters, C.L., Anderson, B.J. and Liou, K., 2001. Estimation of global field aligned currents using the Iridium® system magnetometer data. Geophysical Research Letters, 28(11), pp.2165-2168. doi: 10.1029/2000GL012725.

Weatherwax, A.T., P.H. Yoon, and J. LaBelle, Model results and interpretation related to topside observations of auroral roar, J. Geophys. Res., 107, 10.1029/2001JA000315, 2002.

Weimer, D.R., 1996. A flexible, IMF dependent model of high-latitude electric potentials having "space weather" applications. Geophysical Research Letters, 23(18), pp.2549-2552. doi: 10.1029/96GL02255.

Wiggins, A. and He, Y., 2016, February. Community-based data validation practices in citizen science. In Proceedings of the 19th ACM Conference on computer-supported cooperative work & social computing (pp. 1548-1559). ACM. doi: 10.1145/2818048.2820063.

Willis, P., Fagard, H., Ferrage, P., Lemoine, F.G., Noll, C.E., Noomen, R., Otten, M., Ries, J.C., Rothacher, M., Soudarin, L. and Tavernier, G., 2010. The international DORIS service (IDS): toward maturity. Advances in space research, 45(12), pp.1408-1420. doi:10.1016/j.asr.2009.11.018.

Willis, P., Soudarin, L., Jayles, C. and Rolland, L., 2007. DORIS applications for solid earth and atmospheric sciences. Comptes Rendus Geoscience, 339(16), pp.949-959. doi: 10.1016/j.crte.2007.09.015.

Wiltberger, M., Merkin, V., Lyon, J.G. and Ohtani, S., 2015. High-resolution global magnetohydrodynamic simulation of bursty bulk flows. Journal of Geophysical Research: Space Physics, 120(6), pp.4555-4566. doi: 10.1002/2015JA021080.

Winningham, J.D., Sharber, J.R., Frahm, R.A., Burch, J.L., Eaker, N., Black, R.K., Blevins, V.A., Andrews, J.P., Rudzki, J., Sablik, M.J. and Chenette, D.L., 1993. The UARS particle environment monitor. Journal of Geophysical Research: Atmospheres, 98(D6), pp.10649-10666. doi: 10.1029/93JD00461.

Wygant, J.R., Keiling, A., Cattell, C.A., Johnson, M., Lysak, R.L., Ternerin, M., Mozer, F.S., Kletzing, C.A., Scudder, J.D., Peterson, W. and Russell, C.T., 2000. sheet-tail lobe boundary to UVI images: An energy source for the aurora. Journal of Geophysical Research, 105(A8), pp.18-675.

Yamamoto, M., 2008. Digital beacon receiver for ionospheric TEC measurement developed with GNU Radio. Earth, Planets and Space, 60(11), pp.e21-e24. doi: 10.1186/BF03353137.

Yang, J., Toffoletto, F., Lu, G., and Wiltberger, M.(2014), RCM-E and AMIE studies of the Harang reversal formation during a steady magnetospheric convection event, J. Geophys. Res. Space Physics, 119, 7228– 7242, doi:10.1002/2014JA020207.

Yoon, P.H., J. LaBelle, A.T. Weatherwax, and M. Samara, Mode conversion radiation in the terrestrial ionosphere and magnetosphere, in Geospace Electromangetic Waves and Radiation, ed. by R.A. Treumann and J. LaBelle, Springer-Verlag, 2006.

Young, D.T., Bame, S.J., Thomsen, M.F., Martin, R.H., Burch, J.L., Marshall, J.A. and Reinhard, B., 1988. 2π-radian field-of-view toroidal electrostatic analyzer. Review of scientific instruments, 59(5), pp.743-751. doi: 10.1063/1.1139821.

Zanetti, L., Potemra, T., Erlandson, R., Bythrow, P., Anderson, B., Lui, A., Ohtani, S.I., Fountain, G., Henshaw, R., Ballard, B. and Lohr, D., 1994. Magnetic field experiment on the Freja satellite. In The Freja Mission (pp. 61-78). Springer, Dordrecht. doi: 10.1007/978-94-011-0299-5_4.

Zanetti, L.J., Baumjohann, W. and Potemra, T.A., 1983. Ionospheric and Birkeland current distributions inferred from the MAGSAT magnetometer data. Journal of Geophysical Research: Space Physics, 88(A6), pp.4875-4884. doi: 10.1029/JA088iA06p04875.

Zettergren M., M. Hirsch, P. Inchin, J. Klenzing, and G. Grubbs, Gemini3D ionospheric modeling suite (software). http://doi.org/10.5281/zenodo.4757432

Zettergren, M. and Semeter, J., 2012. Ionospheric plasma transport and loss in auroral downward current regions. Journal of Geophysical Research: Space Physics, 117(A6). doi: 10.1029/2012JA017637.

Zettergren, M. D., and Snively, J. B. (2015), Ionospheric response to infrasonic-acoustic waves generated by natural hazard events, J. Geophys. Res. Space Physics, 120, 8002– 8024, doi:10.1002/2015JA021116.

Zettergren, M., Lynch, K., Hampton, D., Nicolls, M., Wright, B., Conde, M., Moen, J., Lessard, M., Miceli, R. and Powell, S., 2014. Auroral ionospheric F region density cavity formation and evolution: MICA campaign results. Journal of Geophysical Research: Space Physics, 119(4), pp.3162-3178. doi: 10.1002/2013JA019583.

Zettergren, M., Semeter, J., Burnett, B., Oliver, W., Heinselman, C., Blelly, P.L. and Diaz, M., 2010. Dynamic variability in F-region ionospheric composition at auroral arc boundaries. Annales Geophysicae (09927689), 28(2).

Zettergren, M., Semeter, J., Heinselman, C. and Diaz, M., 2011. Incoherent scatter radar estimation of F region ionospheric composition during frictional heating events. Journal of Geophysical Research: Space Physics, 116(A1). doi: 10.1029/2010JA016035.

Zettergren, M.D. and Snively, J.B., 2019. Latitude and Longitude Dependence of Ionospheric TEC and Magnetic Perturbations From Infrasonic-Acoustic Waves Generated by Strong Seismic Events. Geophysical Research Letters, 46(3), pp.1132-1140. doi: 10.1029/2018GL081569.

Zhang, B., Lotko, W., Brambles, O., Wiltberger, M. and Lyon, J., 2015. Electron precipitation models in global magnetosphere simulations. Journal of Geophysical Research: Space Physics, 120(2), pp.1035-1056. doi: 10.1002/2014JA020615.

Zhu J., Taesung Park, Phillip Isola, and Alexei A. Efros. "Unpaired Image-to-Image Translation using Cycle-Consistent Adversarial Networks", in IEEE International Conference on Computer Vision (ICCV), 2017.

Zhu, J., Ridley, A.J. and Deng, Y., 2016. Simulating electron and ion temperature in a global ionosphere thermosphere model: Validation and modeling an idealized substorm. Journal of Atmospheric and Solar-Terrestrial Physics, 138, pp.243-260. doi: 10.1016/j.jastp.2016.01.005.

Zmuda,A. J. and J.C. Armstrong, The diurnal flow pattern of field-aligned currents, J. geophys. Res., 79 (1974), p. 4611

Zou, M. and Pan, J., 2015. Investigation of resonant modes in wideband hybrid omnidirectional rectangular dielectric resonator antenna. IEEE Transactions on Antennas and Propagation, 63(7), pp.3272-3275. doi: 10.1109/TAP.2015.2425421.

Zou, S., Lyons, L.R., Wang, C.P., Boudouridis, A., Ruohoniemi, J.M., Anderson, P.C., Dyson, P.L. and Devlin, J.C., 2009. On the coupling between the Harang reversal evolution and substorm dynamics: A synthesis of SuperDARN, DMSP, and IMAGE observations. Journal of Geophysical Research: Space Physics, 114(A1). doi: 10.1029/2008JA013449.

Zou, S., Moldwin, M.B., Lyons, L.R., Nishimura, Y., Hirahara, M., Sakanoi, T., Asamura, K., Nicolls, M.J., Miyashita, Y., Mende, S.B. and Heinselman, C.J., 2010. Identification of substorm onset location and preonset sequence using Reimei, THEMIS GBO, PFISR, and Geotail. Journal of Geophysical Research: Space Physics, 115(A12). doi: 10.1029/2010JA015520.

Zou, S., Moldwin, M.B., Nicolls, M.J., Ridley, A.J., Coster, A.J., Yizengaw, E., Lyons, L.R. and Donovan, E.F., 2013. Electrodynamics of the high-latitude trough: Its relationship with convection flows and field-aligned currents. Journal of Geophysical Research: Space Physics, 118(5), pp.2565-2572. doi: 10.1002/jgra.50120. doi: 10.1002/jgra.50120.

storm onset location and preonset sequence using Reimei, THEMIS GBO, PFISR, and Geotail. Journal of Geophysical Research: Space Physics, 115(A12). doi: 10.1029/2010JA015520.

Zou, S., Moldwin, M.B., Nicolls, M.J., Ridley, A.J., Coster, A.J., Yizengaw, E., Lyons, L.R. and Donovan, E.F., 2013. Electrodynamics of the high-latitude trough: Its relationship with convection flows and field-aligned currents. Journal of Geophysical Research: Space Physics, 118(5), pp.2565-2572. doi: 10.1002/jgra.50120. doi: 10.1002/jgra.50120.